The Abdus Salam International Centre for Theoretical Physics

2356-11

Targeted Training Activity: ENSO-Monsoon in the Current and Future Climate

30 July - 10 August, 2012

Monsoon Intraseasonal Oscillations: Structure, Predictability and Prediction

GOSWAMI Tanmoy

Indian Institute of Tropical Meteorology
Dr. Homi Bhabha Road, Pashan
Pune 411008
Maharashtra
INDIA

Structure, Predictability and Extended Range Prediction of Indian Summer Monsoon ISOs

B. N. Goswami

Indian Institute of Tropical Meteorology (IITM)

Outline

- Space-time characteristics of Monsoon ISOs
- Monsoon ISOs : Building Block of Monsoon Systems
- Scale selection and mechanism for northward propagation
- Predictability of Monsoon ISOs
- Extended range prediction Monsoon ISOs : Recent Developments

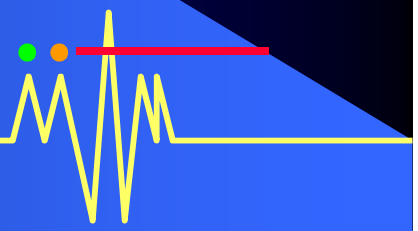

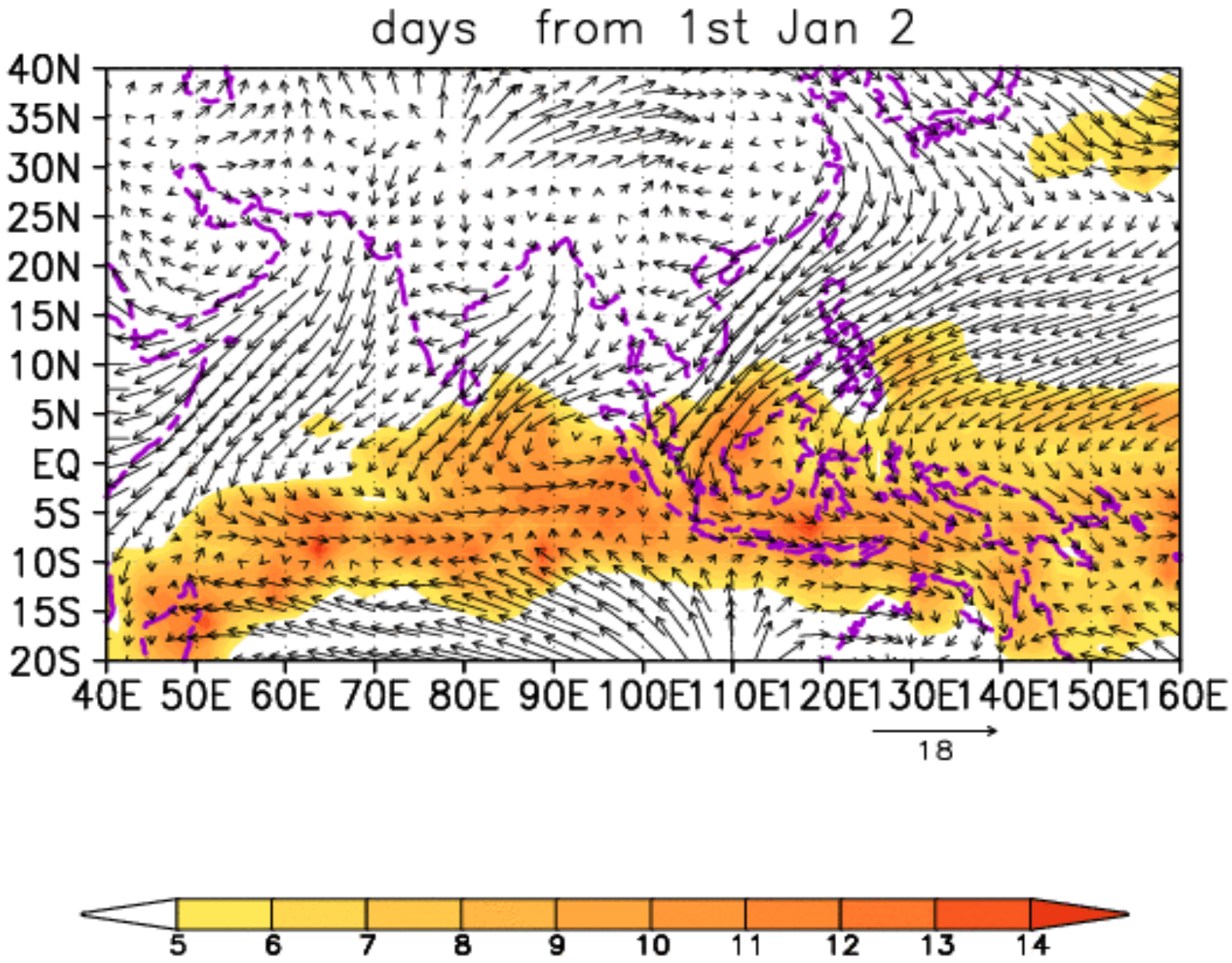

Climatological daily precipitation (color) and winds at 850 hPa, every 10 days

Long term mean

JJA precipitation and

DJF precipitation

Monsoon ?

Wet- summer

Dry - winter

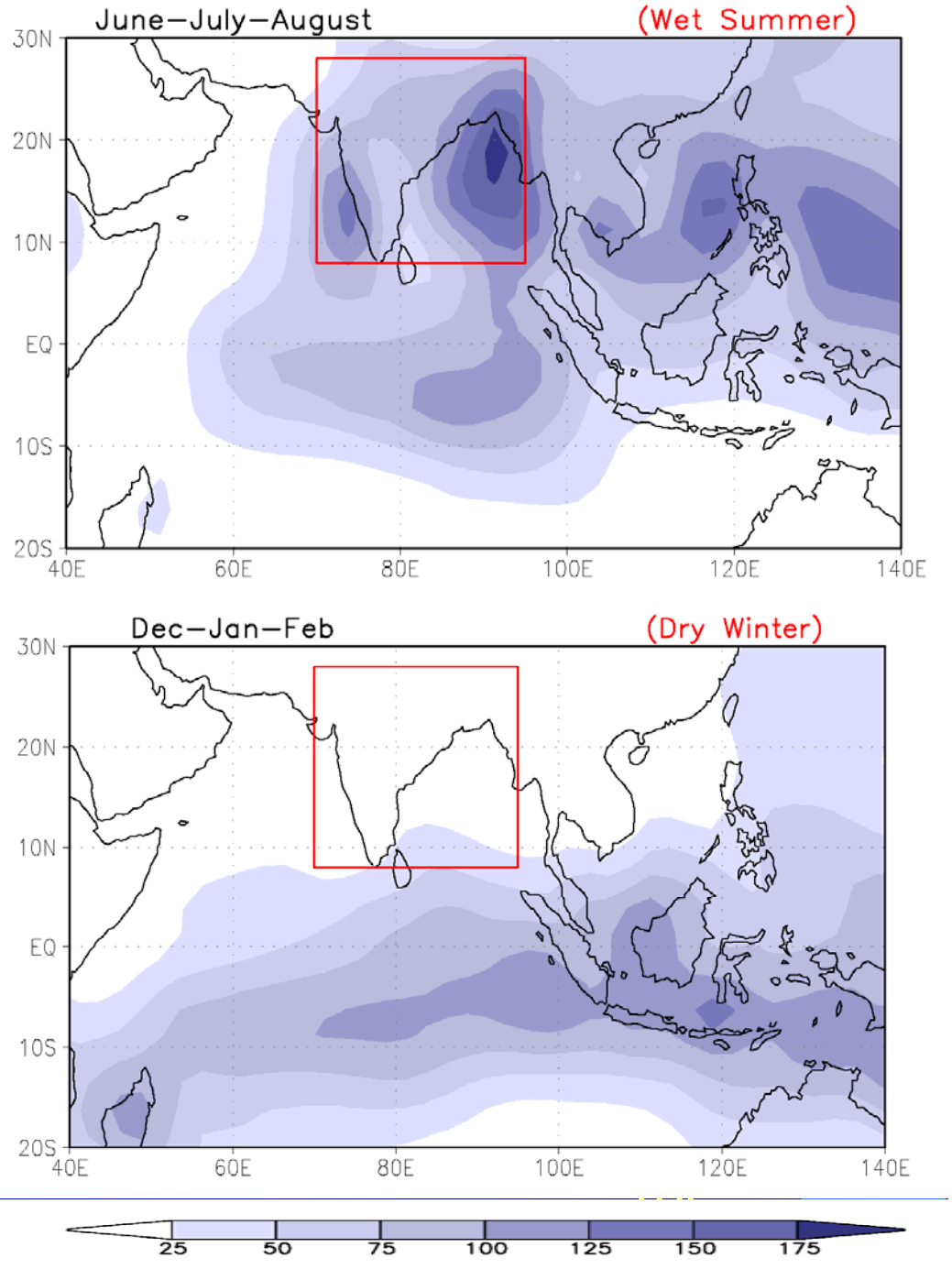

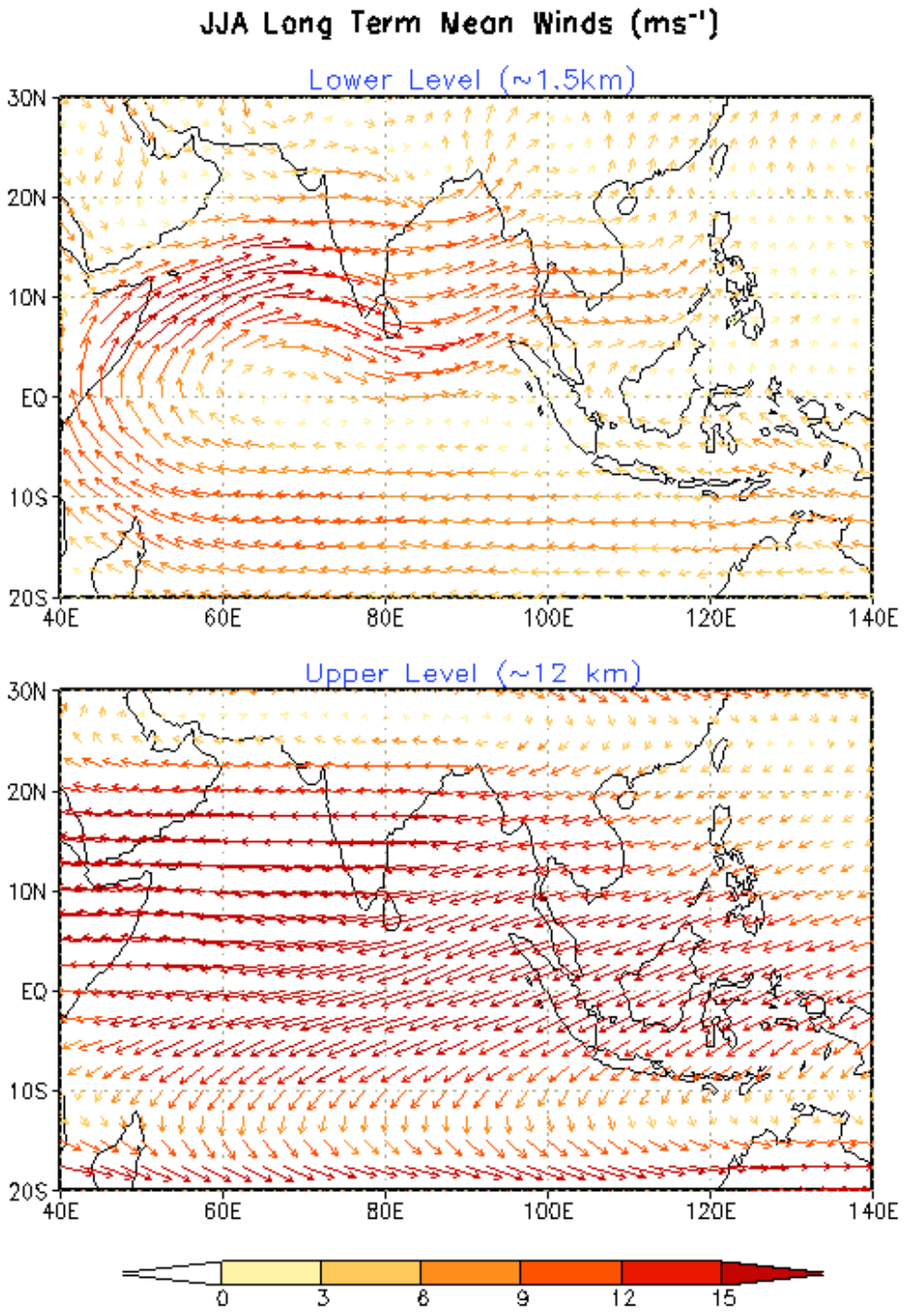

Characteristic features of the summer monsoon

Low level, cross-equatorial flow, south-westerlies, westerly jet in Arabian sea

Deep Baroclinic vertical structure

Upper level easterlies, Monsoon Easterly Jet

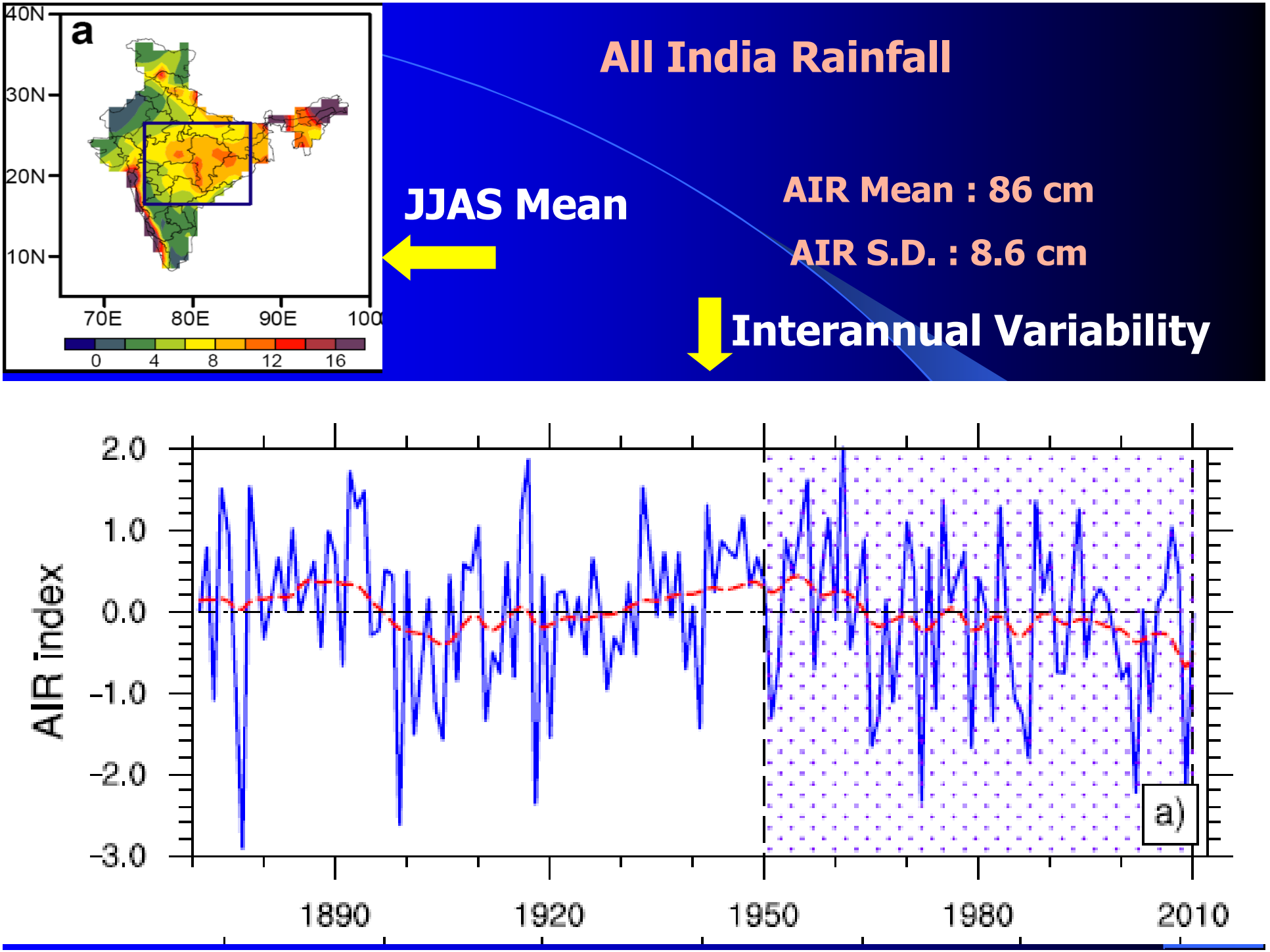
a
40N
30N
20N
10N
70E
80E
90E
100
0
4
8
12
16
All India Rainfall
JJAS Mean
AIR Mean : 86 cm
AIR S.D. : 8.6 cm
Interannual Variability
AIR index
2.0
1.0
0.0
-1.0
-2.0
-3.0
1890
1920
1950
1980
2010
a)

Active-break spells (cycles)

Daily rainfall (mm/day) over central India for three years, 1972, 1986 and 1988

The smooth curve shows long term mean.

Red shows above normal or wet spells while blue shows below normal or dry spells

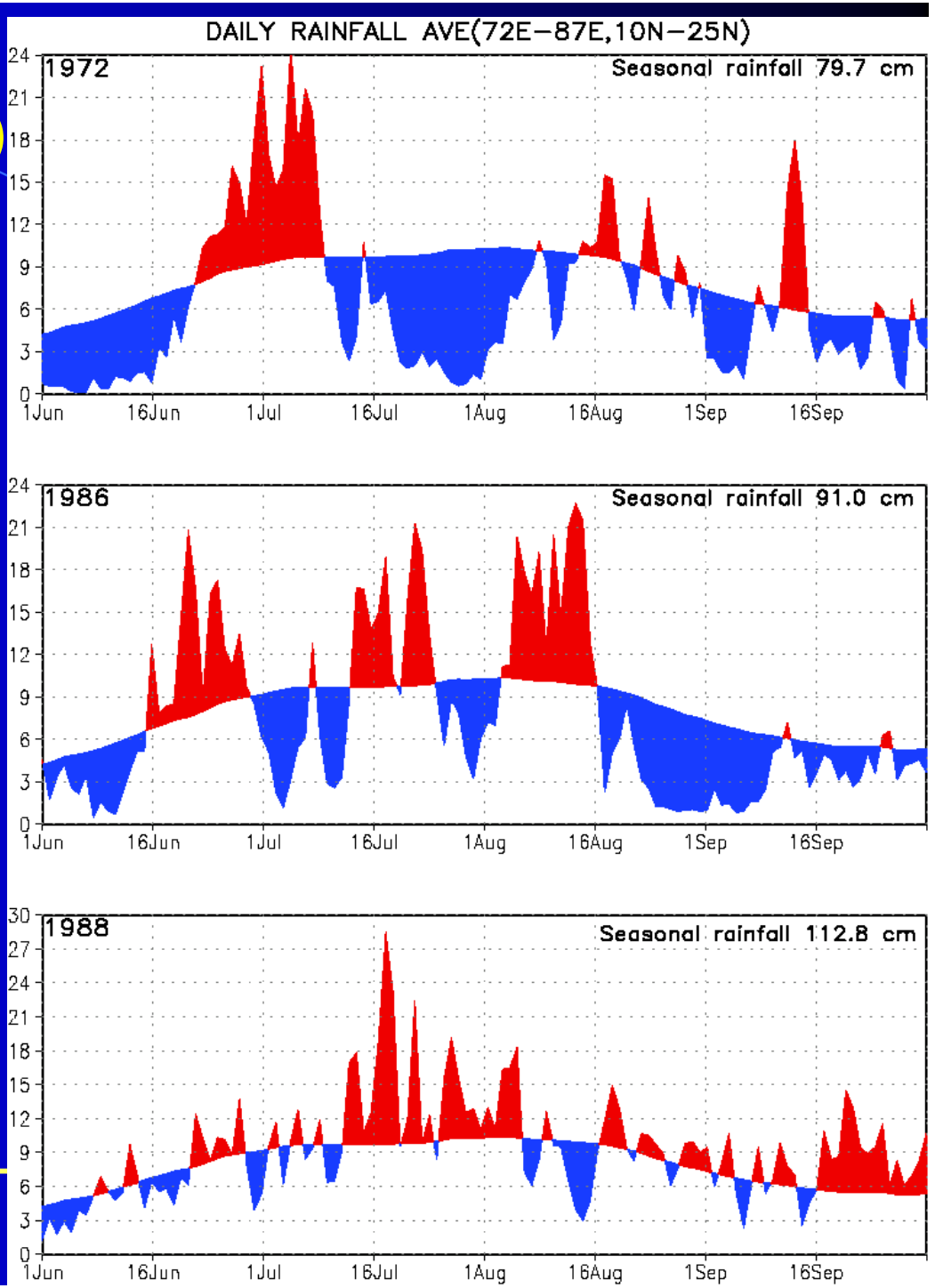

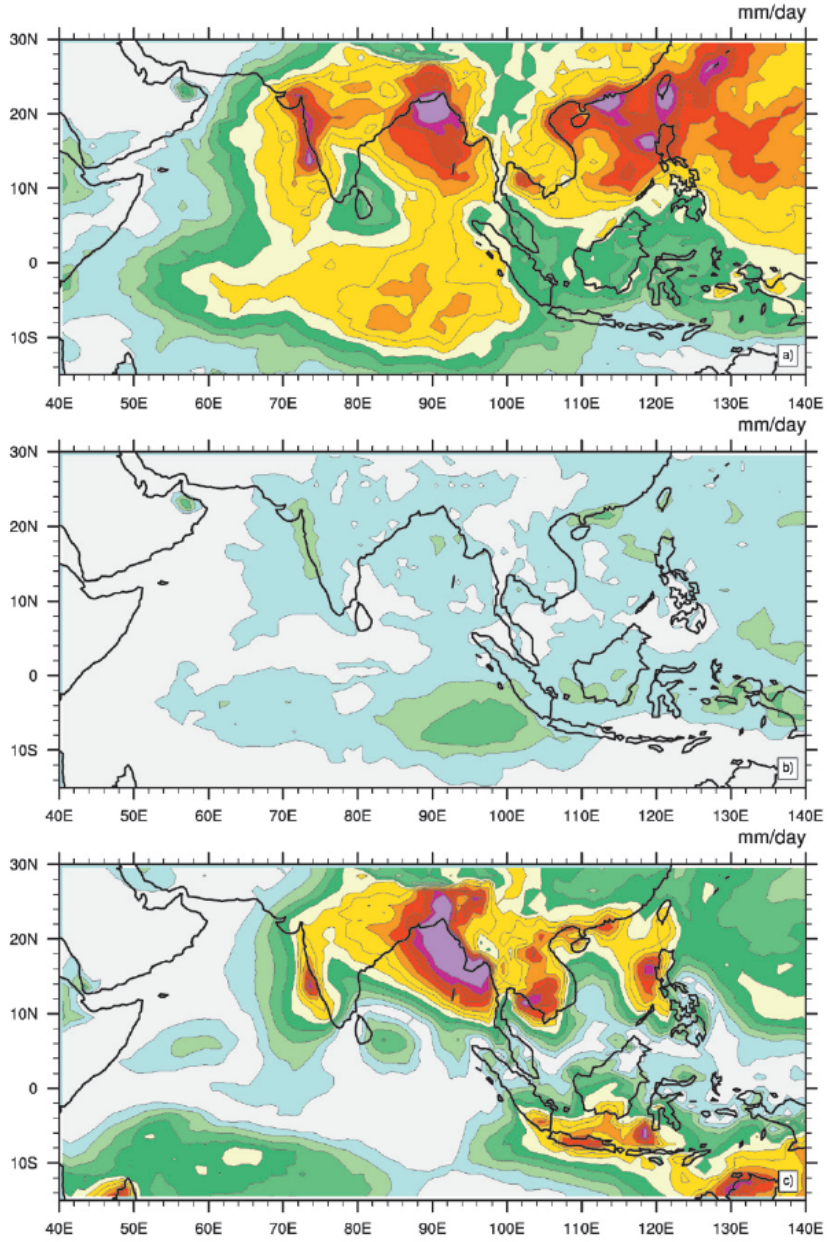

Figure 2.3. (a) Standard deviation of 10 to 90-day filtered GPCP precipitation anomalies (mm/day) based on 1997–2007 JJAS seasons. (b) Standard deviation of IAV of JJAS seasonal mean for the period 1997–2007. (c) Amplitude of the annual cycle. Climatological mean absolute value of the difference between JJAS mean and DJF mean for the 1997–2007 period from GPCP.

Why MISO are important?

They represent a very large signal and hence potentially predictable!

Relationship between Monsoon ISOs and monsoon onset

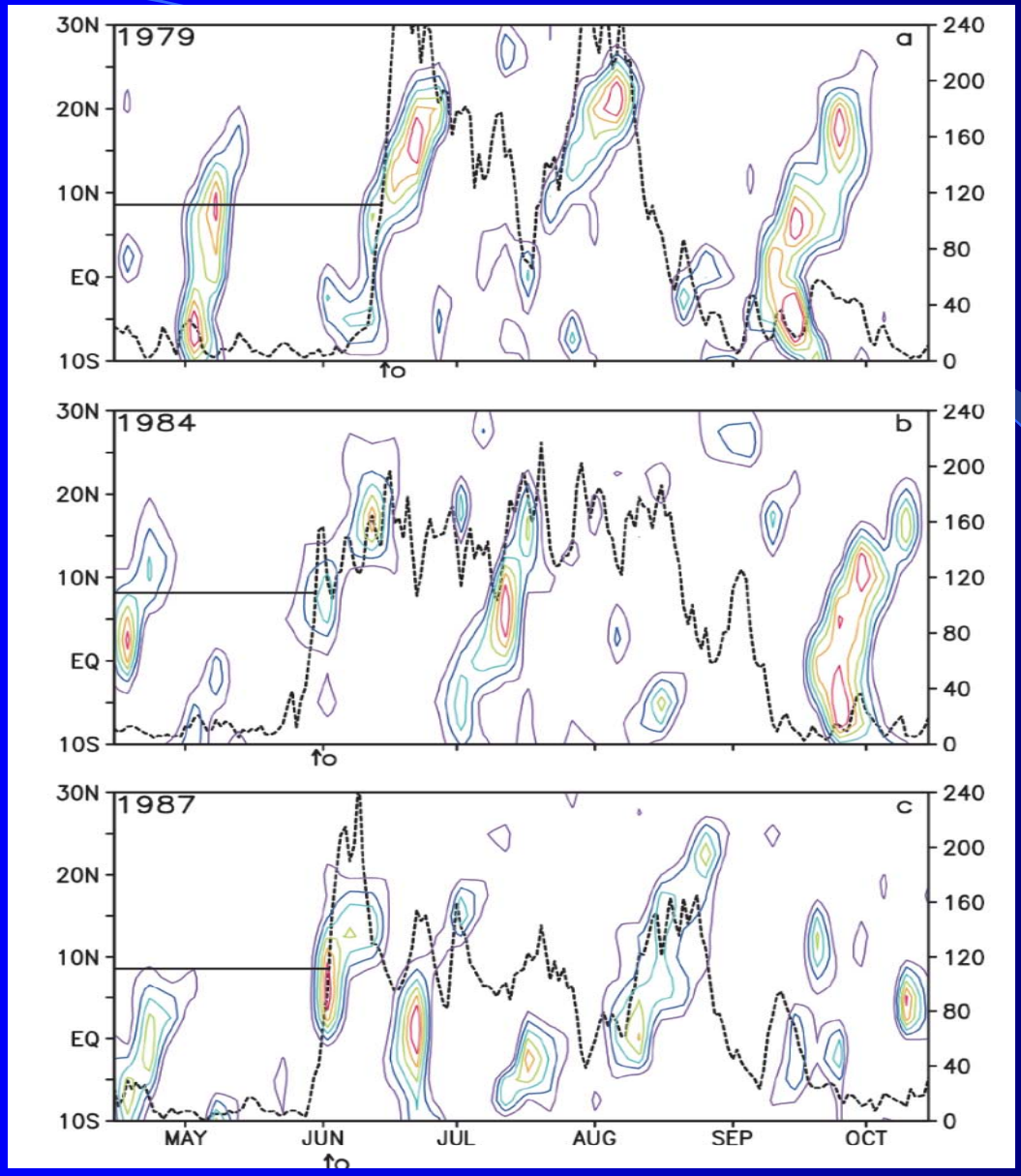

Onset

ISOs Modulate Monsoon Synoptic Activity

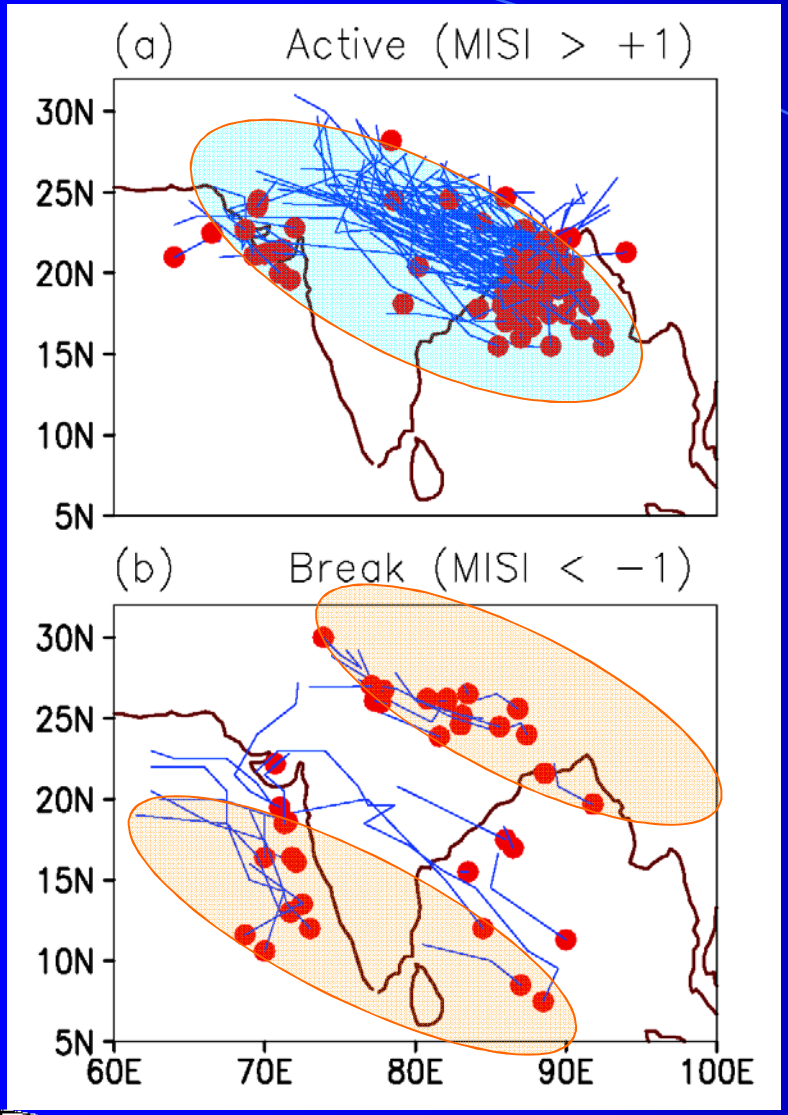

Tracks of LPS for the period 1954-1983 during extreme phases of monsoon ISO. (a) 'Active' ISO phase (MISI > +1) and (b) 'Break' ISO phase (MISI < -1). Red dots represent the genesis point and their lines show the tracks.

Goswami et al. 2003, *GRL*, 30, doi:10.1029/2002GL016734

Monsoon Intraseasonal Oscillations

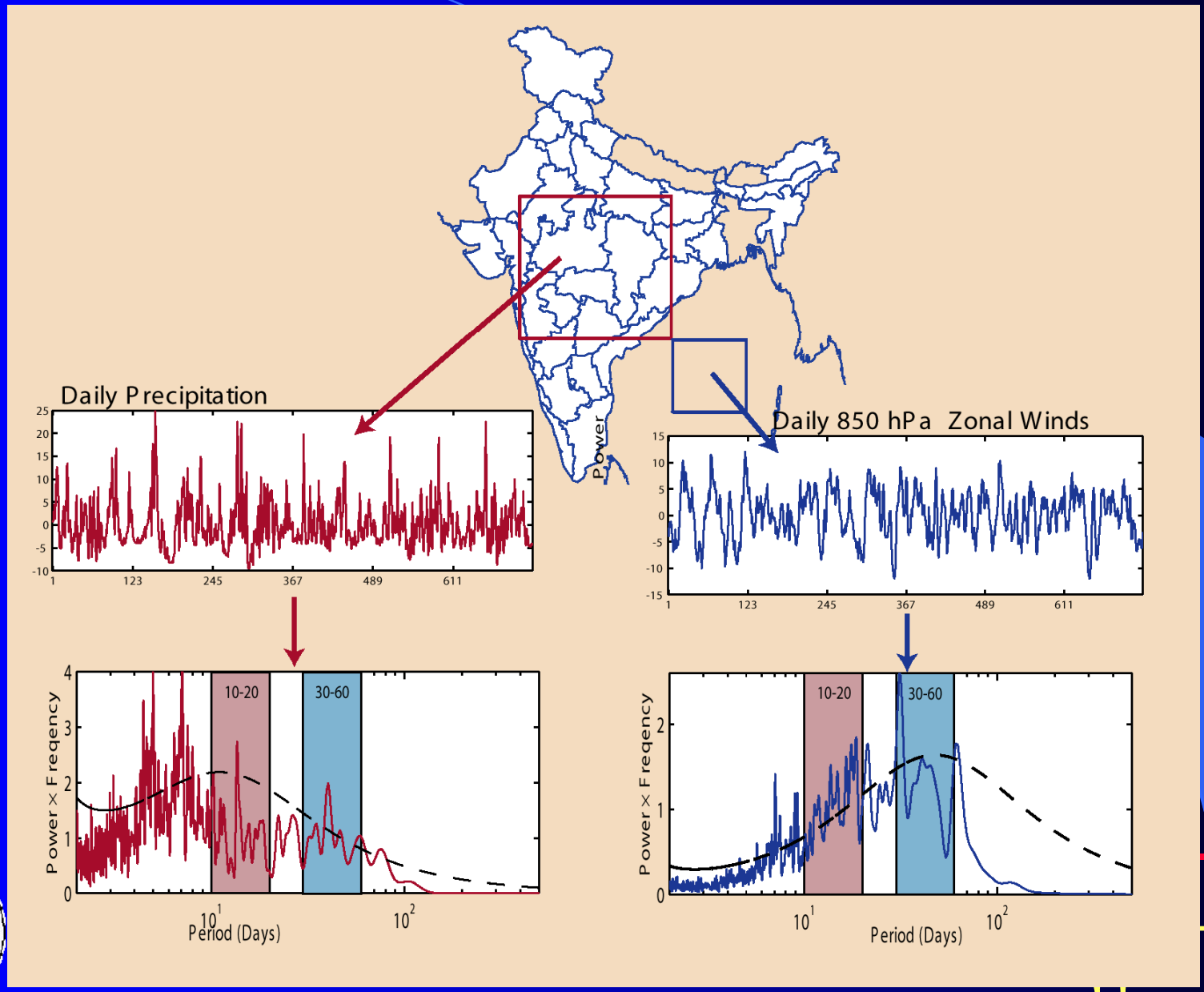

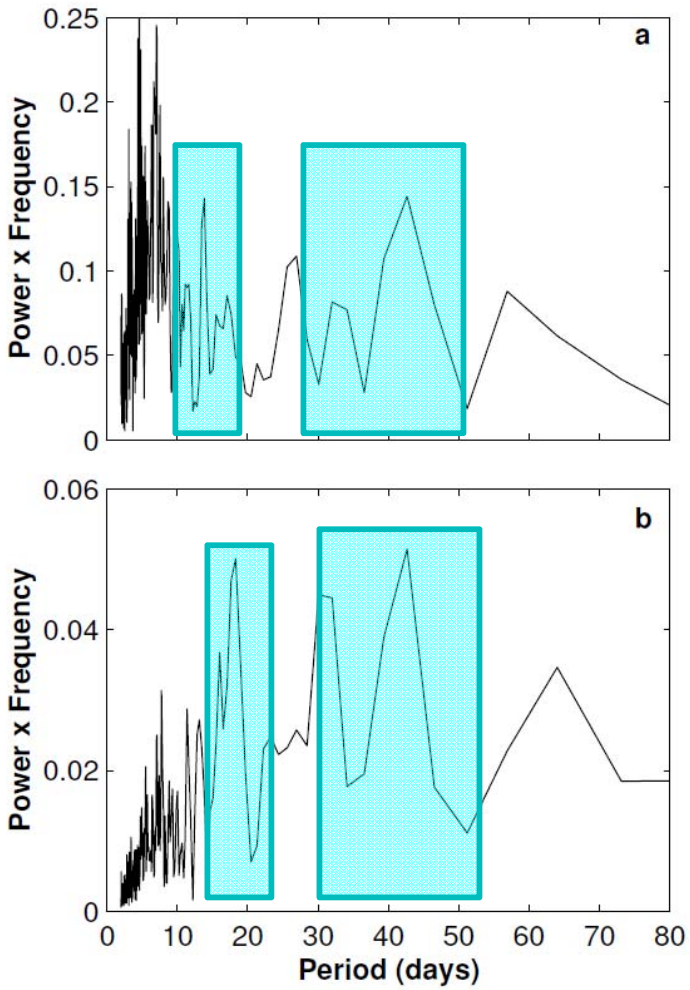

Figure 1: Spectrum of (a) rainfall anomalies for 20 (1971-1989) summer seasons (1 June -30 September) from station data averaged over 75E-85E and 15N-25N and (b) zonal wind anomalies at 850 hPa for 20 (1979-1998) summer seasons from NCEP reanalysis averaged over 55E-65E and 5N-15N.

Existence of sub-seasonal oscillations in the time-scale of 10-20 days and 30-60 days has been known to Indian meteorologists for a long time. However, their spatial scale and propagation characteristics became clear only after 1979.

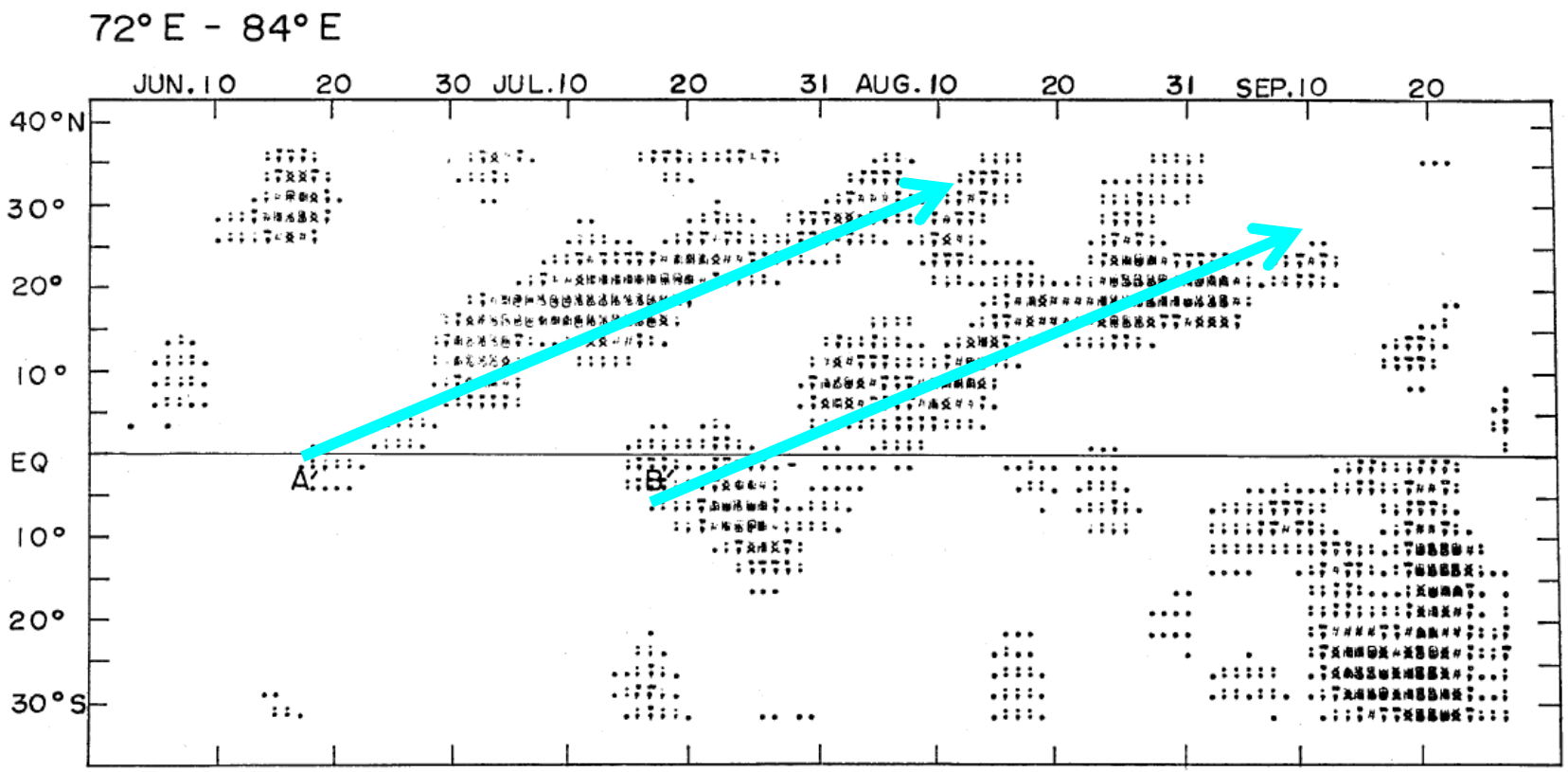

Fig. 7 Time-latitude sections of cloudiness for 72°–84°E longitude zone. Time means are subtracted from the smoothed cloudiness, and positive deviations are illustrated by the grey scale. The cloudiness difference between adjacent levels is 0.3. See text for the symbols A′ and B′.

Yasunari, 1979, JMSJ

For the first time the cloud bands were shown to propagate regularly northward with a period of over a month

Northward Propagation of Maximum Cloud Zones
Sikka and Gadgil, MWR (1980)

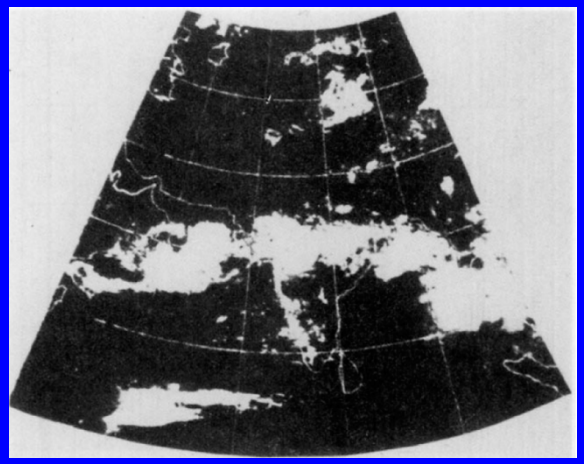

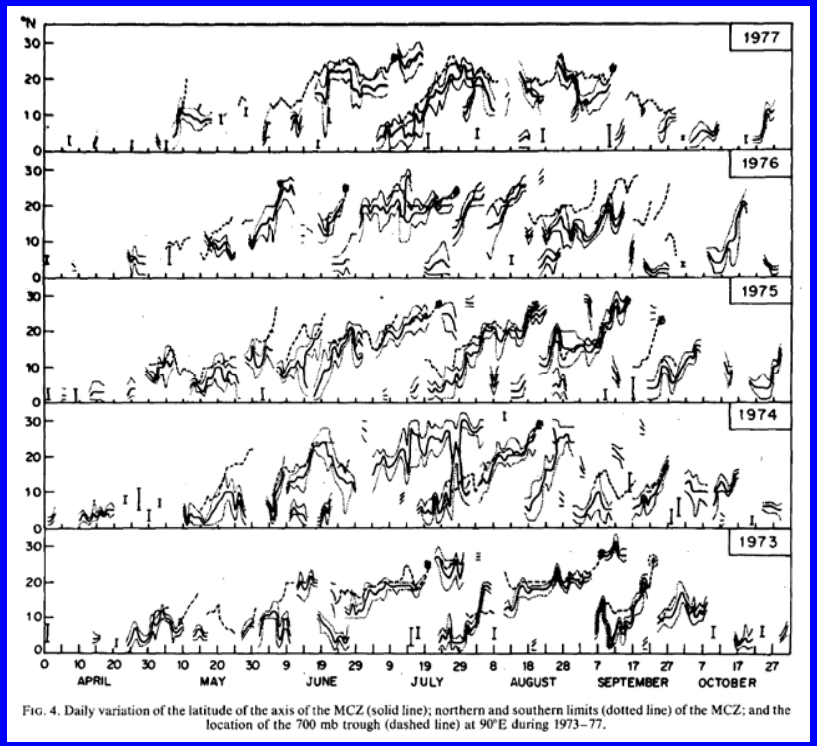

FIG. 4. Daily variation of the latitude of the axis of the MCZ (solid line); northern and southern limits (dotted line) of the MCZ; and the location of the 700 mb trough (dashed line) at 90°E during 1973–77.

- Two favorable locations for maximum cloud zones (tropical Convergence Zones, TCZs) are identified; one over the equatorial Indian Ocean and other over Monsoon zone north of 15°N.
- Revival of the monsoon occurs with a transition to a moist convective regime, either with northward propagation of the equatorial TCZ
- Established large scale nature and propagation characteristics of Monsoon ISOs

Almost simultaneously, Sikka and Gadgil showed similar northward propagation of the cloud bands.

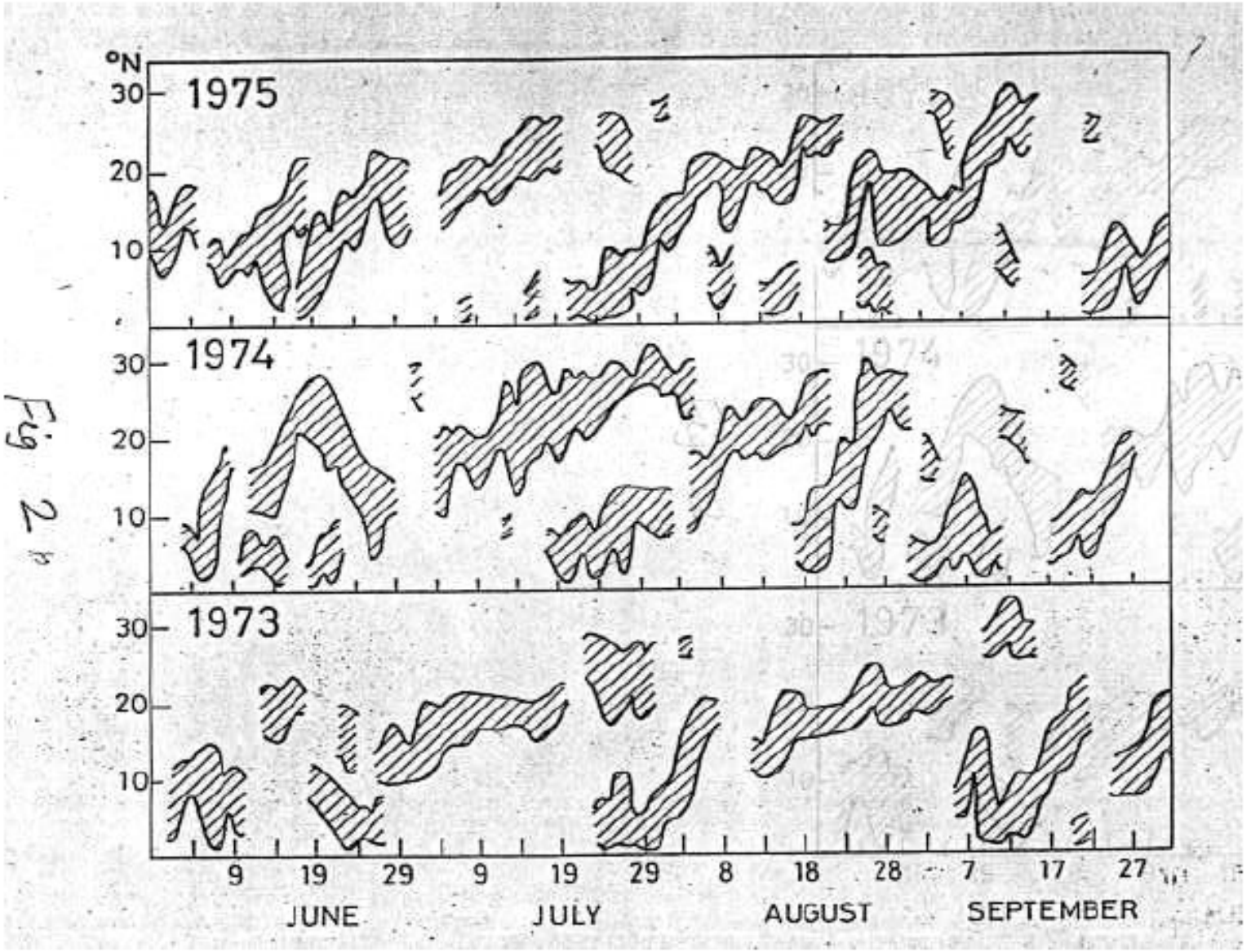

Courtesy : Prof. Gadgil

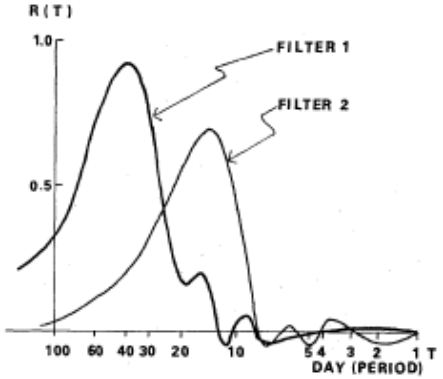

Fig. 4 Frequency response of the two filters. The peak of filter 1 exists at 40-day period and that of filter 2 is at about 14-day period.

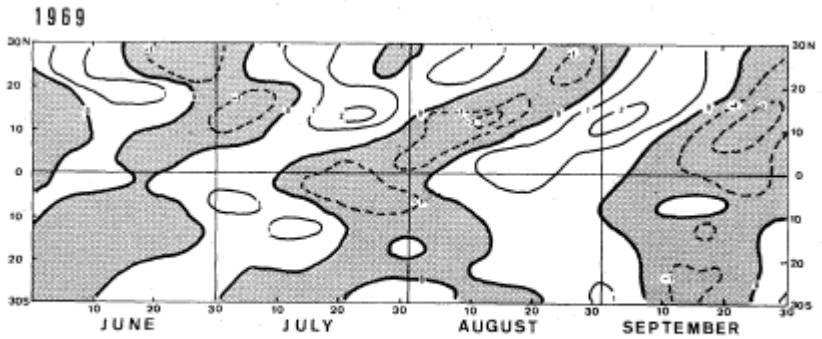

Fig. 3 Time latitude section of filtered cloudiness for the 40-day period along the longitudinal sector of 70°-90°E. Unit of contour line is 1.0 and negative values are shaded.

Yasunari, 1981, JMSJ

T. Yasunari

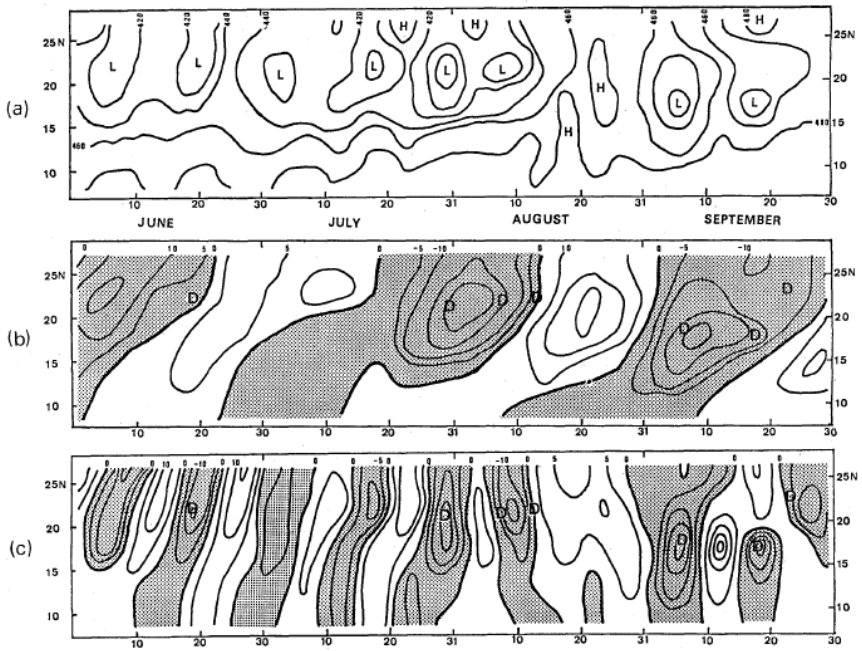

5 Cross sections of the geopotential height at 850 mb along the line shown in Fig. 1, by using (a) 5-day moving averaged data (b) data by filter 1, and (c) data by filter 2. Contour intervals are (a) 20 m, (b), (c) 5 m. The areas of negative values are shaded in (b) and (c).

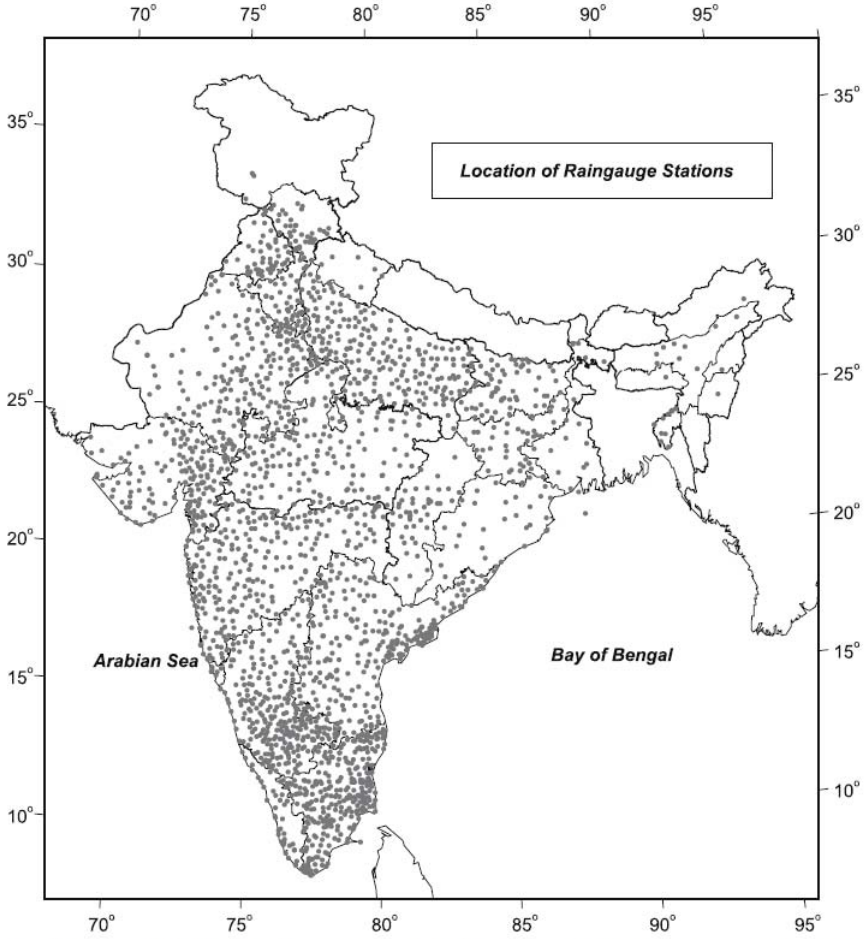

Figure 3. Network of raingauge stations considered for the development of high resolution gridded dataset.

Rajeevan,Gadgil and Bhate, 2010, JESS,

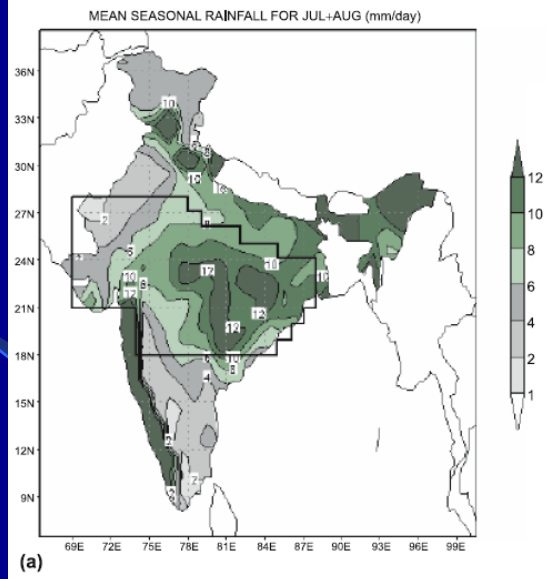

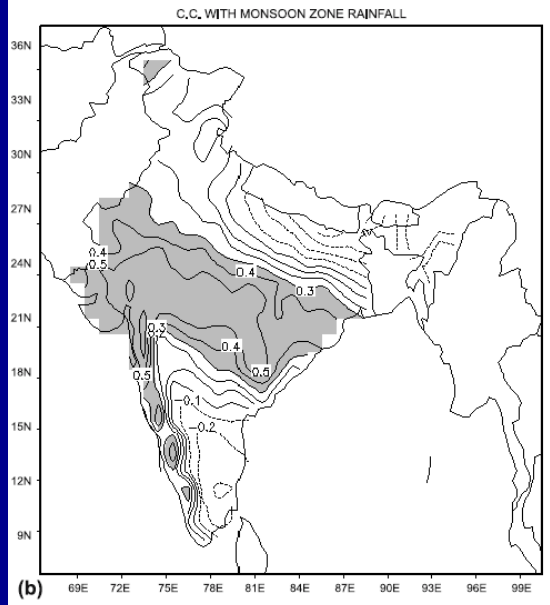

Figure 4. (a) Monsoon core zone considered to identify the active and break events. Mean (1951–2007) rainfall (mm/day) during the period July and August is also shown. (b) Correlation coefficient of 5-day average rainfall over the monsoon zone with rainfall at all grid points. Rainfall during only July and August months have been considered.

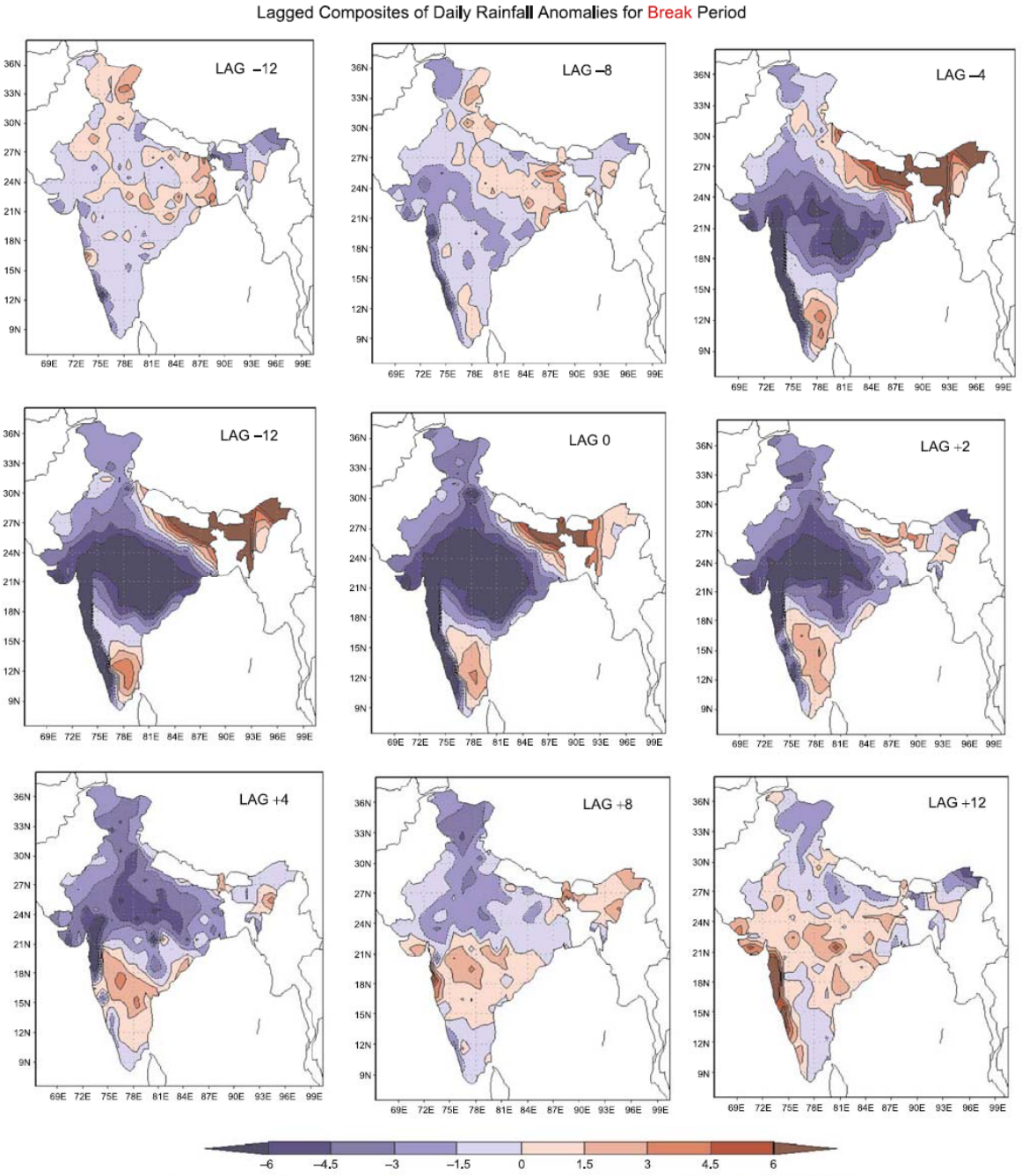

Figure 7(a). Lagged rainfall (mm) composites during the break spells (1951–2004).

Break Composite

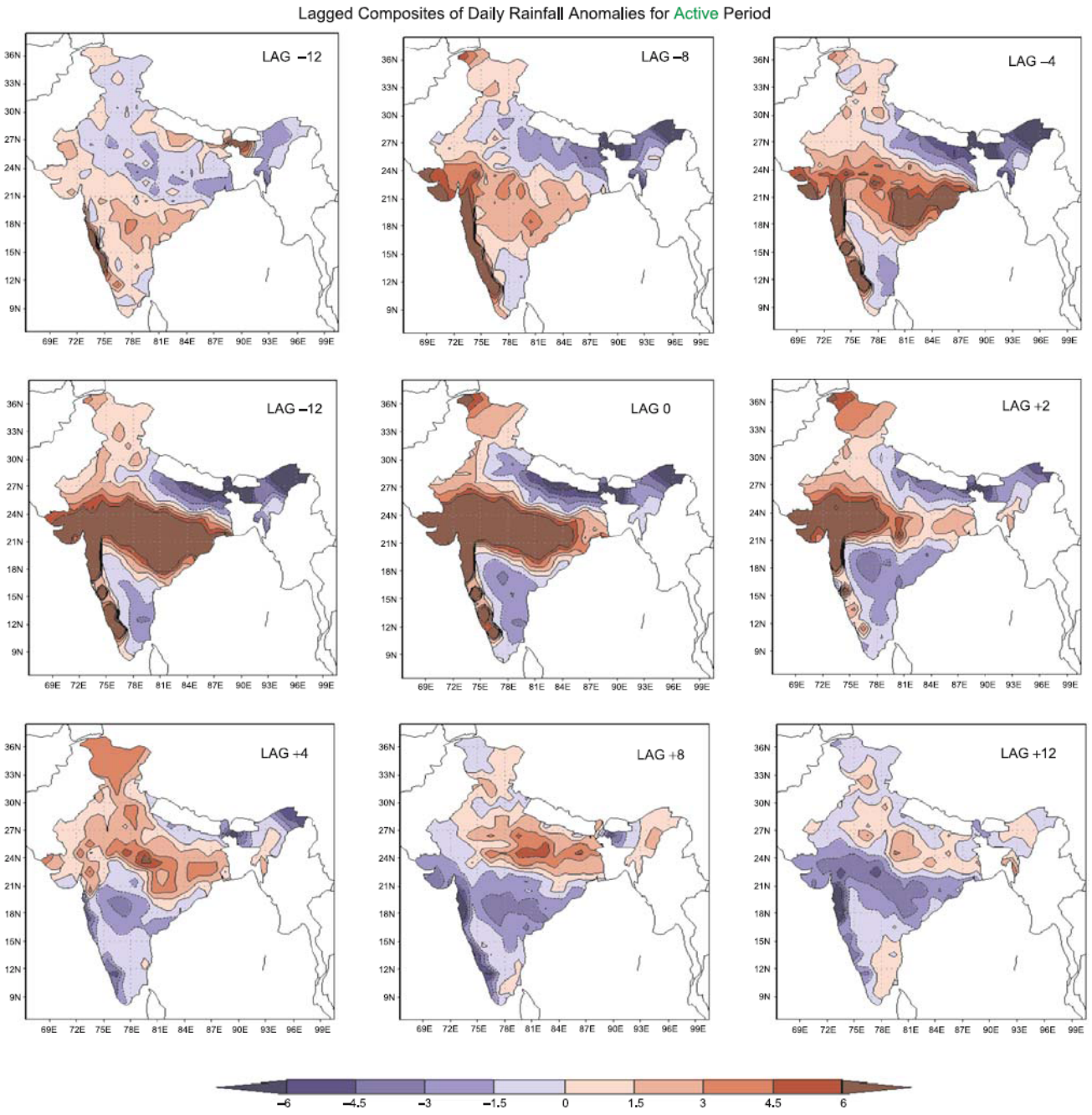

Figure 7(b). Lagged rainfall (mm) composites for the active spells (1951–2004).

Active Composite

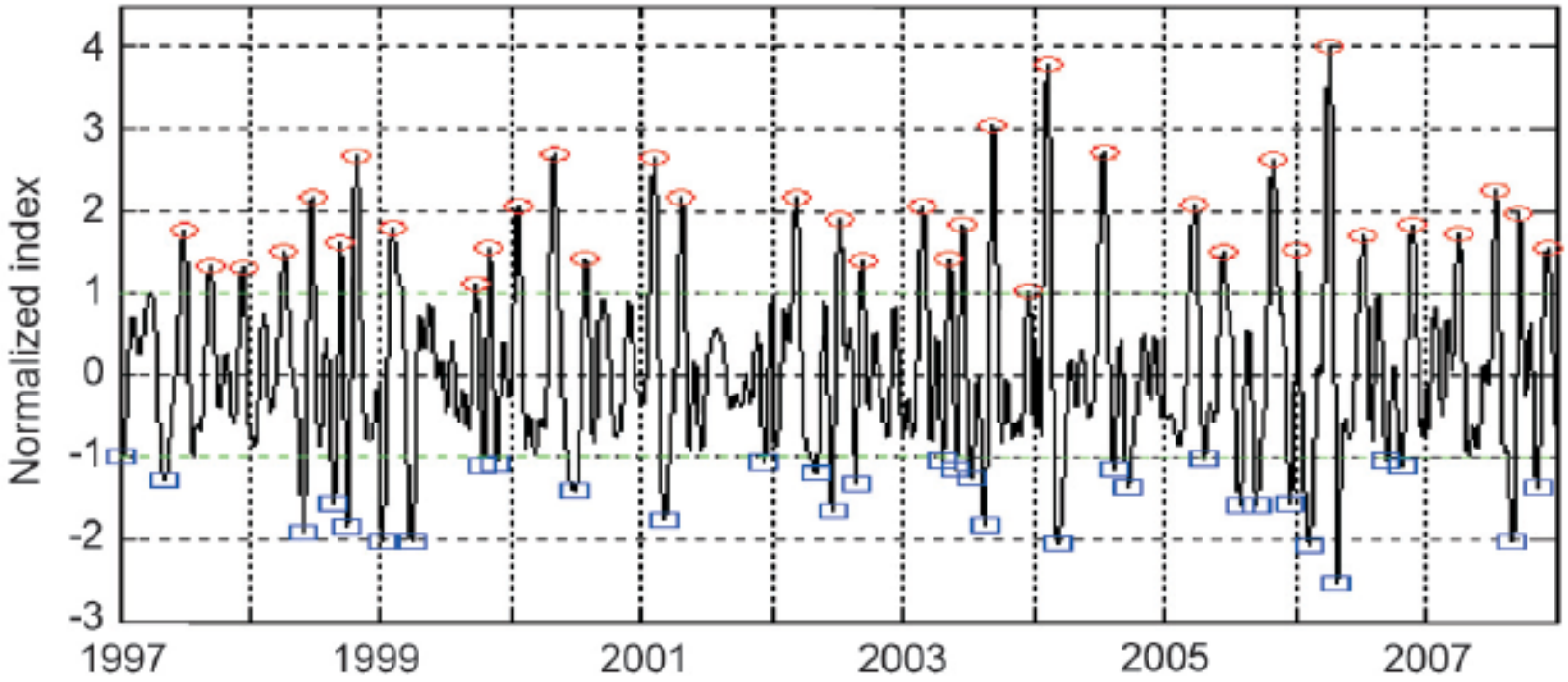

Figure 2.4. Time series of normalized monsoon ISO index between June 1 and September 30 (122 days) for a sample of 11 (1997–2007) summer seasons. The ISO index is defined as 10 to 90-day filtered GPCP rainfall anomaly averaged between 70°E–90°E and 15°N–25°N. The time series is normalized by its own standard deviation. Open circles and squares indicate peaks of active and break conditions, respectively.

Lag composite of MISO: 25-90 day (GPCP JJAS)

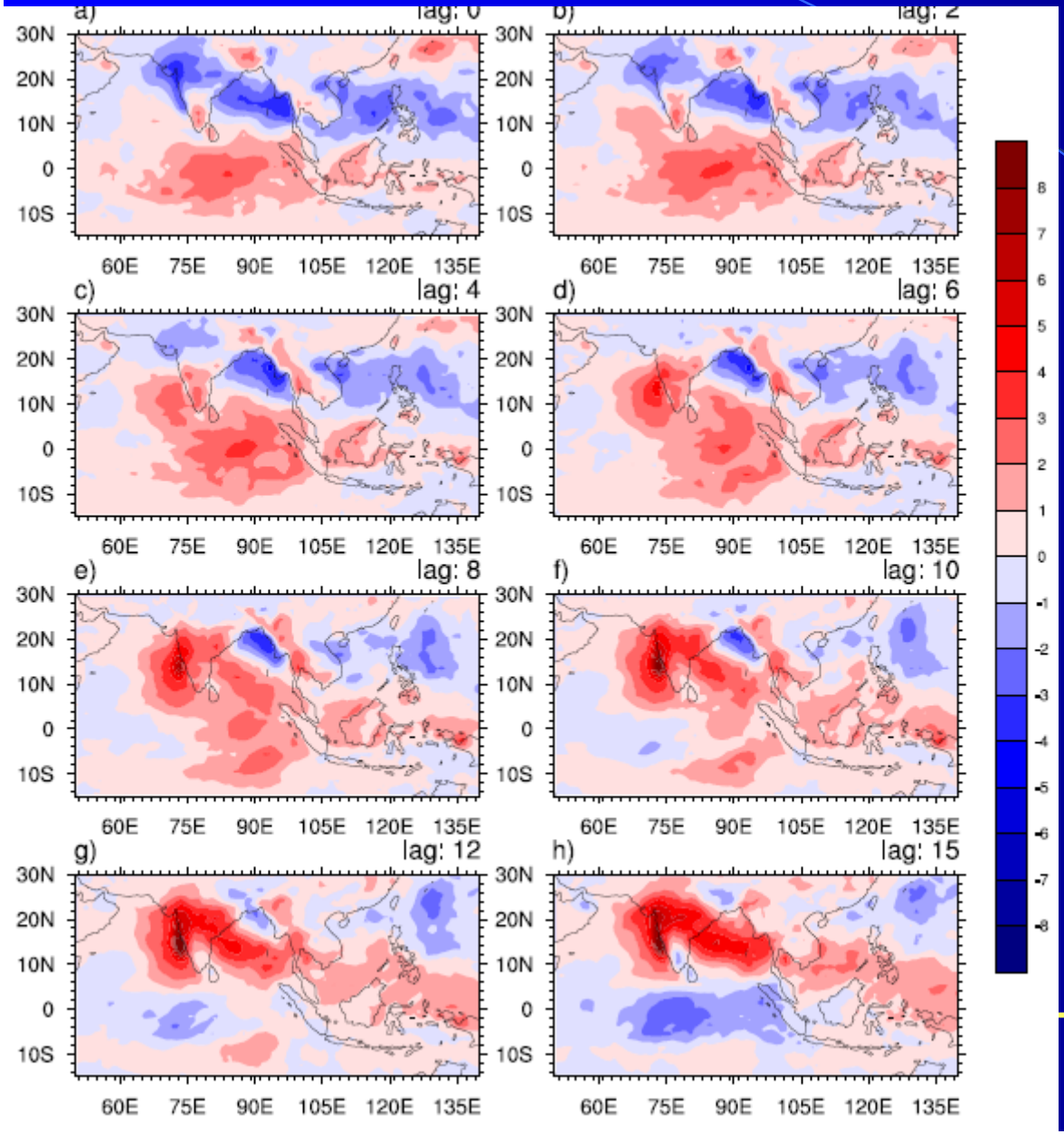

MISO evolution
one half cycle

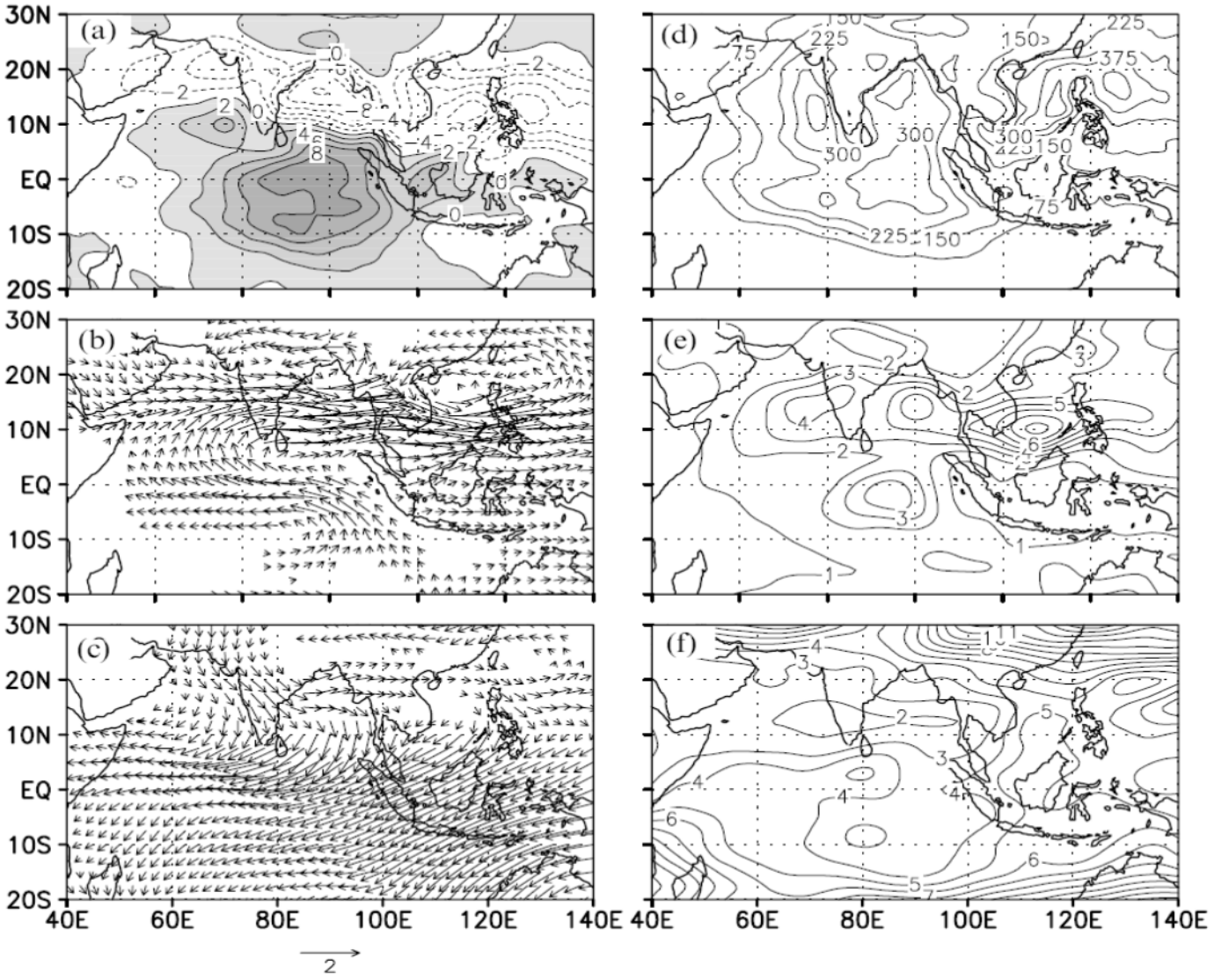

Figure 2.10. Spatial structure and amplitude of the 30–60-day mode. Regressed 30–60-day filtered anomalies of (a) OLR (in $W\,m^{-2}$), (b) 850-hPa winds, and (c) 200-hPa winds (in $m\,s^{-1}$) with respect to a reference time series of 30–60-day filtered zonal winds averaged over 85°E–90°E and 5°N–10°N with 0 lag. Only regressed wind anomalies significant at 95% confidence level are plotted, with a mean variance of 30–60-day filtered (d) OLR (in $W^2\,m^{-4}$), (e) 850-hPa, and (f) 200-hPa zonal winds (in $m^2\,s^{-2}$), based on 20 (1979–1998) summers (1 June–30 September).

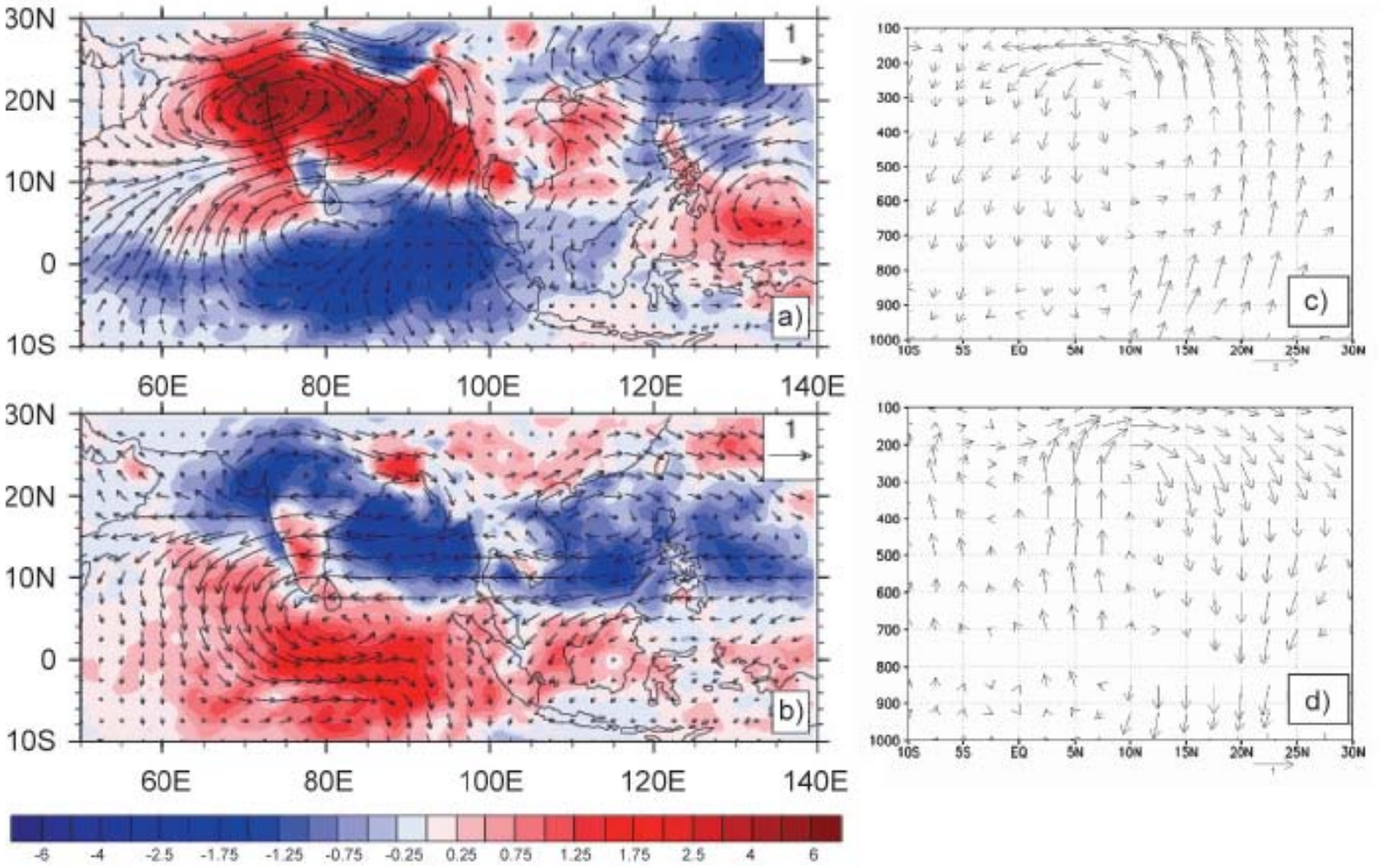

Figure 2.5. Horizontal and vertical structure of dominant ISV. Regressed 10 to 90-day filtered GPCP (shaded, mm day^{-1}) and zonal and meridional wind anomalies at 850 hPa (vectors, m s^{-1}) with respect to the ISO index (Figure 2.4) at (a) 0 lag (active condition) and (b) 14-day lag (break condition). (c) and (d) The anomalous regional Hadley circulation associated with active and break conditions, respectively. Regressed meridional and vertical wind anomalies at a number of vertical levels averaged over 75°E–85°E. Vertical wind anomalies (h Pa s^{-1}) have been scaled up by a factor of 100.

Goswami, 2011, ISV Book,Chapt-2

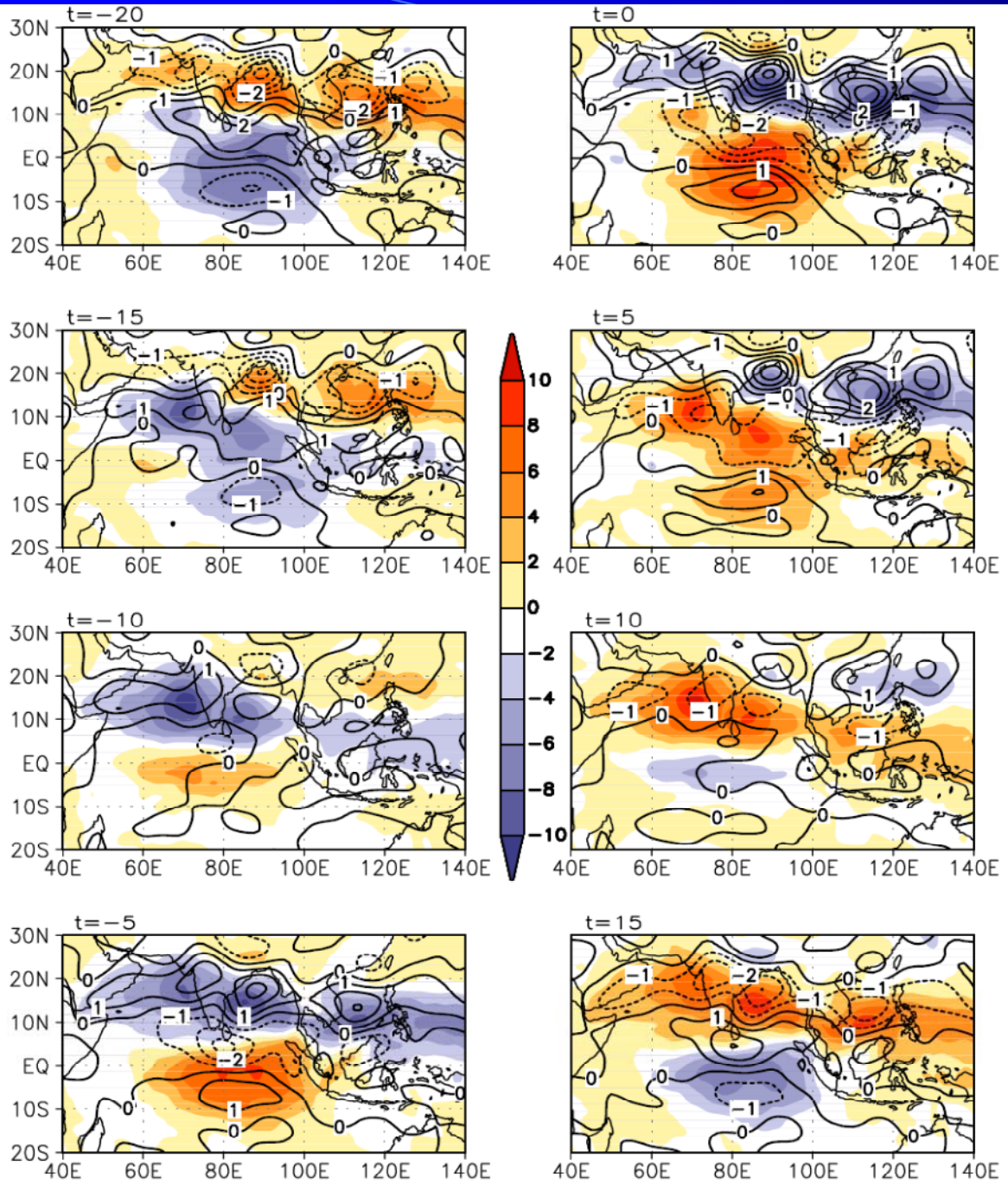

Large scale structure: relationship between OLR and 850 hPa vorticity

Regressed OLR (shaded) and 850 hPa relative vorticity (contour) w.r.t a reference time series of 10-90 day filtered OLR over CI

Goswami, 2005: ISV book

Convectively Coupled...

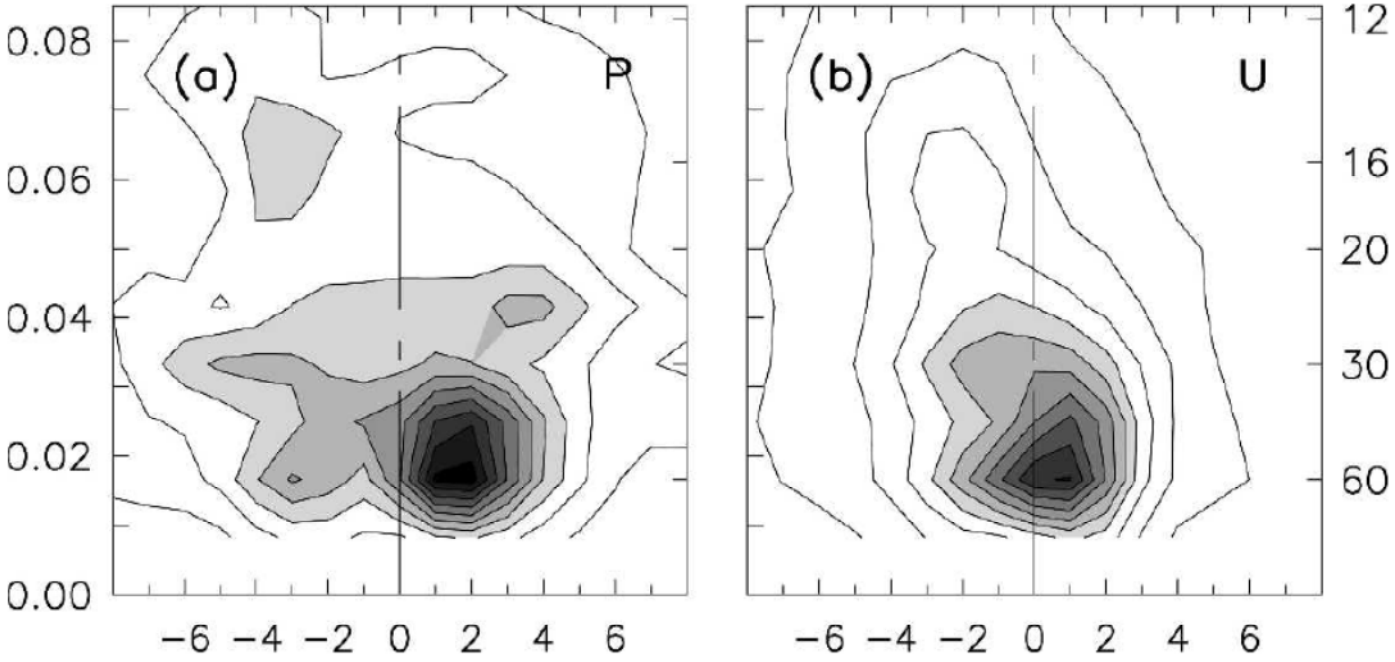

FIG. 2. Wavenumber–frequency spectral power of observed precipitation and 850-hPa zonal winds anomalies averaged over the latitude band 5°–25°N. The *y* axis left ordinate is frequency (in cycles per day, cpd) and right ordinate is period (days), while the *x* axis represents zonal wavenumber. The minimum contour and contour interval is 0.5; contours greater than 2.0 are shaded.

What is responsible for the northward propagation?

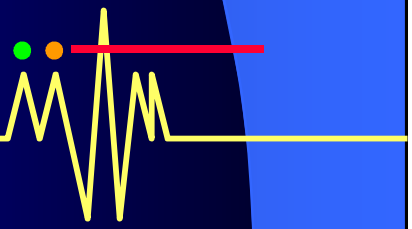

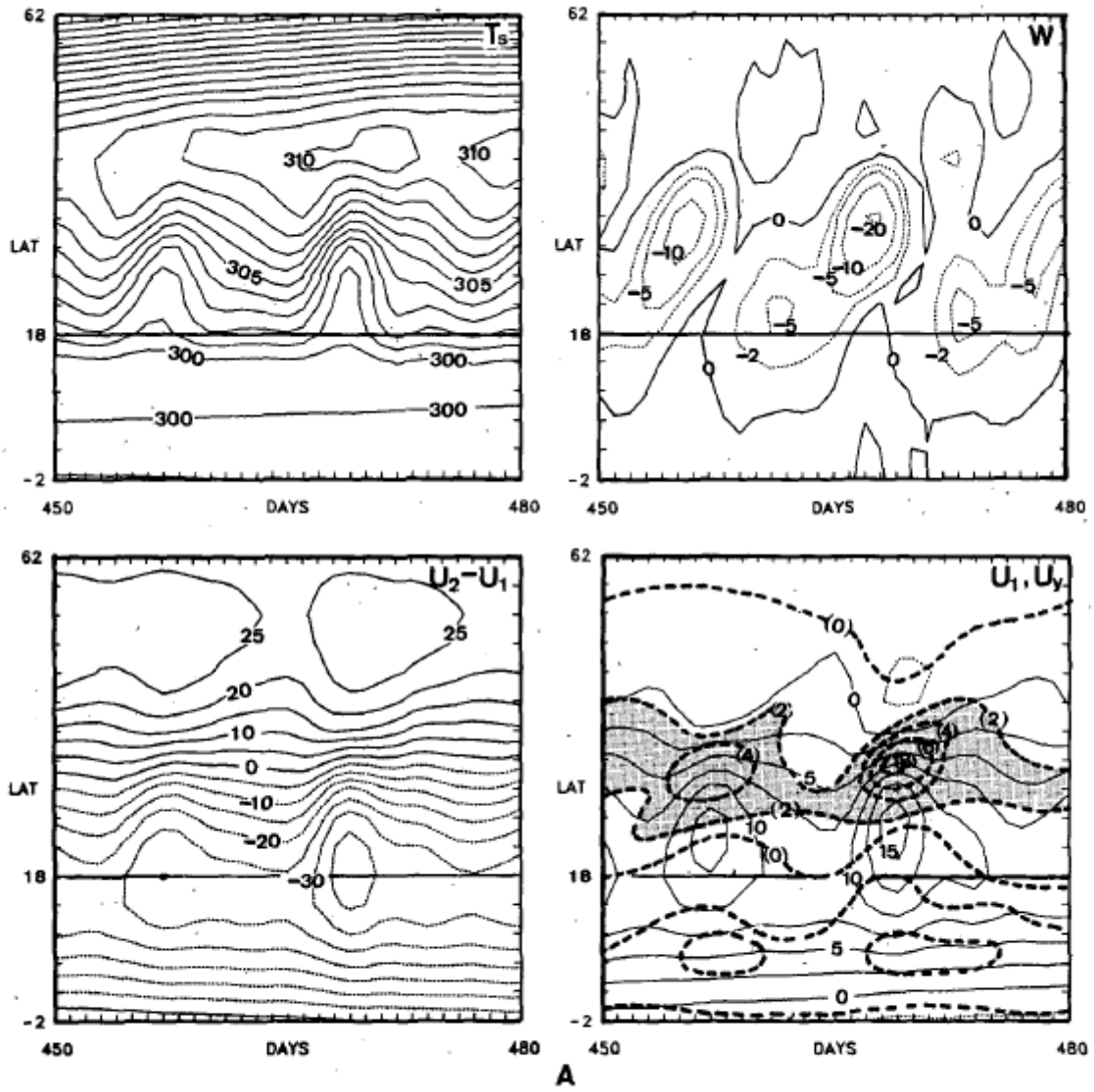

FIG. 3a. Detailed structure of various fields of the region A demarked in Figs. 2. Surface temperature and vertical velocity contours are shown in the upper two panels (units, °K and 10^{-4} mb s^{-1}, respectively). Lower left panel provides a measure of the vertical shear ($u_2 - u_1$, m s^{-1}). Solid contours of the lower right panel show the 750 mb zonal velocity component (m s^{-1}). The latitudinal shear (heavy dashed lines) are superimposed. Shaded area denotes latitudinal shear exceeding -2 m s^{-1} (500 km)$^{-1}$.

Mechanism of northward propagation

Webster , 1983, JAS

Used a very simple two-layer model

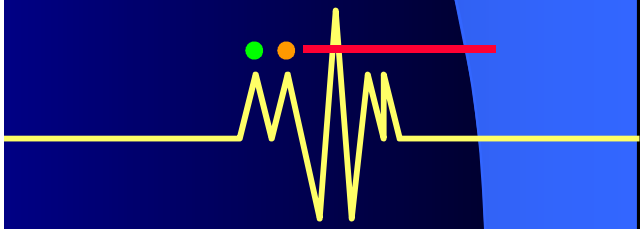

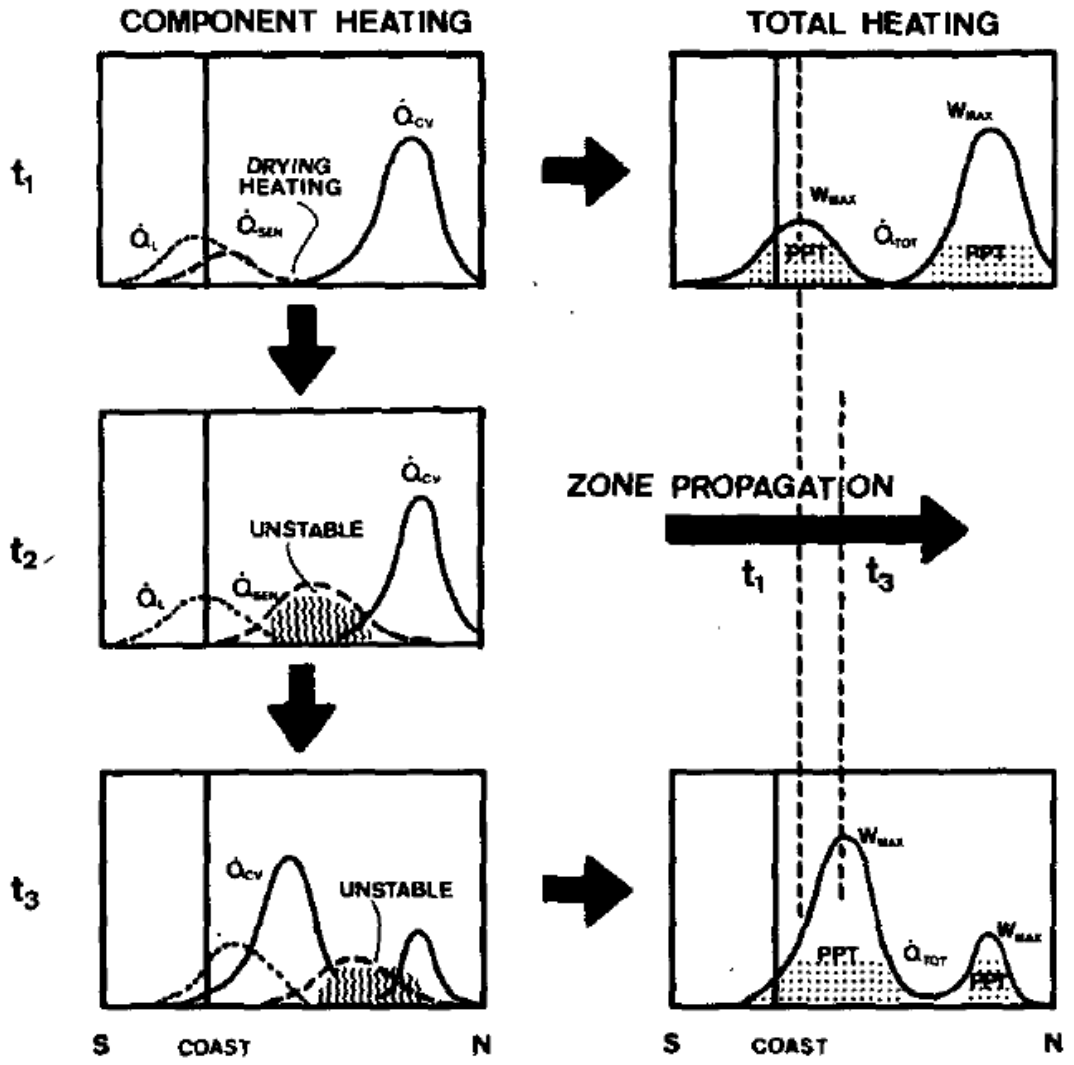

FIG. 7. Schematic representation of the interaction of the components of the total heating function and the dynamic feedback. Diagrams show two successive times and the resultant zone propagation away from the coast.

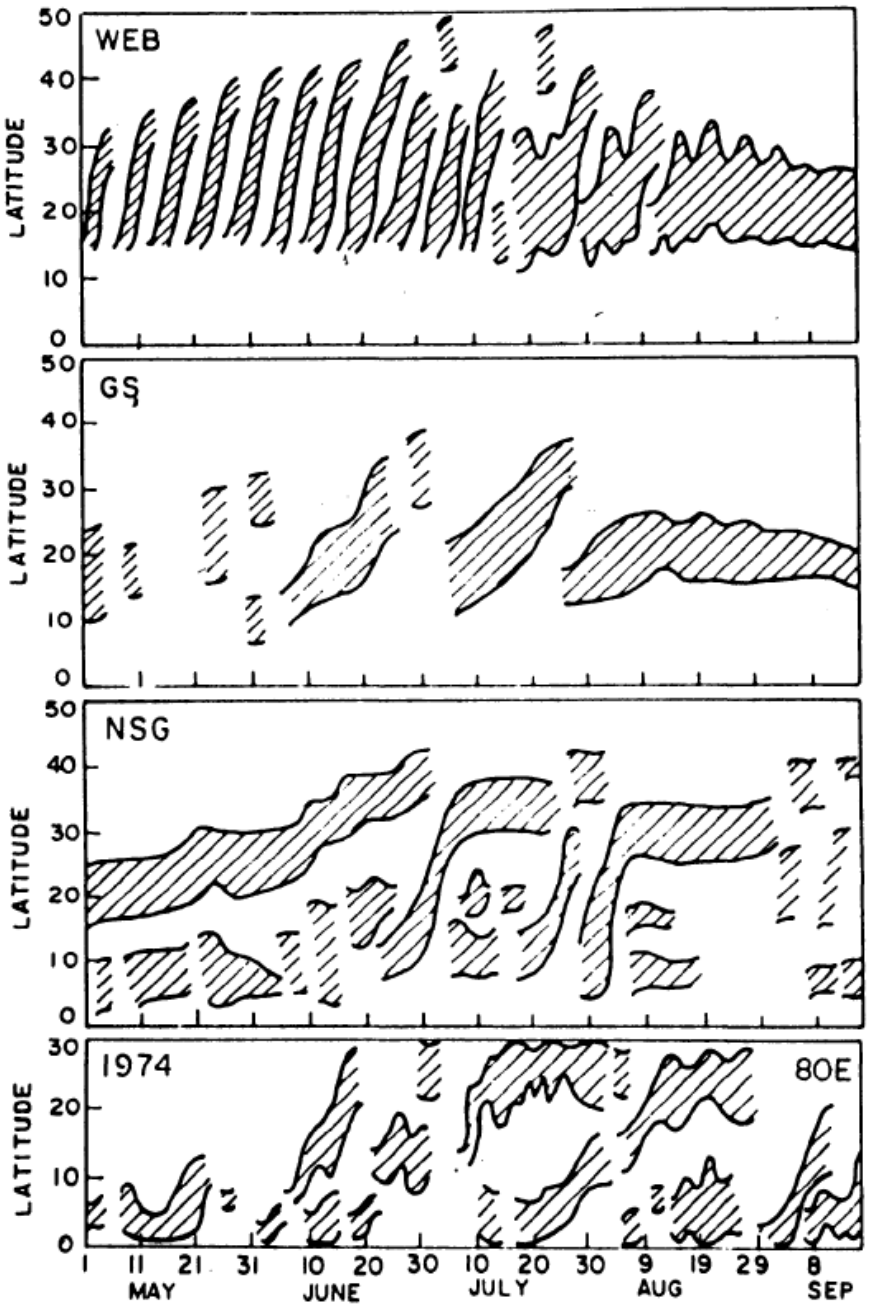

Nanjundiah, Srinivasan and Gadgil, 1992, JMSJ

Fig. 6. Time-latitude section of the region with upward vertical velocity larger than 30 hpa $\sec^{-1}$ from a) Webster Model (After Webster and Chou, 1980b) (WEB) b) Modified Version of Webster Model (after Gadgil and Srinivasan, 1990)) (GS) c) Present Model (NSG) d) Variation of the maximum cloudiness zone at 80°E in the year 1974. (After Sikka and Gadgil, 1980)

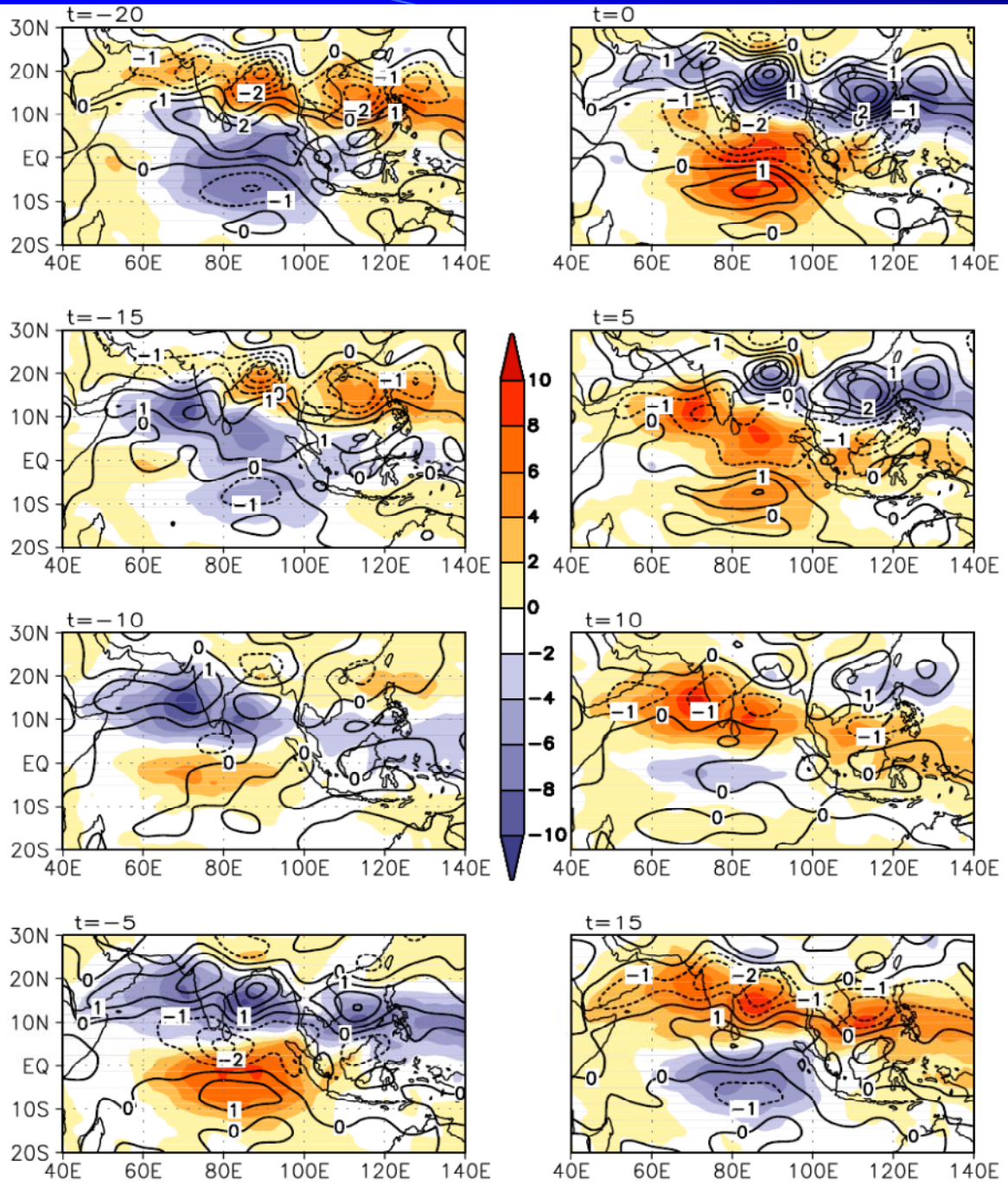

What is responsible for the northward propagation?

Regressed OLR (shaded) and 850 hPa relative vorticity (contour) w.r.t a reference time series of 10-90 day filtered OLR over CI

Goswami, 2005: ISV book

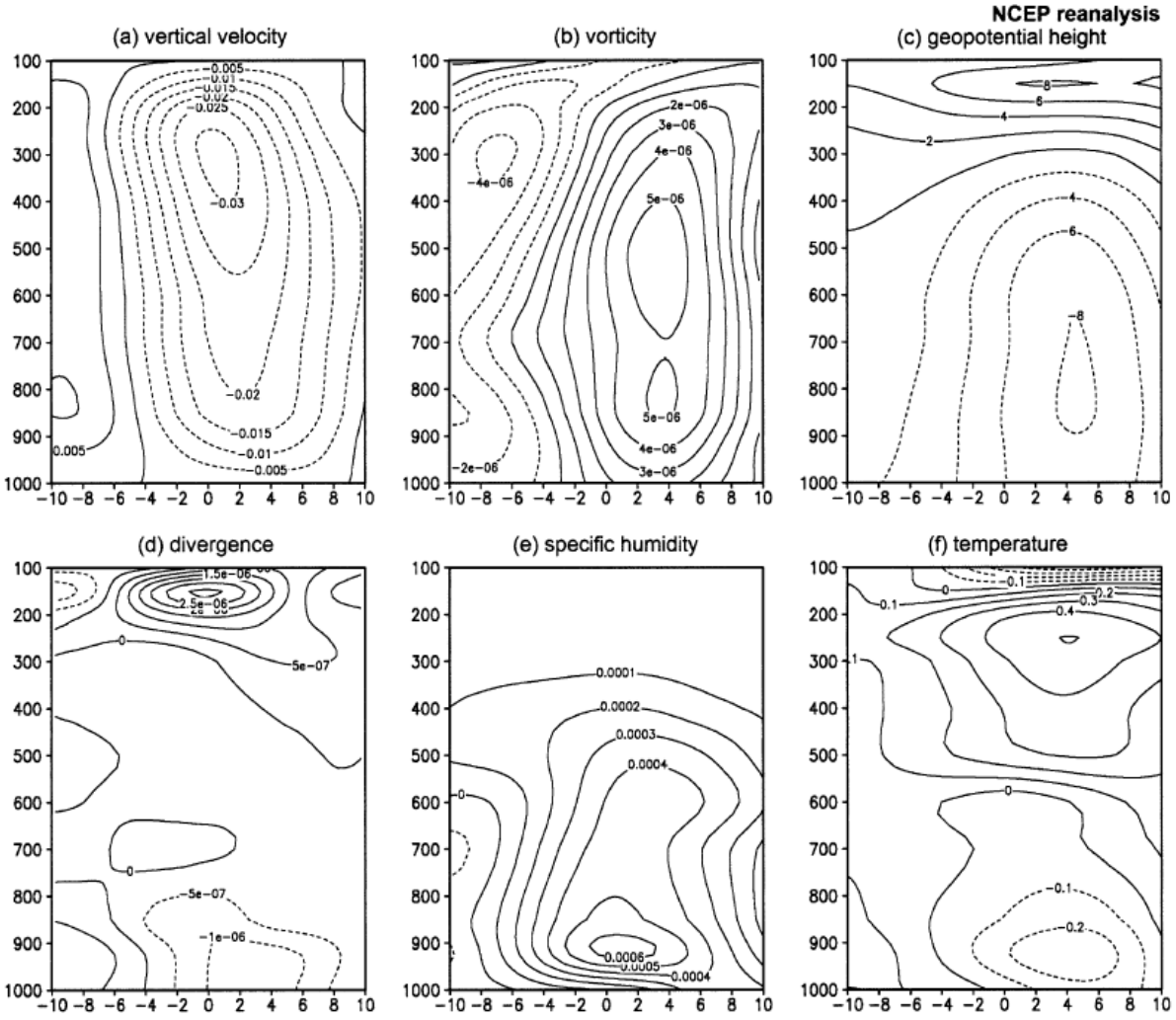

FIG. 8. As in Fig. 7 except for the NCEP–NCAR reanalysis.

FIG. 7. Meridional–vertical structures of the northward propagating BSISO mode derived from the ECHAM model: (a) vertical velocity (hPa s^{-1}), (b) vorticity (s^{-1}), (c) geopotential height (dam), (d) divergence (s^{-1}), (e) specific [redacted] temperature (K). Horizontal axis is the meridional distance (°lat) with respect to the convection center. The positive (negative) value means to the north (south) of convection center. The vertical axis is the pressure (hPa).

Jiang et al. 2004, J. Climate

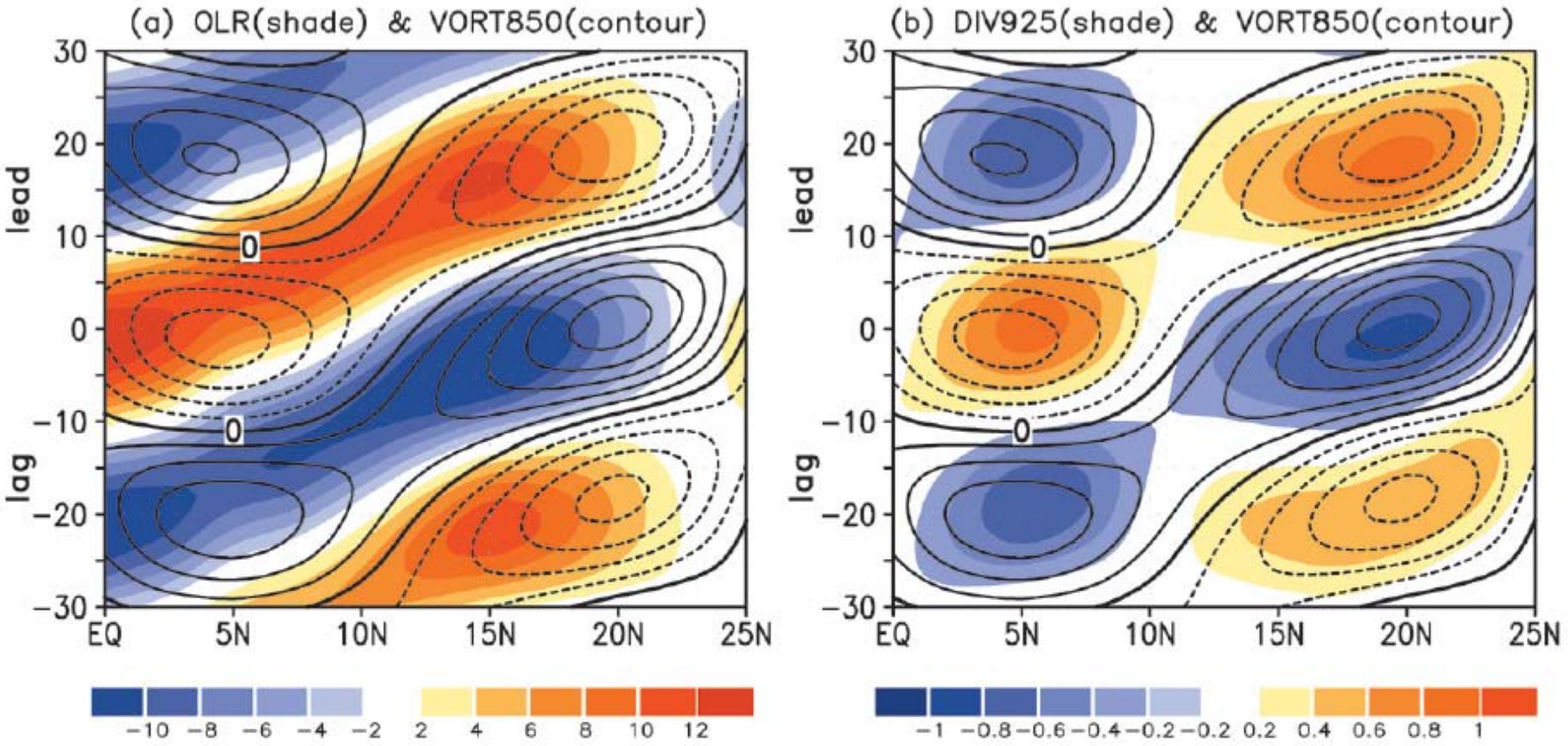

Figure 2.16. (a) Regressed 30 to 60-day filtered anomalies of OLR (shaded; $W\,m^{-2}$) and 850 hPa relative vorticity (contour, positive solid and negative dashed, contour interval $1 \times 10^{-6}\,s^{-1}$) with respect to the reference time series described in Figure 2.10 averaged over 80°E–90°E. (b) Regressed 30 to 60-day filtered anomalies of 850 hPa relative vorticity (contour, positive solid and negative dashed, contour interval $1 \times 10^{-6}\,s^{-1}$) and divergence at 925 hPa (shaded; $10^{-6}\,s^{-1}$) with respect to the same reference time series.

What is responsible for making the low level moisture convergence north of the heat source?

Jiang , Wang and Li (2004, J. Climate, 17, 1022-1039)

- They show that response of a heat source in the presence easterly mean flow leads to cyclonic barotropic vorticity centered slightly to the north of the heat source.
- It drives frictional convergence in the boundary layer north of the heat source.
- Near the equator, positive meridional gradient of low level mean humidity leads to anomalous moisture convergence north of the heat source.

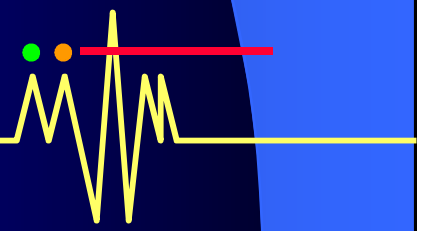

this model, there are a 2-layer free atmosphere and a well-mixed PBL. For simplicity we consider a 2D case with vanished zonal gradients for all variables. The governing equations for a linear motion on an f plane under a constant vertical shear of the mean zonal flow can be written as

$$\frac{\partial \zeta_-}{\partial t} + f_0 D_- = -\overline{u}_T \frac{\partial D_+}{\partial y} + K\nabla^2 \zeta_-, \quad (1)$$

$$\frac{\partial D_-}{\partial t} - f_0 \zeta_- + \nabla^2 \phi_- = K\nabla^2 D_-, \quad (2)$$

$$\frac{\partial \zeta_+}{\partial t} + f_0 D_+ = \overline{u}_T \frac{\partial}{\partial y}(2D_+ + D_-) + K\nabla^2 \zeta_+, \quad (3)$$

$$\frac{\partial D_+}{\partial t} - f_0 \zeta_+ + \nabla^2 \phi_+ = K\nabla^2 D_+, \quad (4)$$

$$\frac{\partial \phi_-}{\partial t} - f_0 \overline{u}_T v_+ + c_0^2(1 - I)D_- = c_0^2(B - 1)D_+ + K\nabla^2 \phi_-, \quad (5)$$

where $\overline{u}_T = (\overline{u}_1 - \overline{u}_3)/2$ denotes the constant vertical shear of the mean flow and f_o is the Coriolis parameter at a reference latitude (12°N). Variables with a subscript, + (−), represent a barotropic (baroclinic) mode. The

Jiang, Li and Wang, 2004, J. Climate

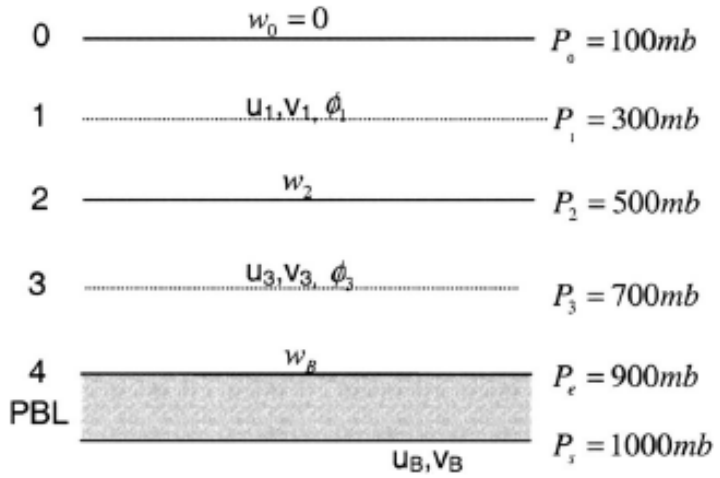

FIG. 9. Vertical structure of the 2½-layer model (Wang and Li 1993).

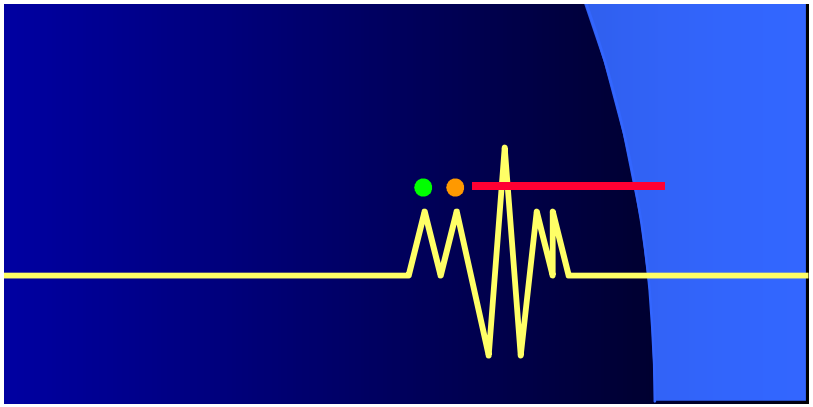

$$\frac{\partial \zeta_+}{\partial t} \propto \overline{u}_T \frac{\partial D_-}{\partial y}. \qquad (9)$$

The generation of the barotropic vorticity may further lead to the development of the barotropic divergence in the free atmosphere:

$$\frac{\partial D_+}{\partial t} \propto f_0 \zeta_+. \qquad (10)$$

Equation (9) implies that the baroclinic and barotropic modes are closely coupled in the presence of the vertical shear of the mean flow. In reality, the vertical structure of the atmospheric mean flow in boreal summer is characterized by a strong easterly shear in the monsoon region.

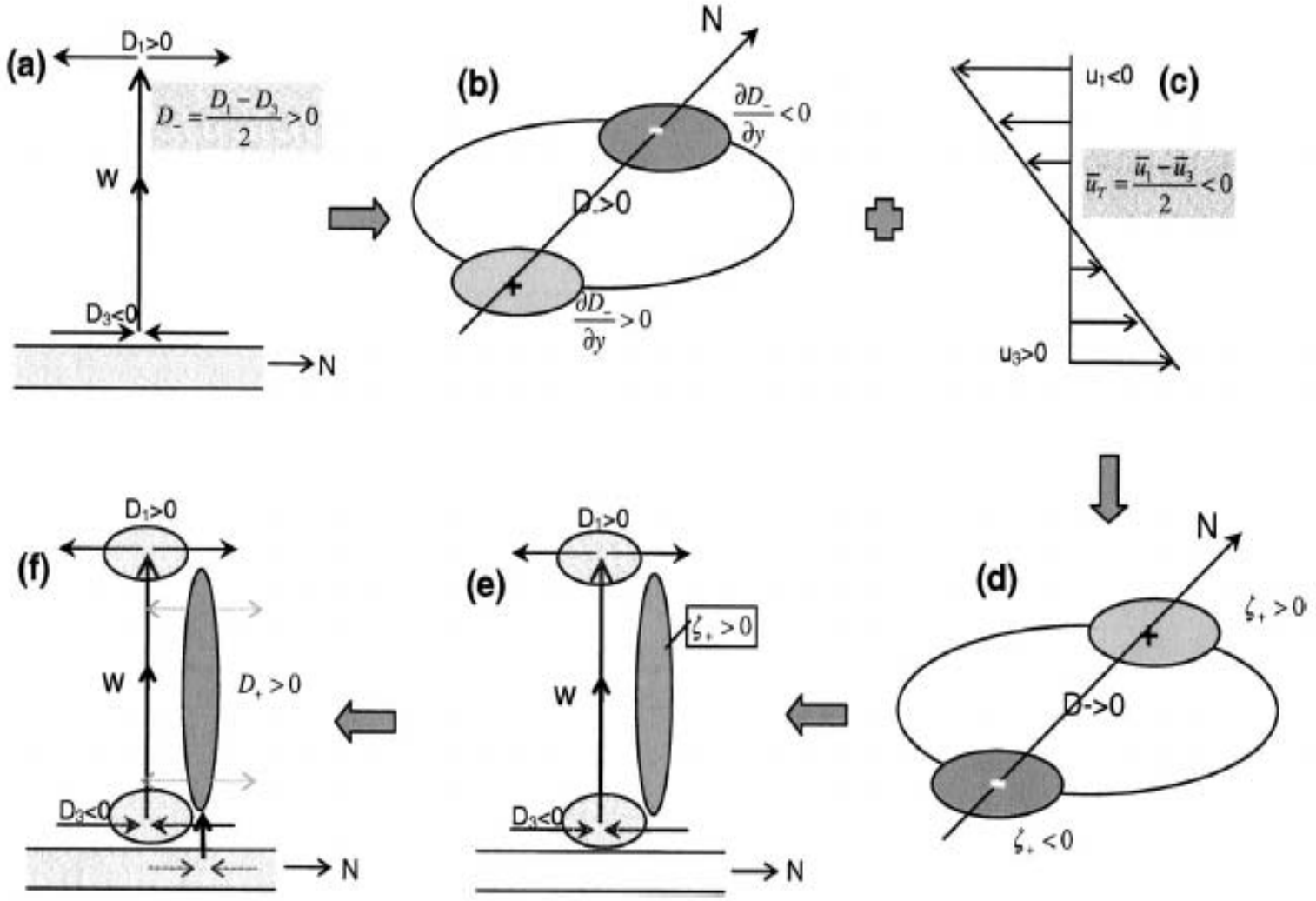

FIG. 10. Schematic diagram for the vertical shear mechanism. (a) Consider initially an ISO convection with a baroclinic structure. (b) This leads $\partial D_-/\partial y < 0$ ($\partial D_-/\partial y > 0$) north (south) of the convection center. (c) In the presence of the easterly shear of the mean flow, (d), (e) a positive barotropic vorticity is induced north of the convection, leading to (f) a barotropic divergence in situ. The latter further leads to a PBL convergence and thus a northward shift of convective heating.

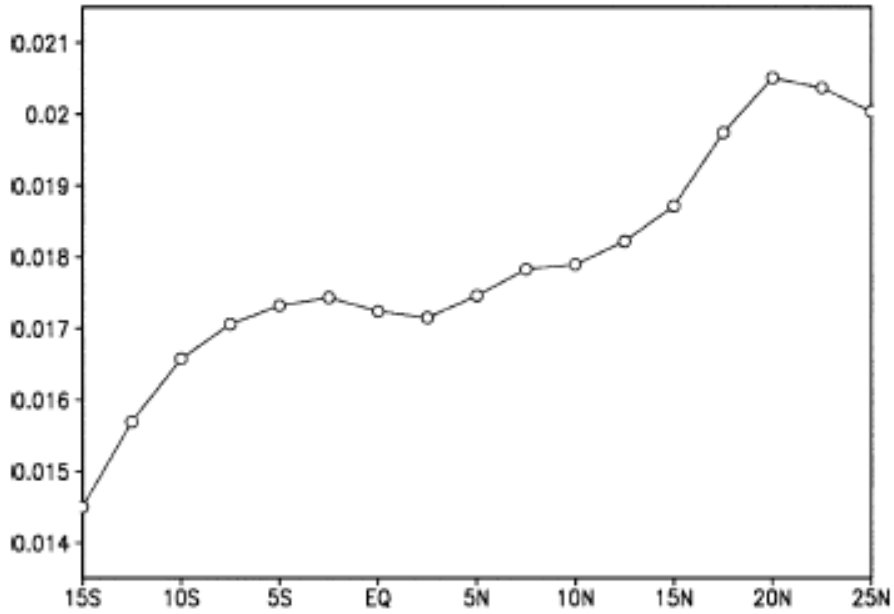

FIG. 13. Meridional profile of the summer mean specific humidity (kg kg^{-1}) at 1000 mb averaged between 70° and 95°E.

Near the equator, the wind shear mechanism does not work. Here, a positive gradient of mean q leads to anomalous moisture converngence to the north of the heat source

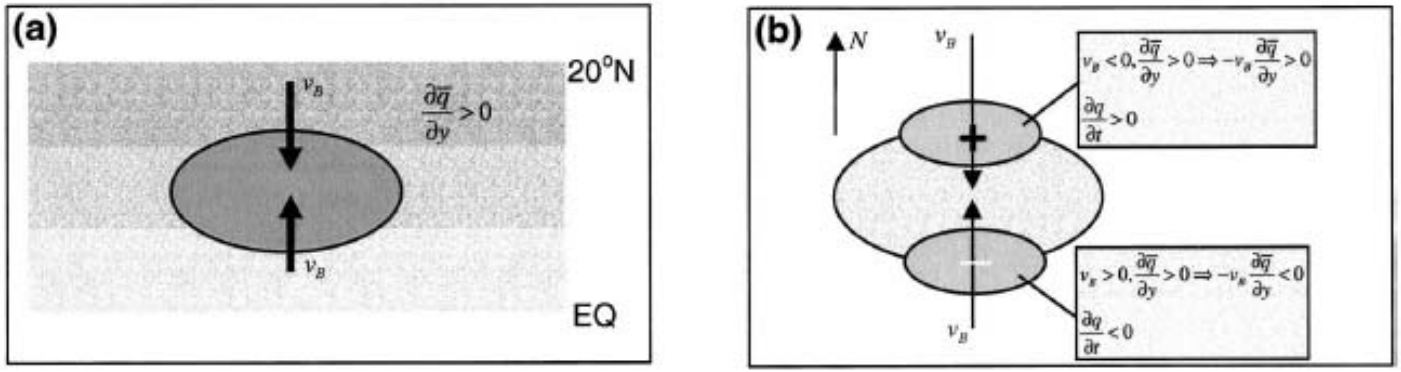

FIG. 14. Schematic diagram for the mechanism of moisture advection by the ISO wind in the presence of the mean specific humidity gradient. The meridional asymmetric mean specific humidity field is advected by convection-induced perturbation wind, (a) southward to the north of a convection center and northward to the south, which leads to a (b) positive moisture perturbation to the north and negative to the south of the convection center. As a result, the convection tends to move northward.

What is responsible for the oscillation in the 30-60 day time scale?

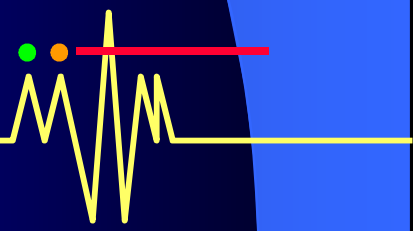

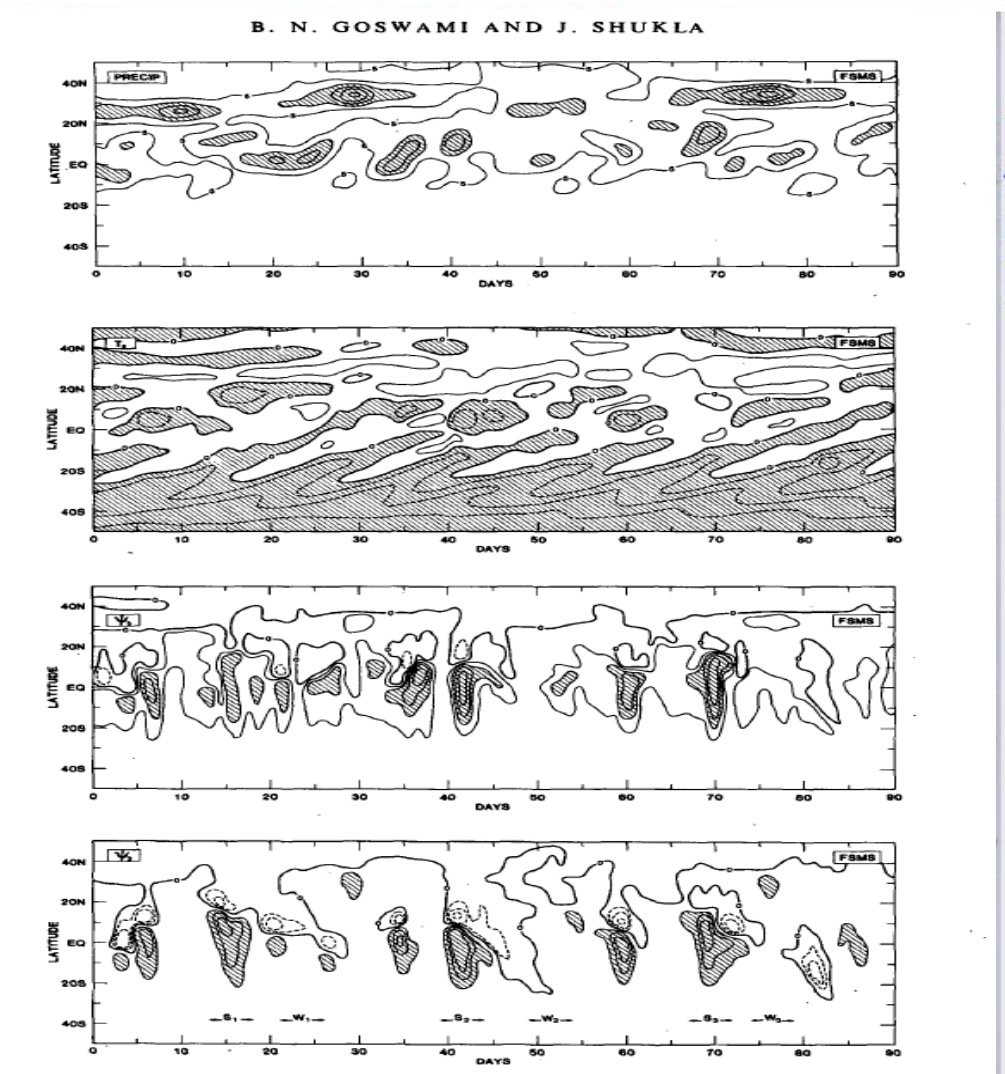

FIG. 4. As in Fig. 2 but for the fixed soil moisture, summer (FSMS) run. A unit of 300 is subtracted from the *TS* field and negative areas are shaded. Contour interval for *TS* and *P* is 10, and that for ψ_5 is 25. For ψ_2, negative contour interval is 10 and positive contour interval is 20. For *P*, contours greater than 15 are shaded, for ψ_5 contours greater than 50 are shaded while for ψ_2, contours greater than 20 are shaded.

Model simulates realistic fluctuation (period about one month) and northward propagation of rain band.

Meridional gradient of stream function is proportional to vertical velocity.

Shows fluctuations of the mean meridional circulation (Hadley Circ with same period

Figure 10: Latitude-time plot of some simulated fields by the GLAS Symmetric climate model.

Goswami and Shukla, 1984, JAS

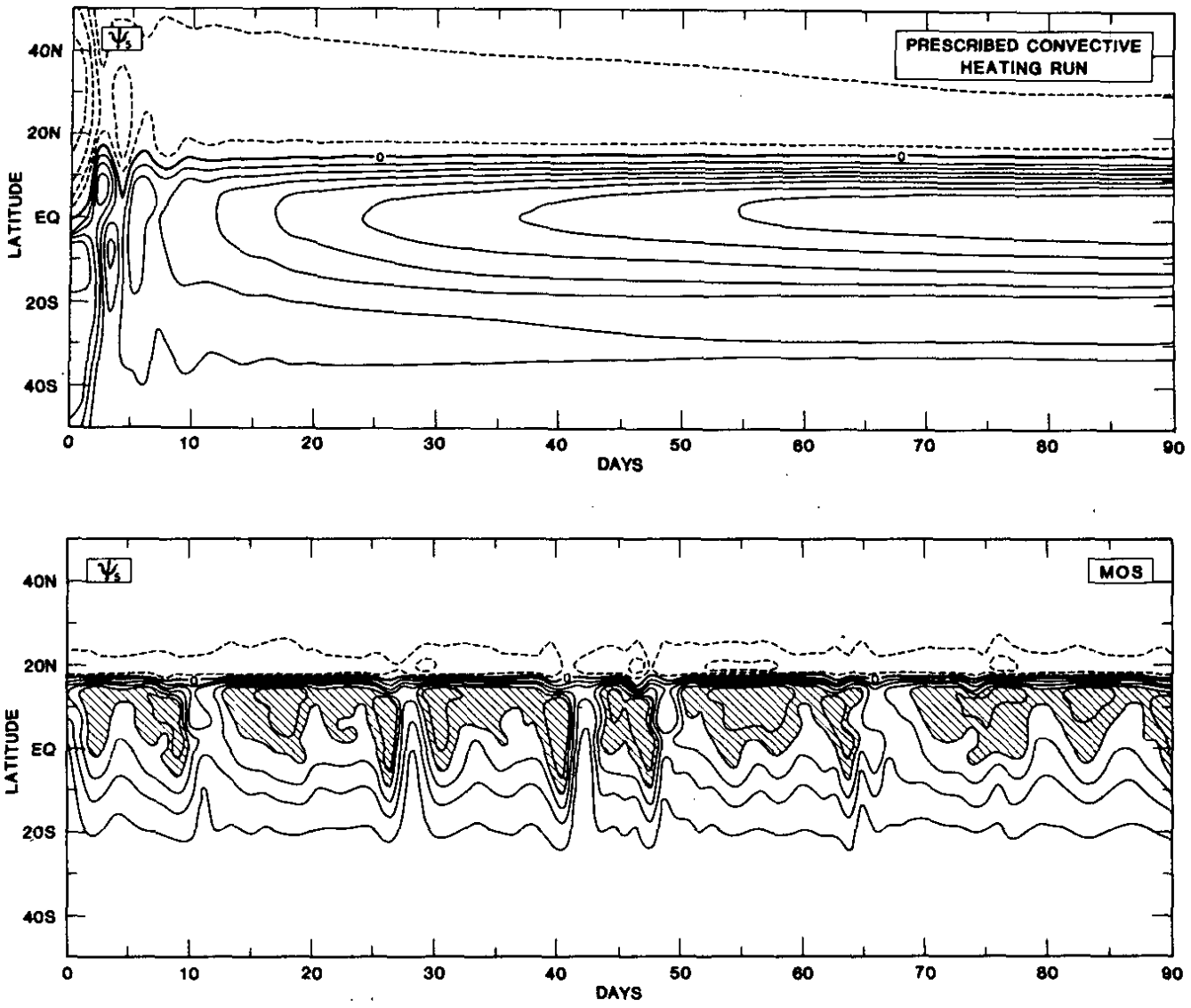

FIG. 3. Time series of ψ_5 for a run with prescribed latent heating (upper panel) and dynamically determined heating (lower panel) for the all-ocean summer run (MOS). Units 10^{10} kg s^{-1}.

What makes the TCZ oscillate with 30-60 day periodicity?

Goswami and Shukla (1984, JAS) proposed a convective-radiative-dynamical feedback to explain this temporal scale selection

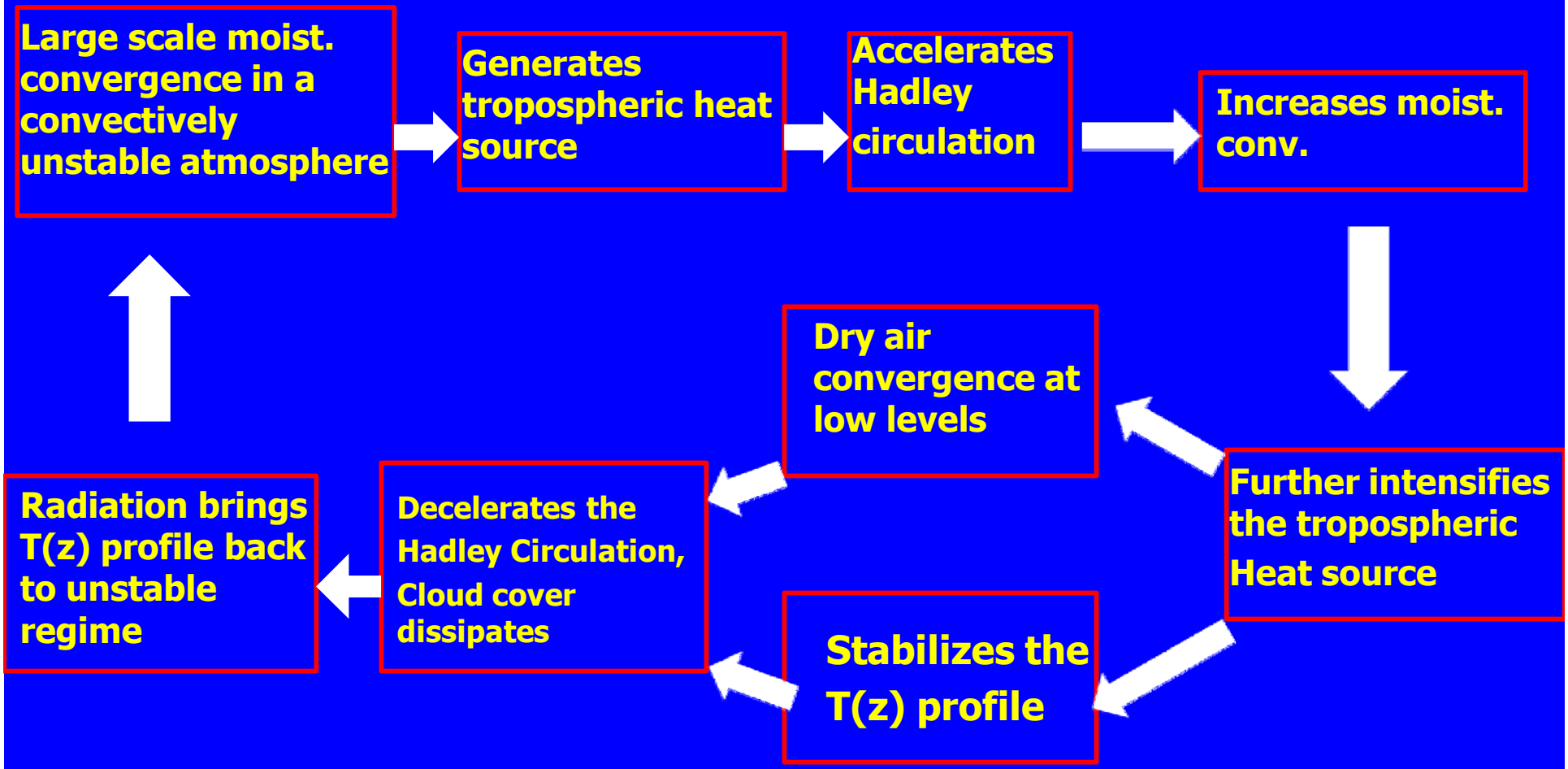

The 10-20 day mode:
Structure and Mechanism for generation

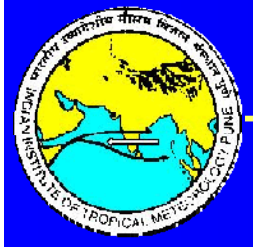

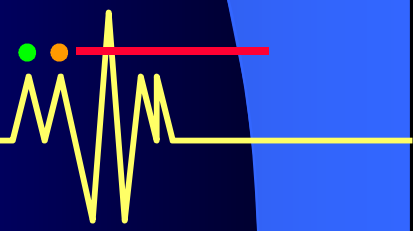

Summer composite

850 hPa 10-20 day filtered winds and OLR for two opposite phases (a,b) of the QBM . (c) Relative vorticity (x 1.0e+6) averaged between 5S-5N as a function 15 phases

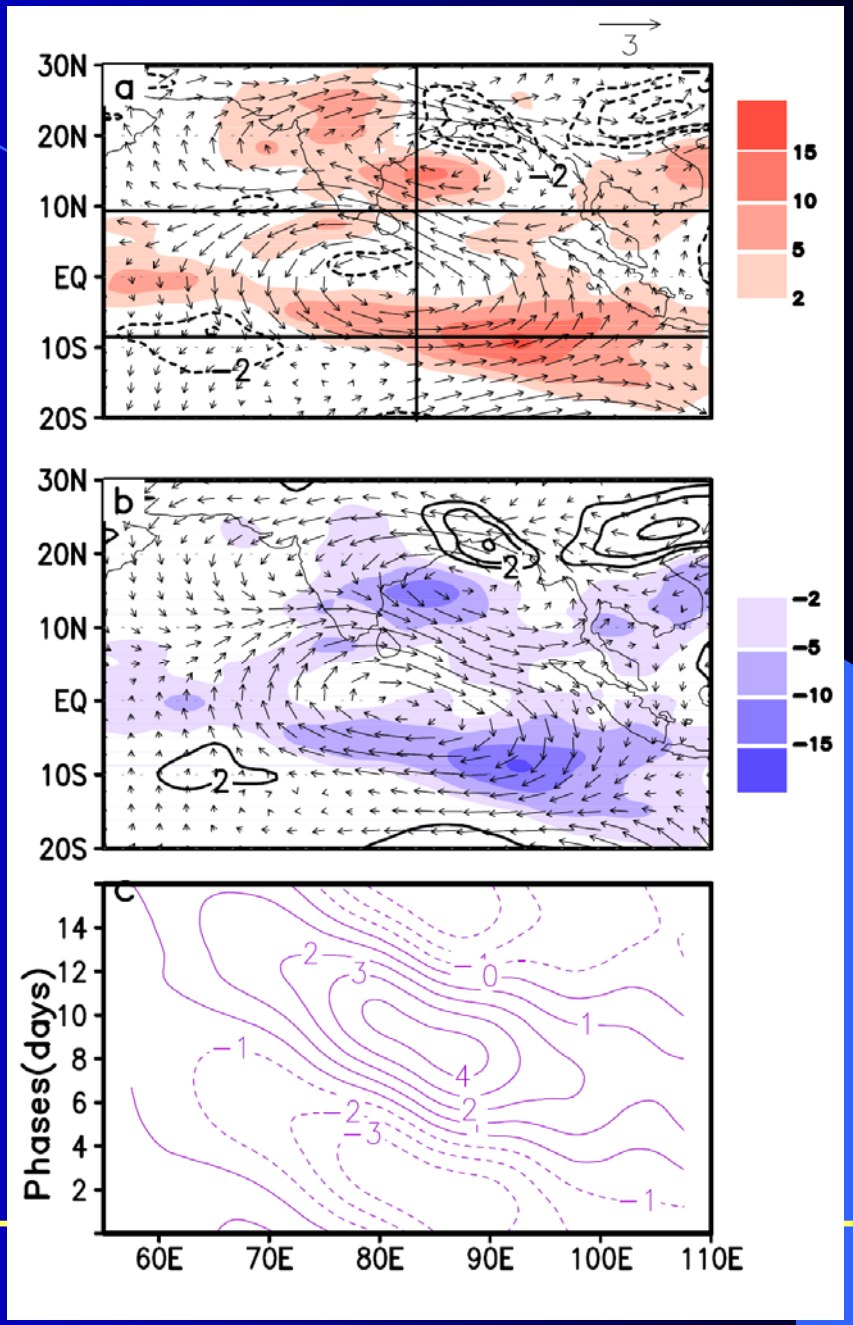

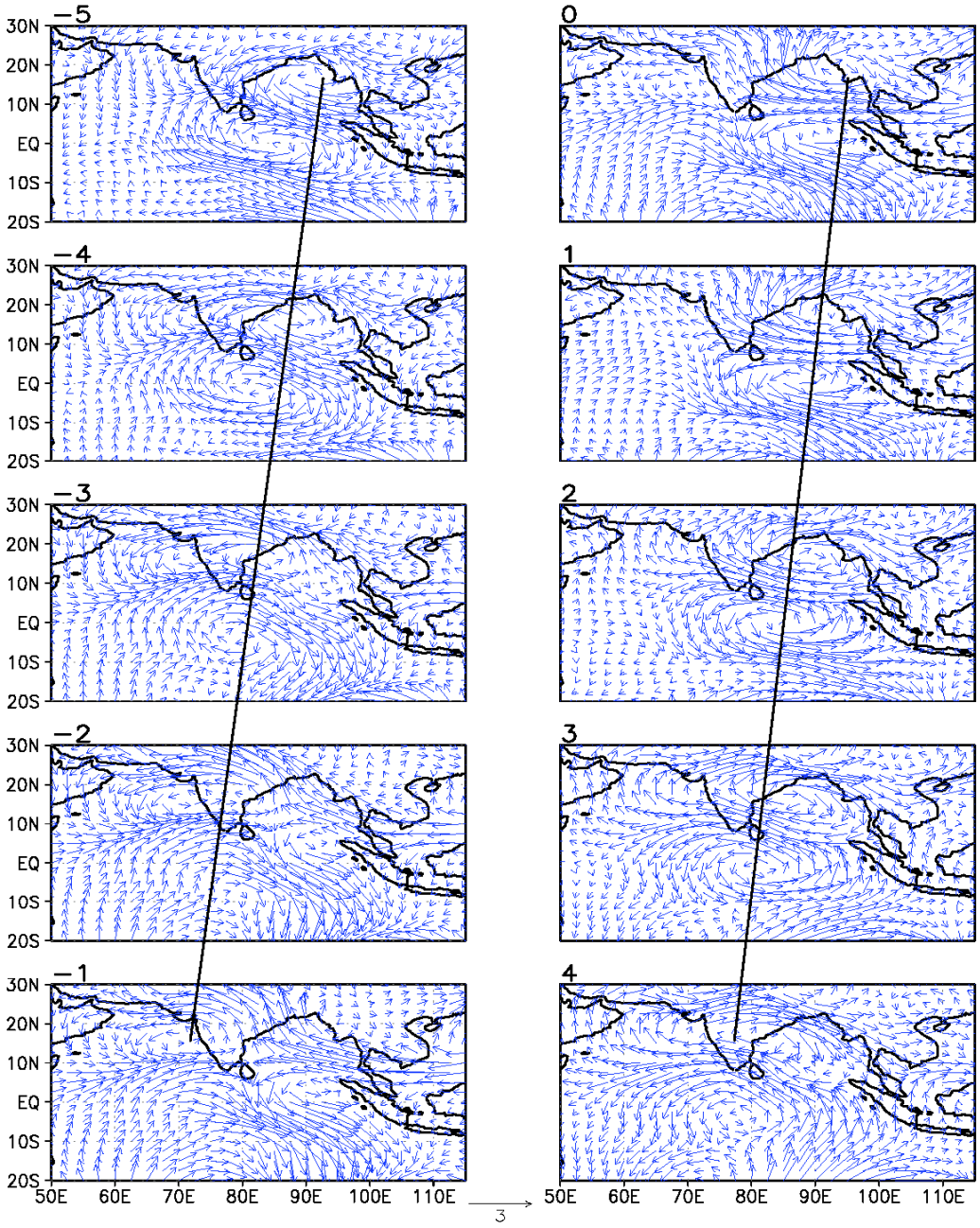

Figure 5: Composites of different phases showing generation and westward movement of vortices. The scale for wind vectors is same for all levels and shown at the bottom.

Composite structure for different phases.

Westward phase propagation of the two vortices is evident

Winter composite

850 hPa 10-20 day filtered winds and OLR for two opposite phases (a,b) of the QBM . (c) Relative vorticity (x 1.0e+6) averaged between 5S-5N as a function 15 phases

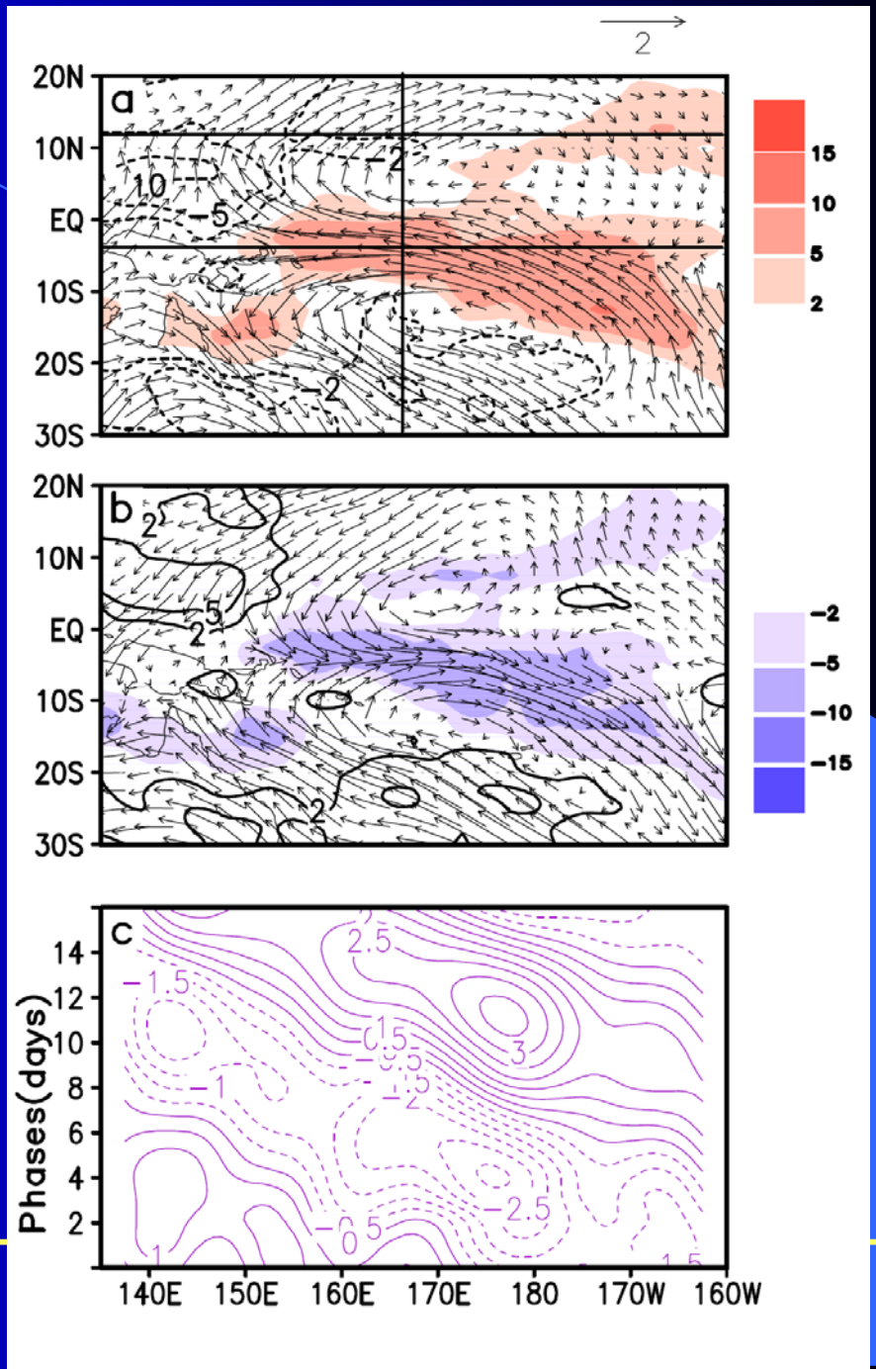

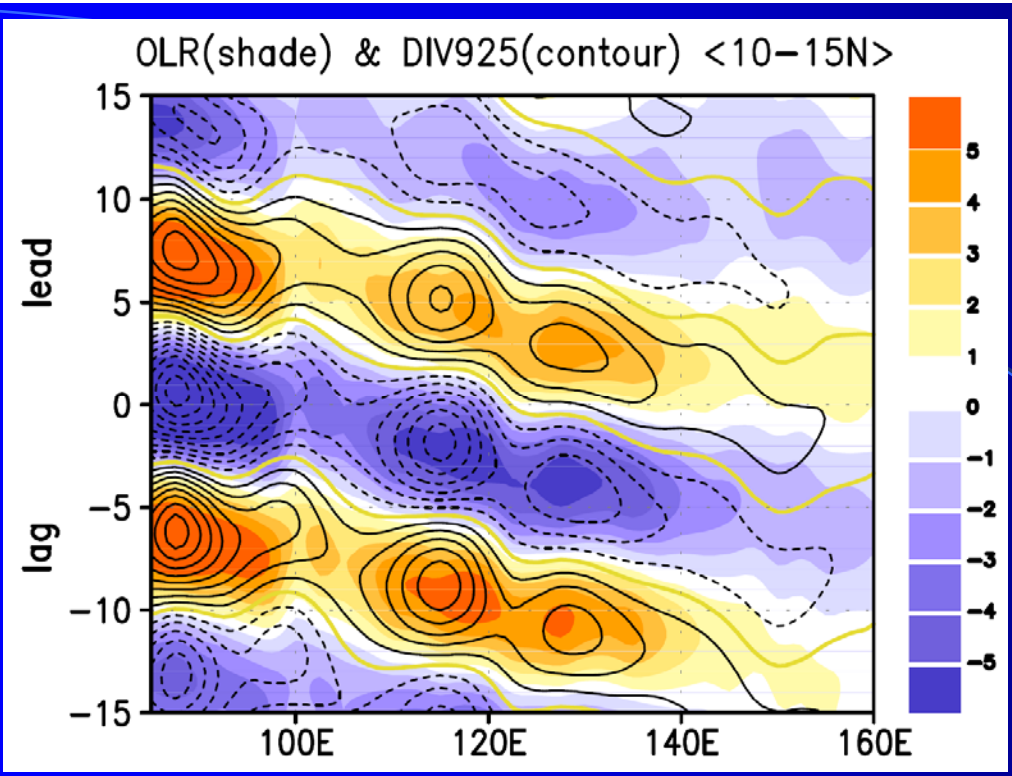

Lag-longitude plot of Regression of 10-20 day filtered OLR and 925 hPa div. on the QBM index averaged between 10N-15N.

Div. Maximum (minimum) at 925 hPa (BL) is west of the OLR maximum (minimum).

→BL moisture convergence makes convection move westward

→Convective coupling

Chatterjee and Goswami, 2004, QJRMS

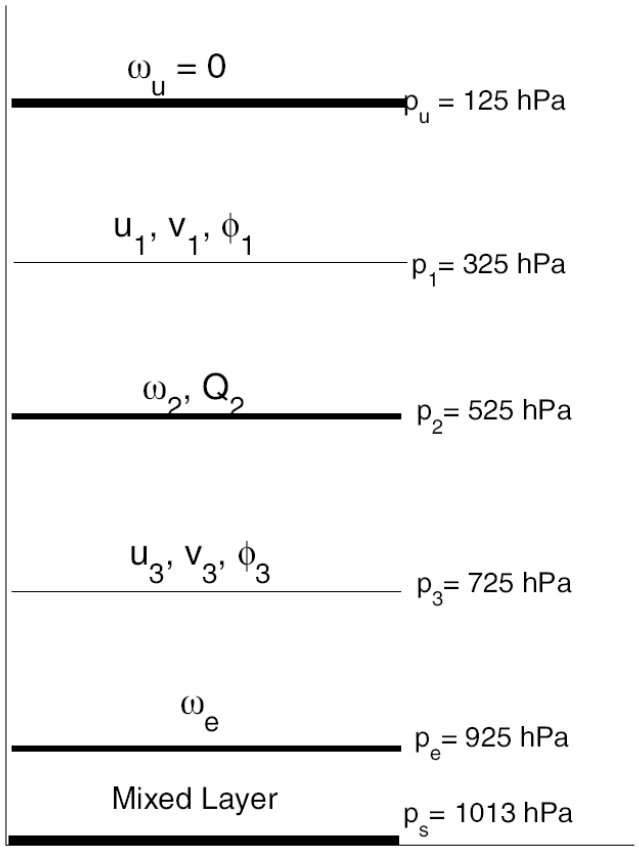

Figure 6. The vertical structure of the model.

Momentum eqns.at levels 1 and 3 while the thermodynamic energy eqn.at level 2.

Define barotropic and baroclinic components as

$$\chi_c = (\chi_3 - \chi_1)/2 \text{ and } \chi_t = (\chi_3 + \chi_1)/2,$$

Where χ represents zonal and meridional winds u and v or geopotential Φ, $\bar{U}$ represents mean background flow.

Results: The control case; No mean flow, No EWF

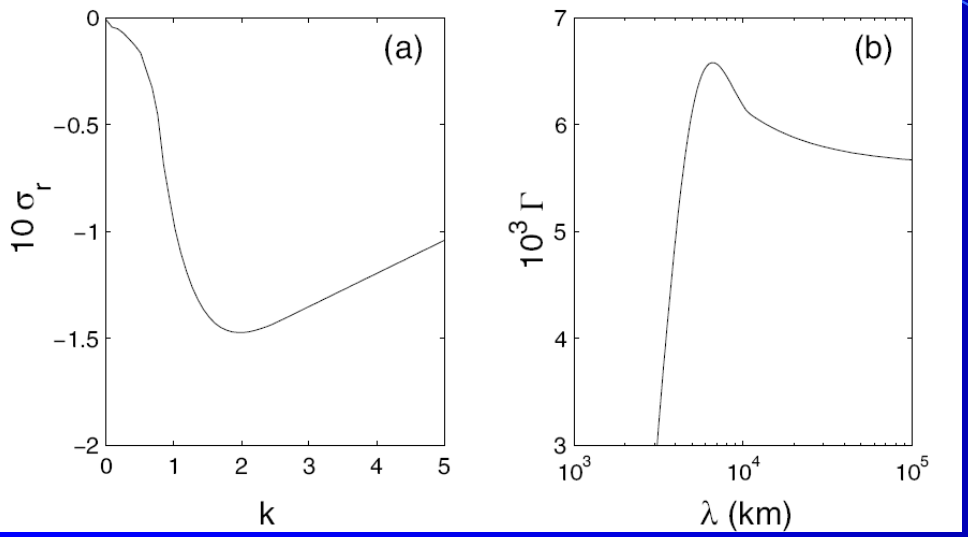

(a) Wavenumber vs real freq.

(b) Growth rate Γ vs wave length

Max Growth for k=1.33, or λ=6750 km. Period=16 days, Cp= 4.8 m/s

Structure of the most unstable , n = 1 Rossby mode

Vortices symmetric about the equator

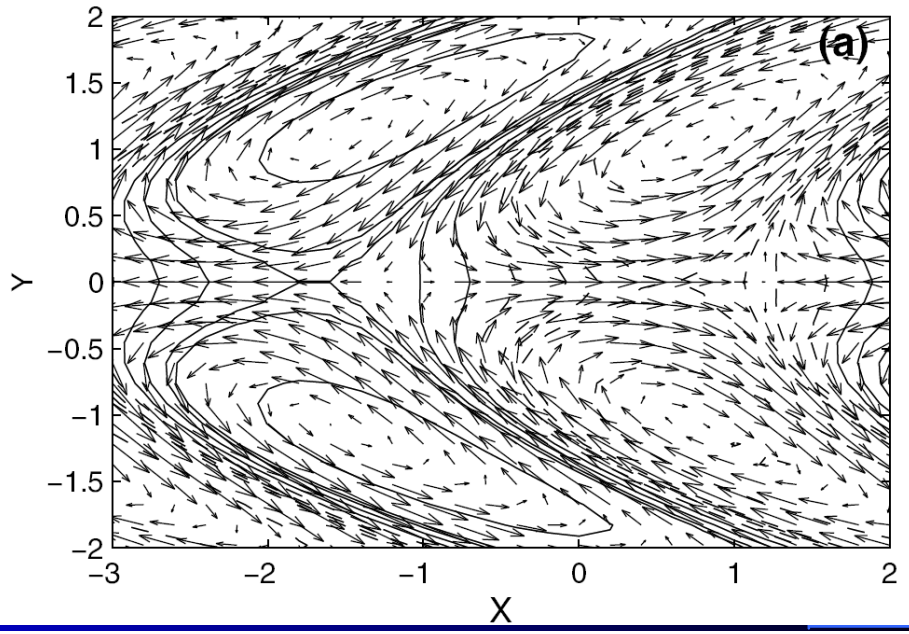

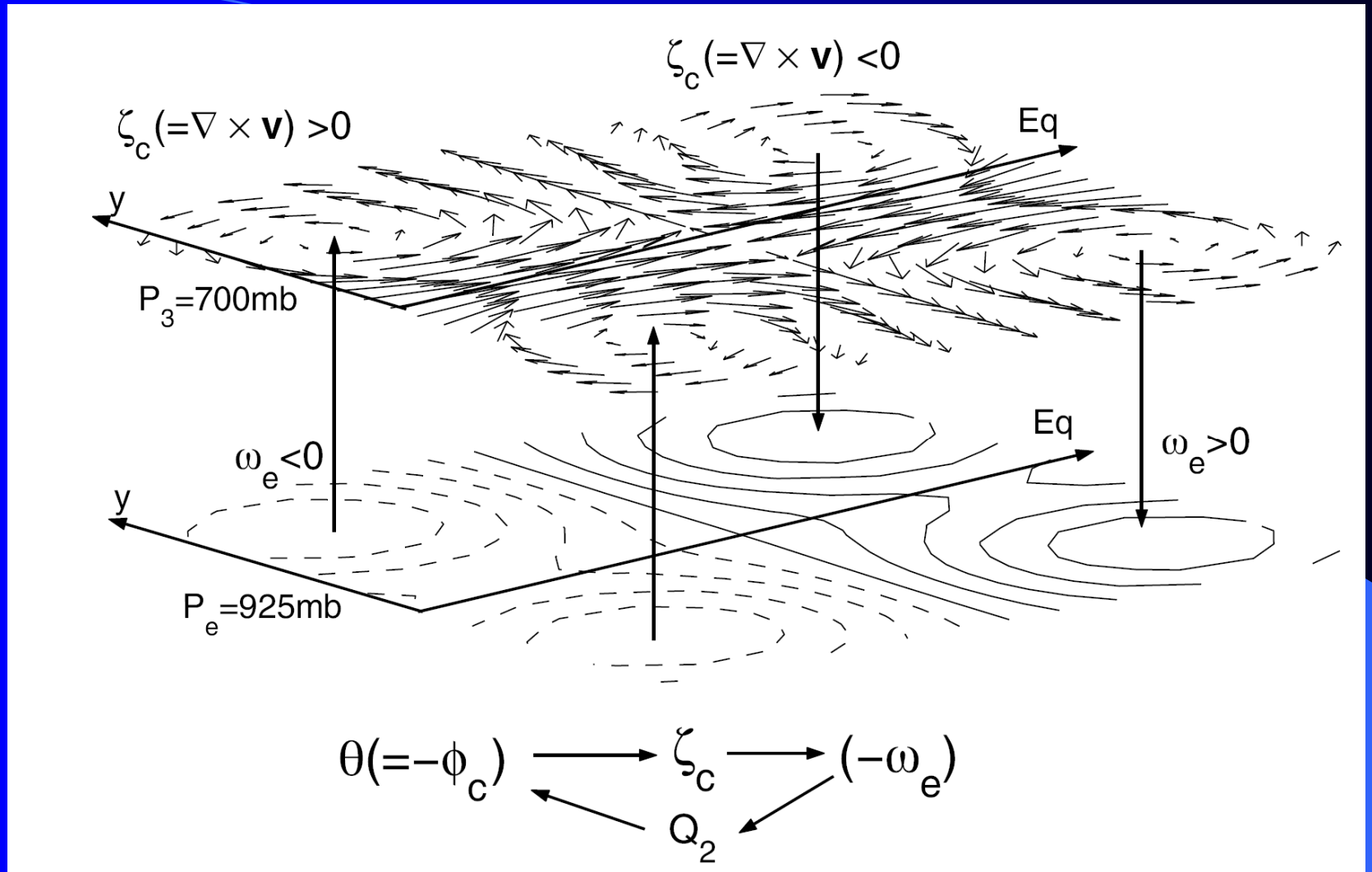

Schematic illustrating the Wave-Boundary-Layer-CISK for the unstable mode

Role of the mean background flow on the unstable mode:

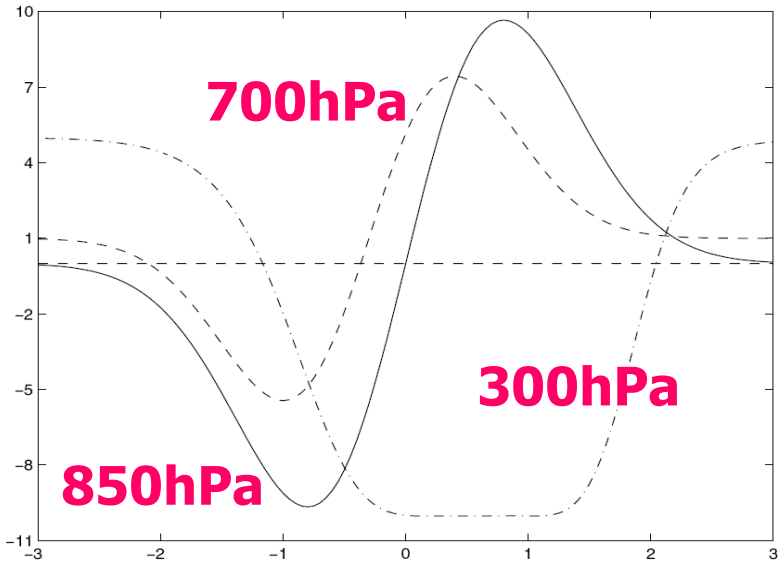

T=17 days, λ = 6020 km

Cp = 4.1 m/s

Spatial structure of the unstable mode with mean flow.

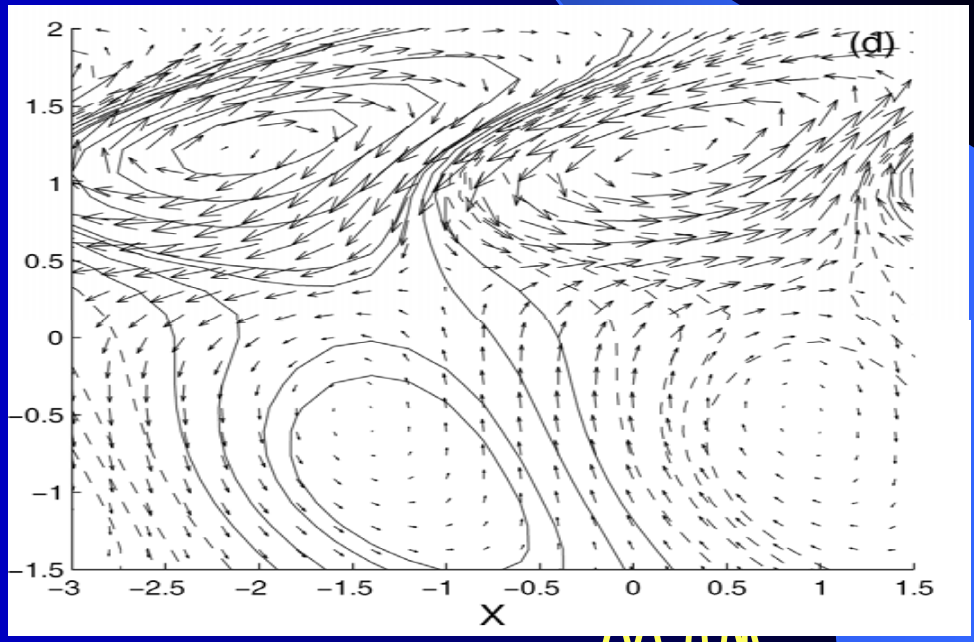

Climatological zonal winds for July averaged between 40E-120E

Vertical shear of mean winds:

Not essential for the basic instability. When included makes the structure more realistic.

Evaporation wind feedback:

Again not essential for the basic instability. When included enhances the growth rate of the unstable mode without changing the period and phase speed substantially.

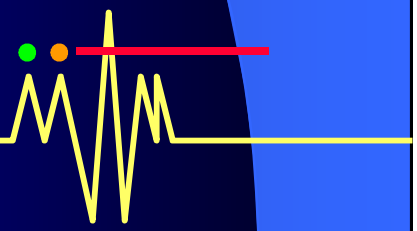

Importance of QBM in Tropical Intraseasonal Variability

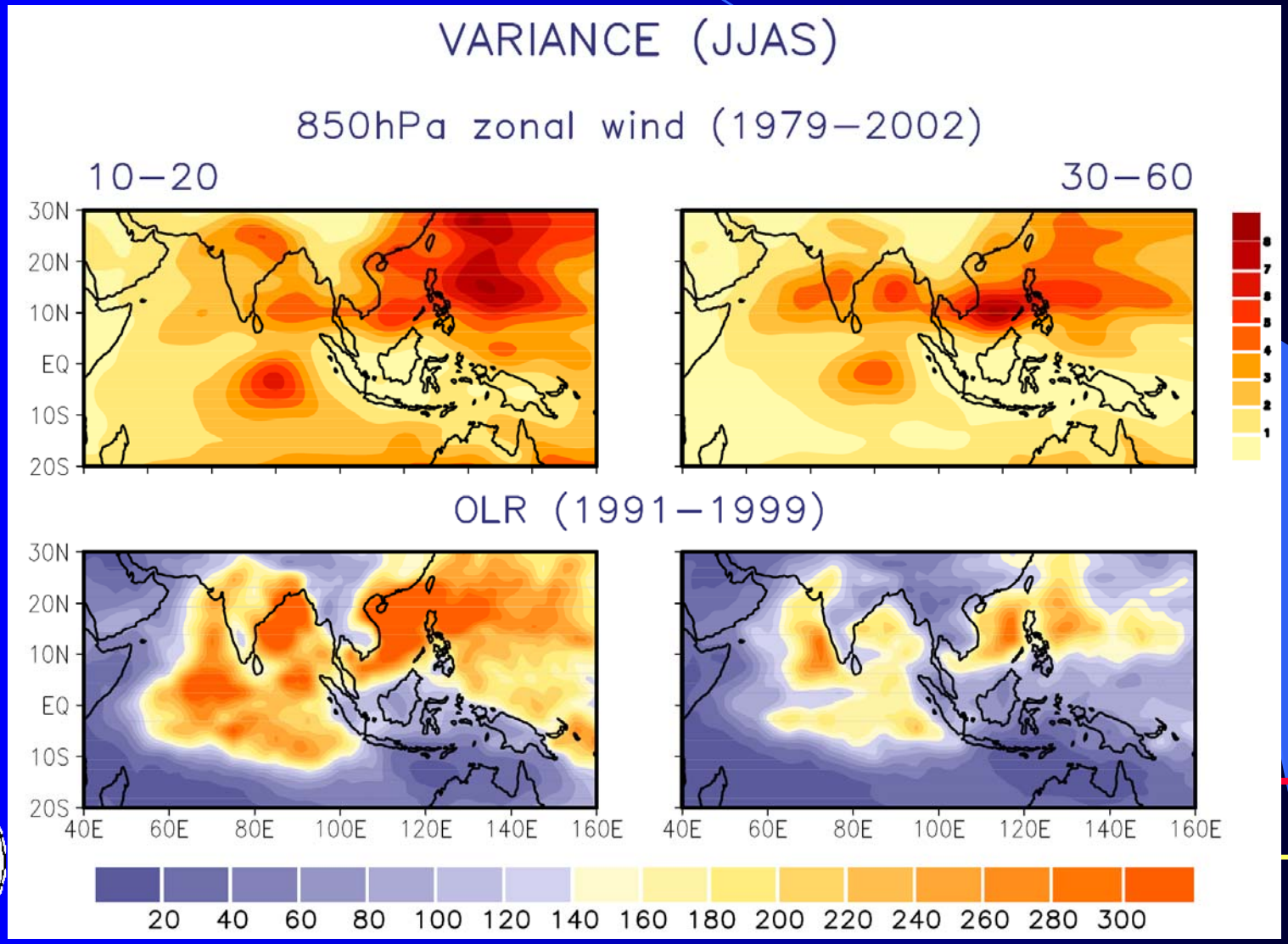

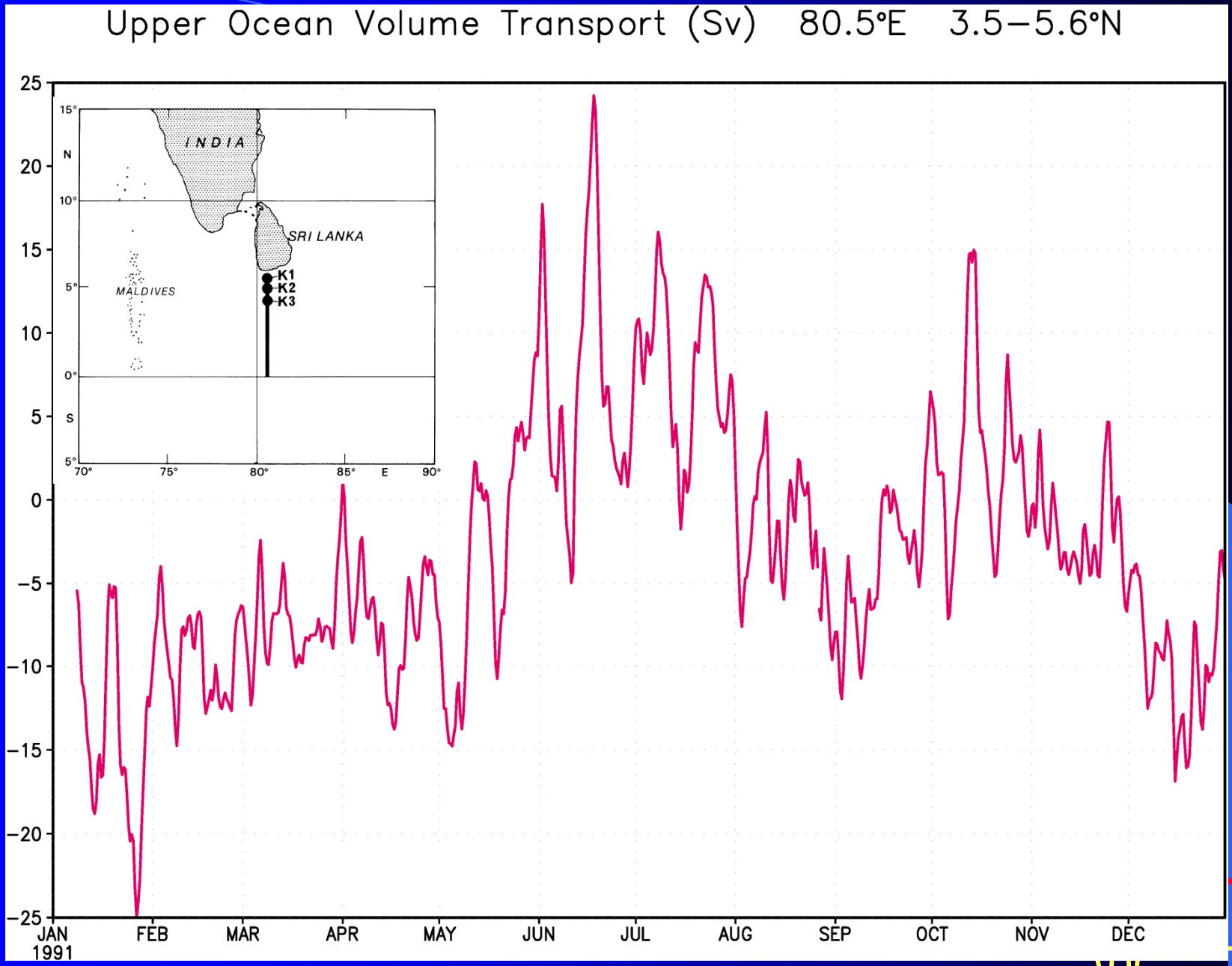

Schott et al., 1994, JGR

MERIDIONAL VELOCITY (cm s^{-1}) 90°E EQUATOR

OBSERVATION *(Masumoto, Murty et al., Presented at IOGOSS Conference, Mauritius, November 2002)*

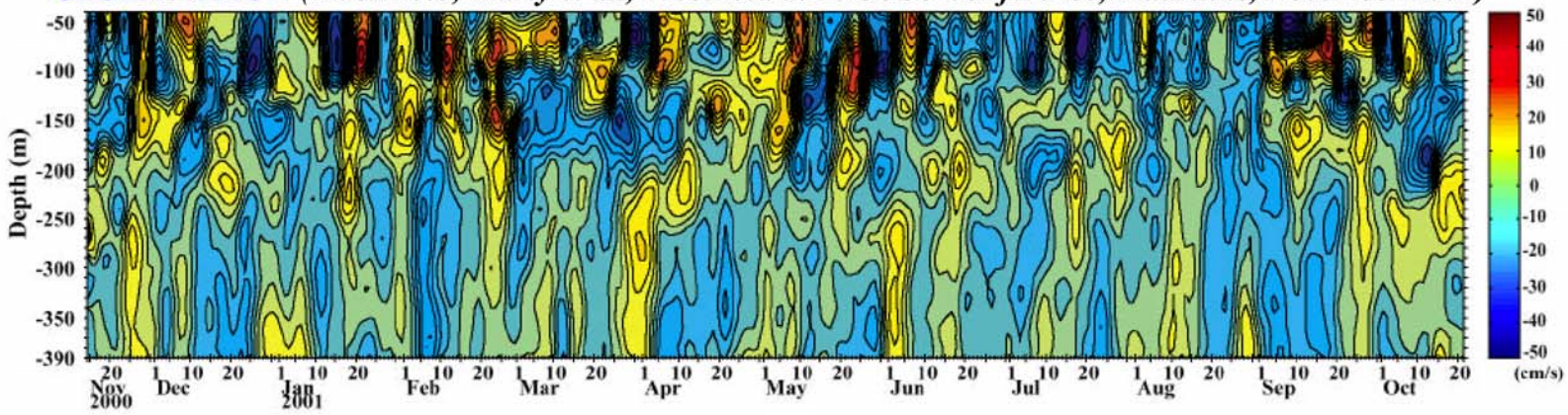

From Sengupta et al, 2007, J. Climate

MODEL

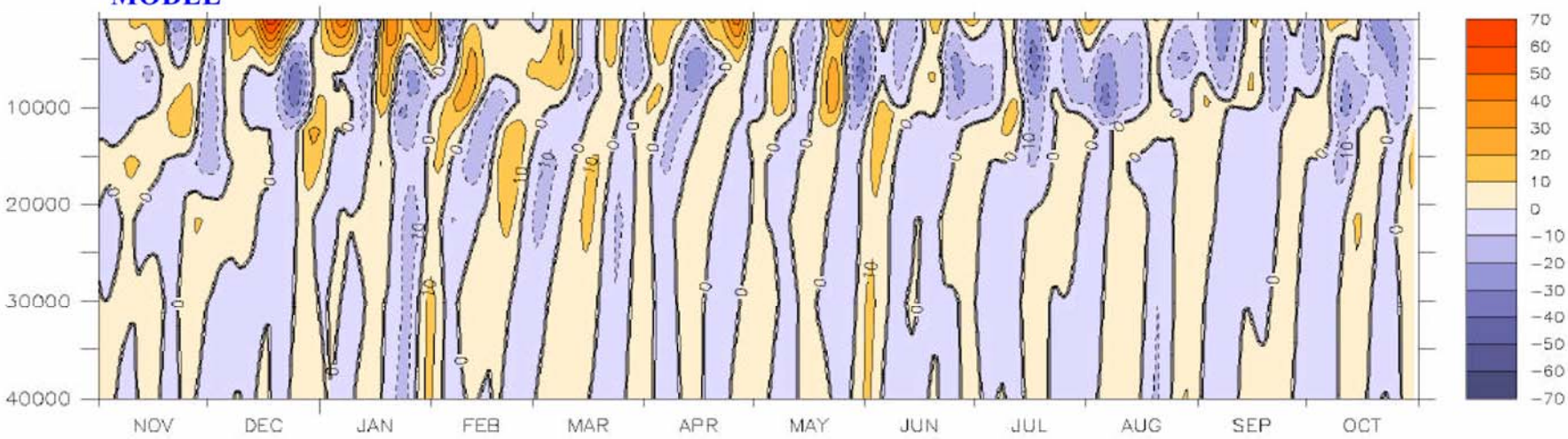

SST variability: mainly 14-day Yanai waves at all depths + 30-60 day ?? below ~150m

What role ocean-atmosphere coupling play in existance of the MISO and its northward propagation?

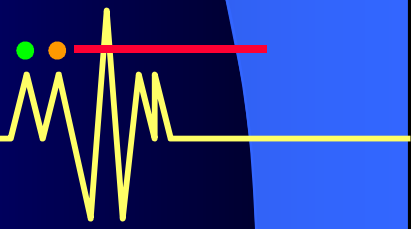

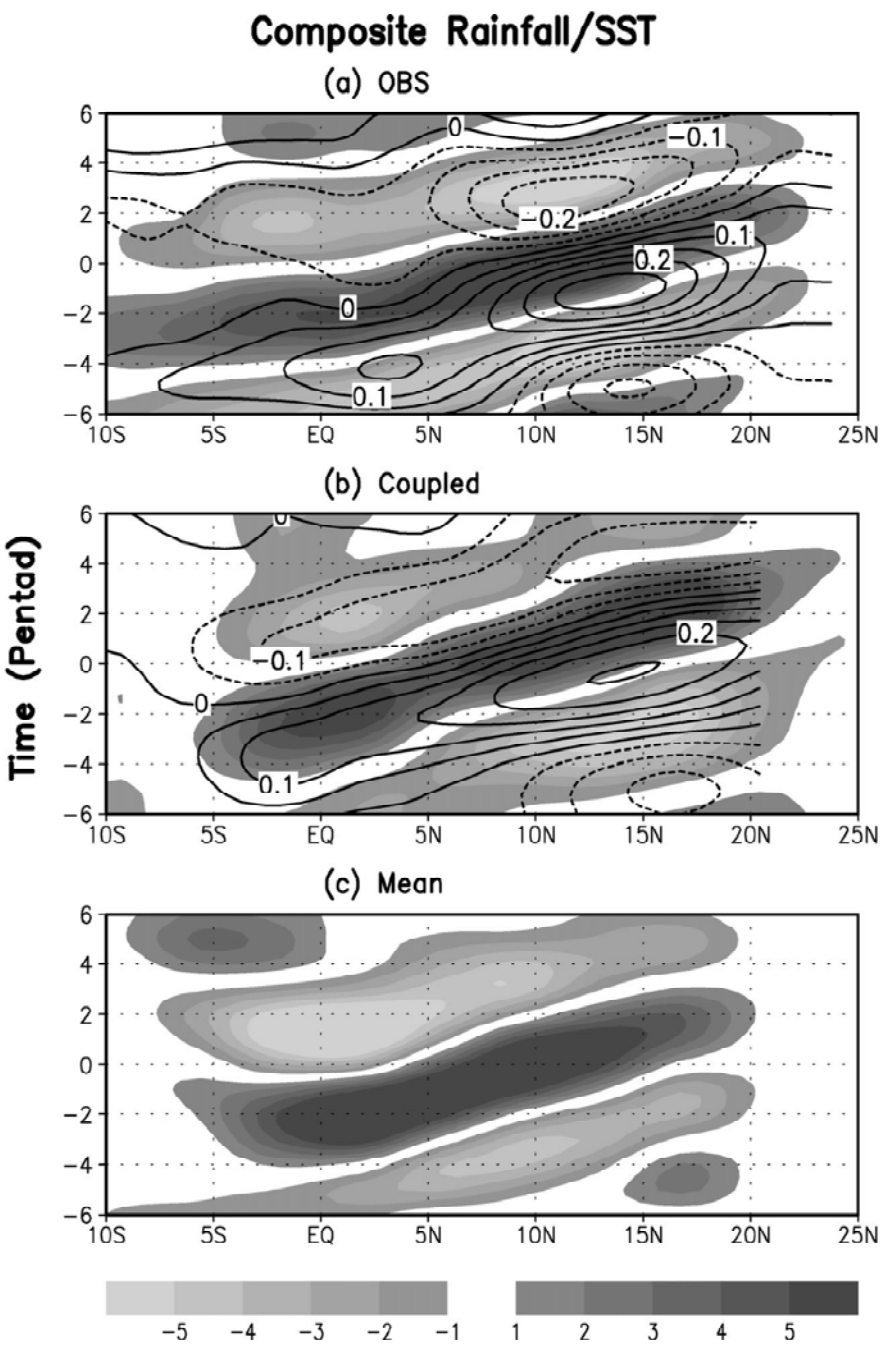

FIG. 11. Composite rainfall (mm day^{-1}; shaded) and SST (contours; contour interval: 0.05°C) associated with the NPISOs averaged between 85° and 95°E in (a) the observations (15 events), (b) the coupled run (16 events), and (c) the mean run (5 events).

SST-Rainfall relationship in MISO:

Evidence of air-sea interactions

Fu and Wang, 2003, J.Climate

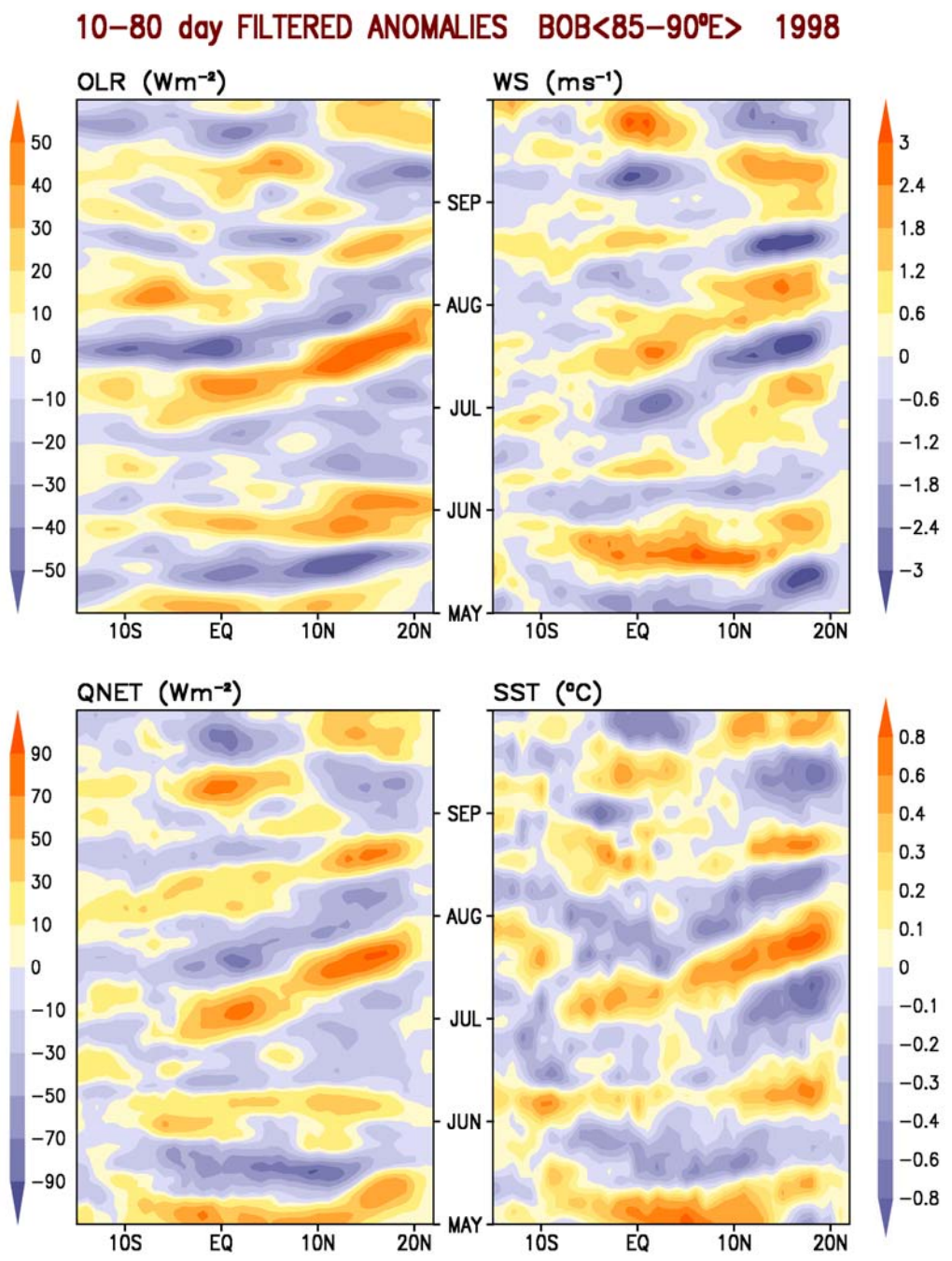

Monsoon ISOs are associated with Ocean-Atmosphere coupling

Coherent northward propagation of OLR, surface wind speed (WS), Qnet and SST during summer of 1998

Large amplitude of the ISO anomalies is noteworthy

Sengupta, Goswami & Senan . 2001, GRL

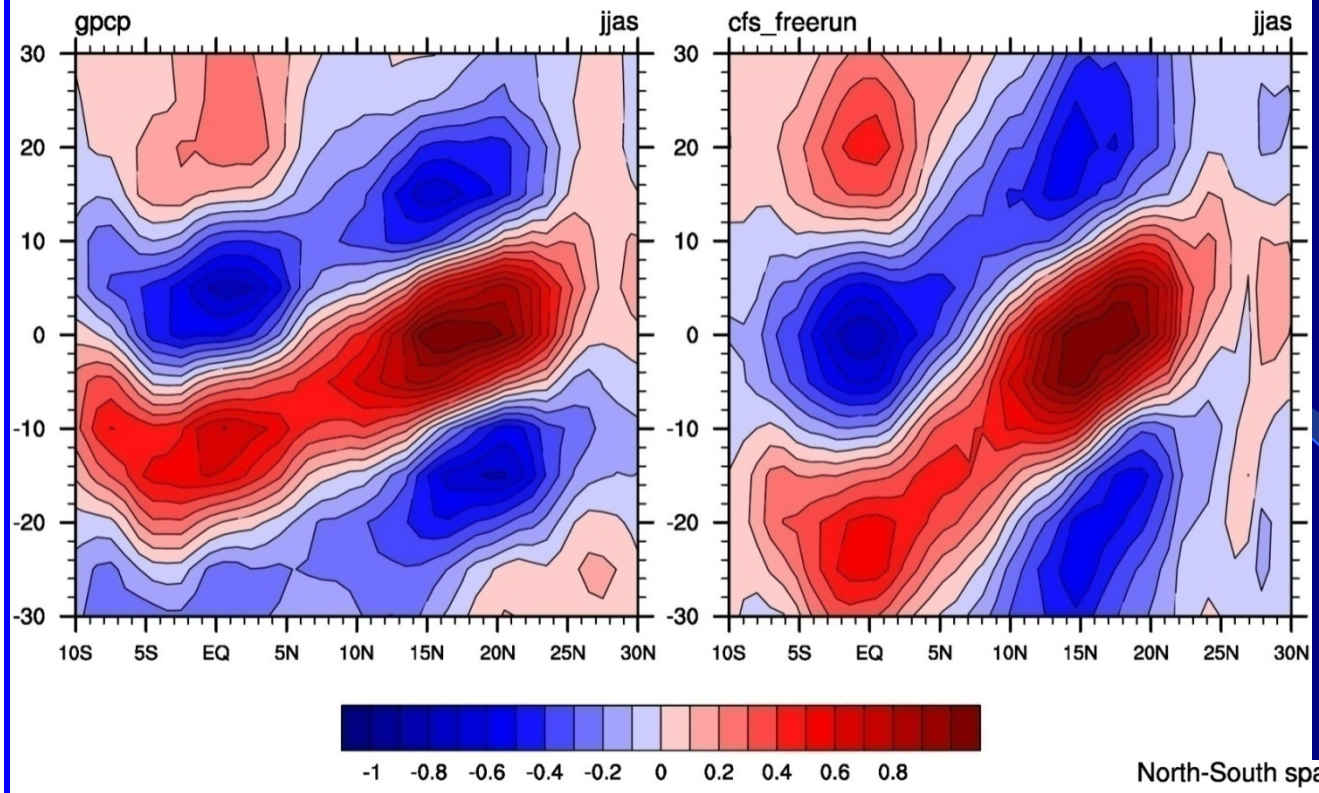

Lead lag correlation plot: OLR

Ref.series: 70-90E,12N-22N

CFSv2 with T126 atmos.

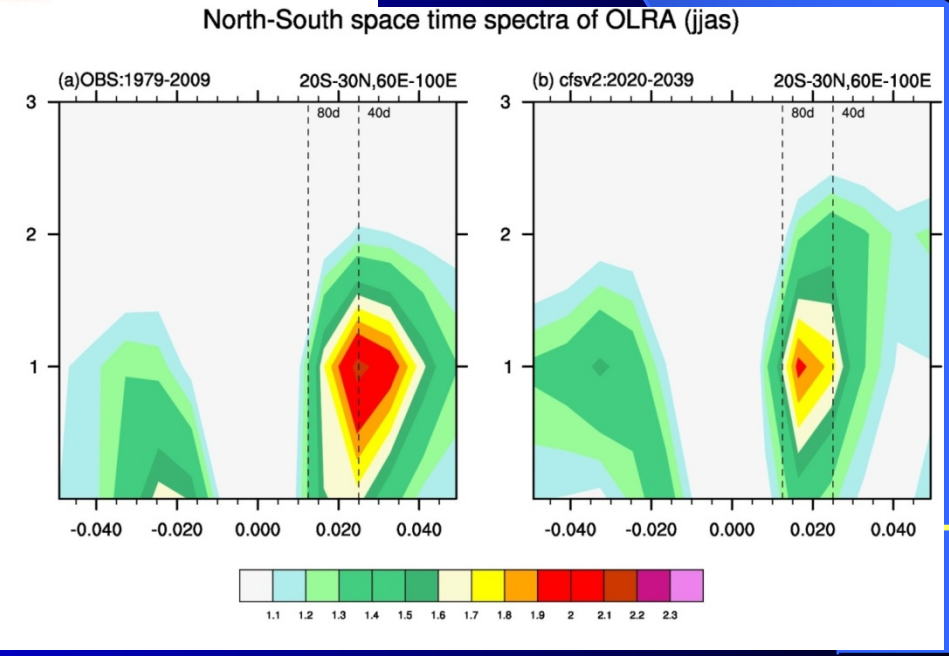

Northward Propagation of MISO

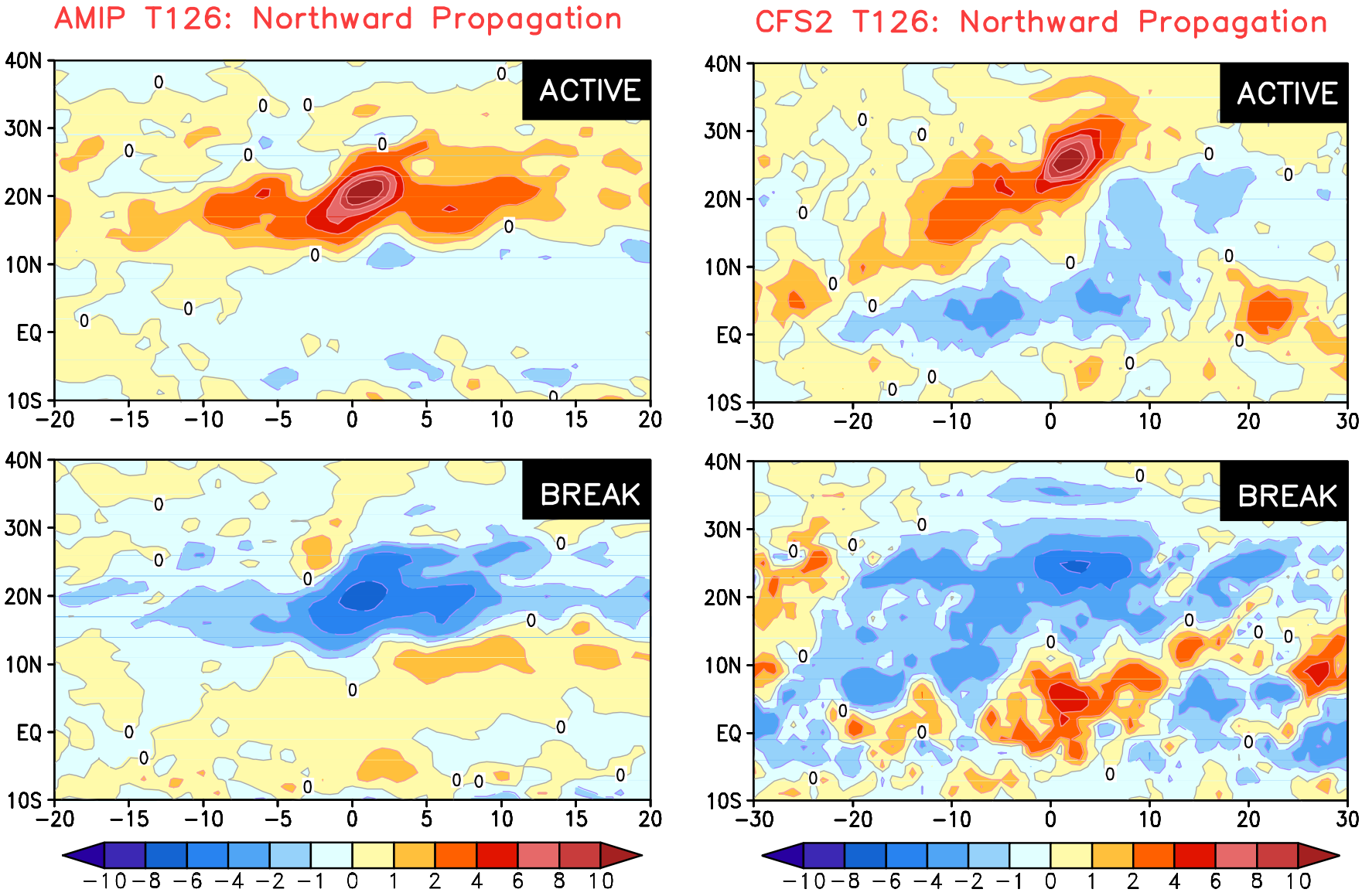

ISO variance in T382 CFS V2

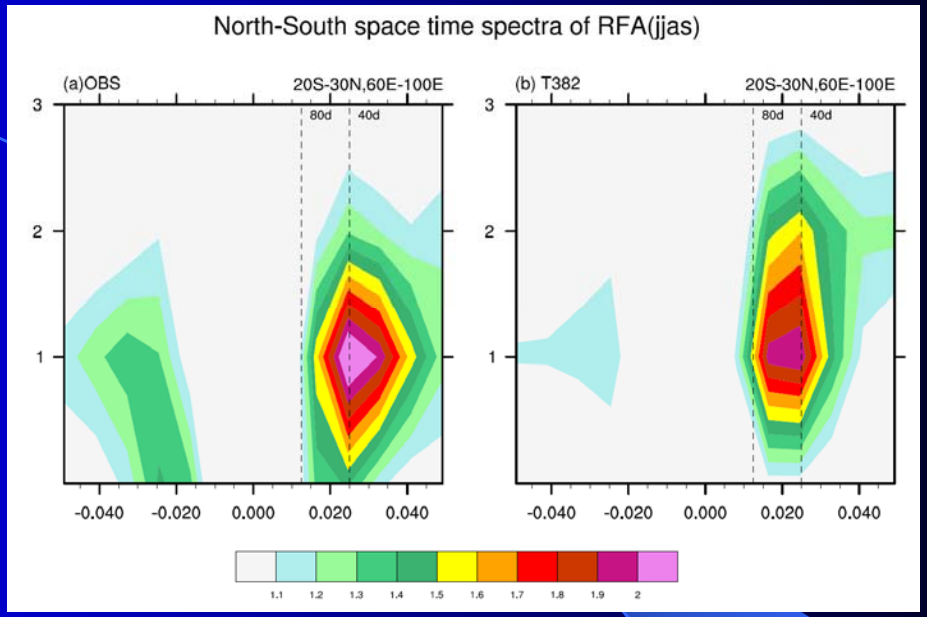

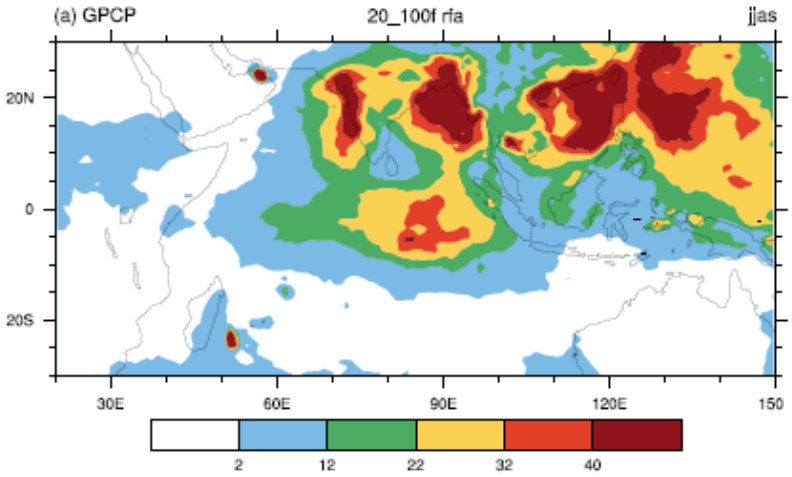

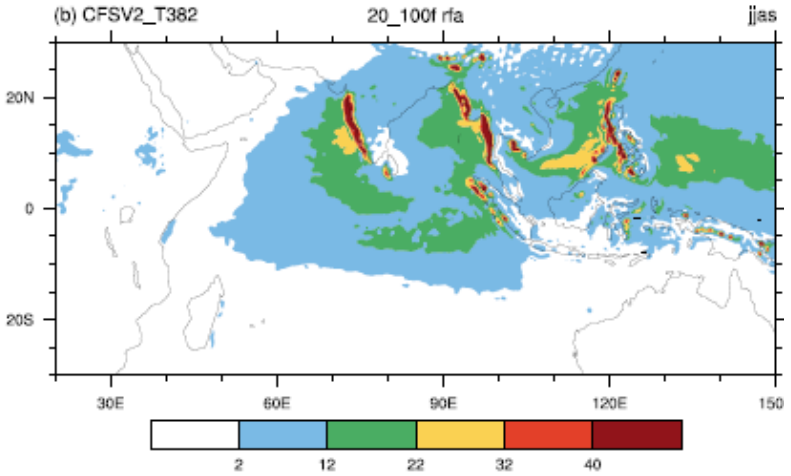

Northward propagation in T382 CFSv2

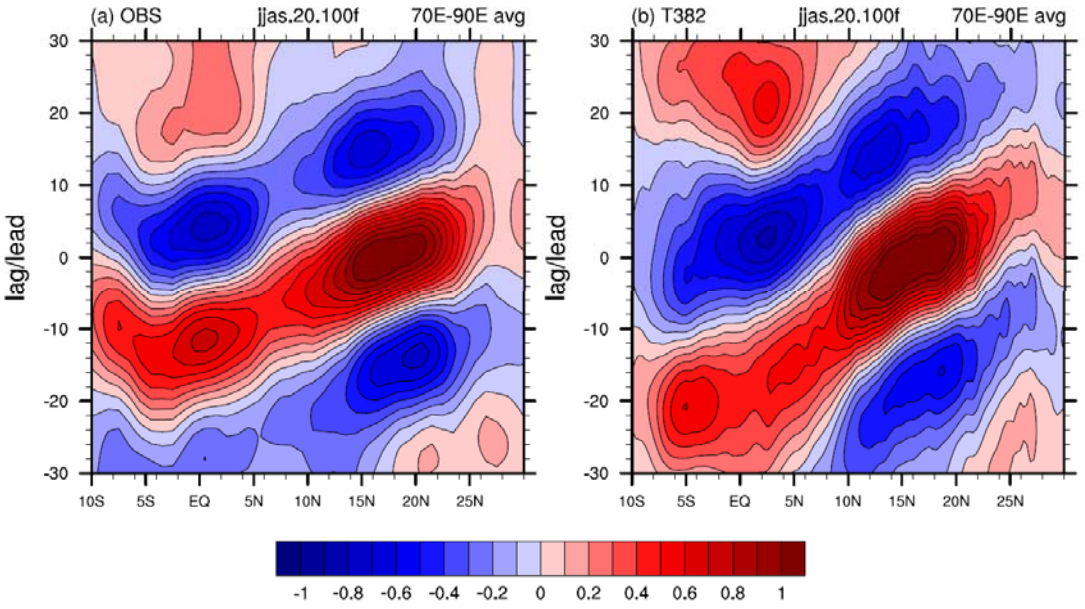

Climatology of Precipitation and SST (June-Sept)

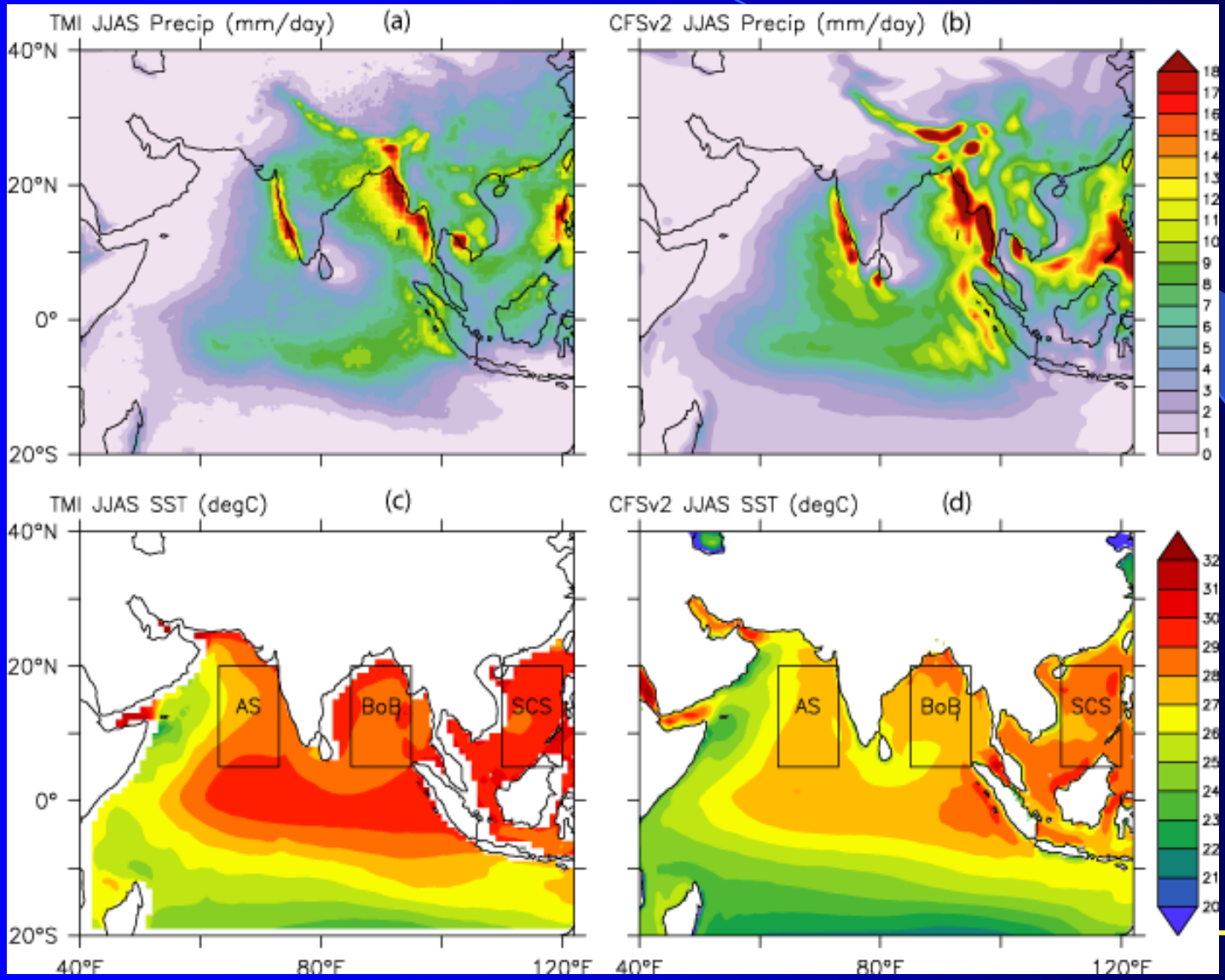

Courtesy:
Roxy Mathews

Spatial variability of SST – Precipitation relationship

The SST–precipitation relationship have different lead–lags over the Arabian Sea and the Bay of Bengal/South China Sea

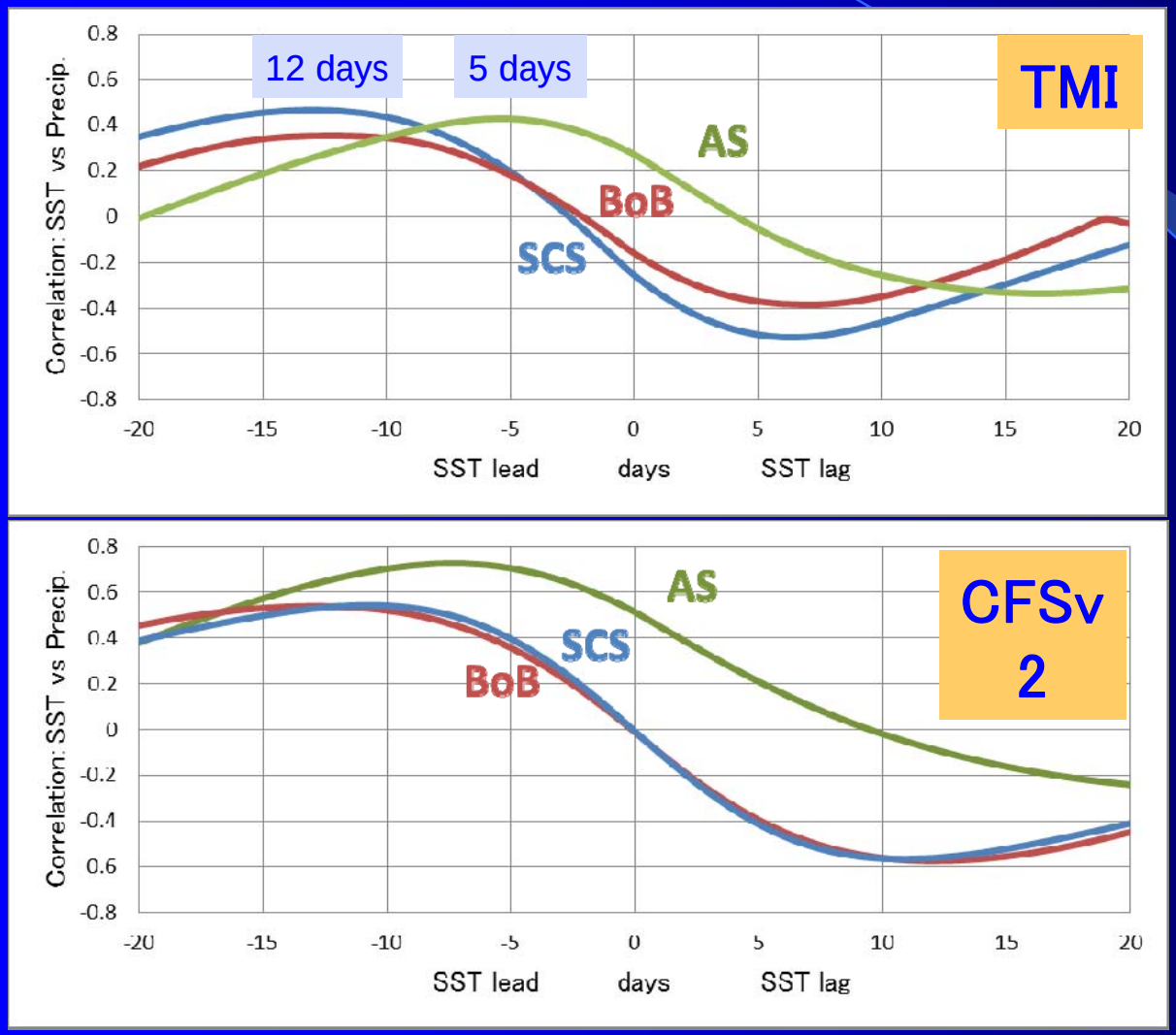

Spatial variability: response time difference of 1 week!

Spatial variability is there, but lessened.

More important, correlation between SST & precip. is overestimated:

TMI r_{max} = 0.4

CFSv2 r_{max} = 0.7

Ocean -> Atmosphere | Atmosphere -> Ocean

Can the MISOs influence the seasonal mean monsoon?

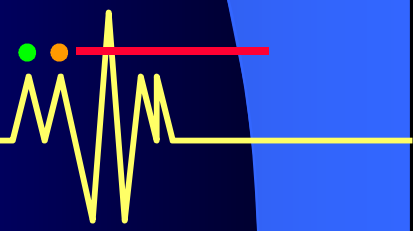

Climatological mean JJAS P and 850 hPa winds

P and 850 hPa wind anoms during 'Active' phase

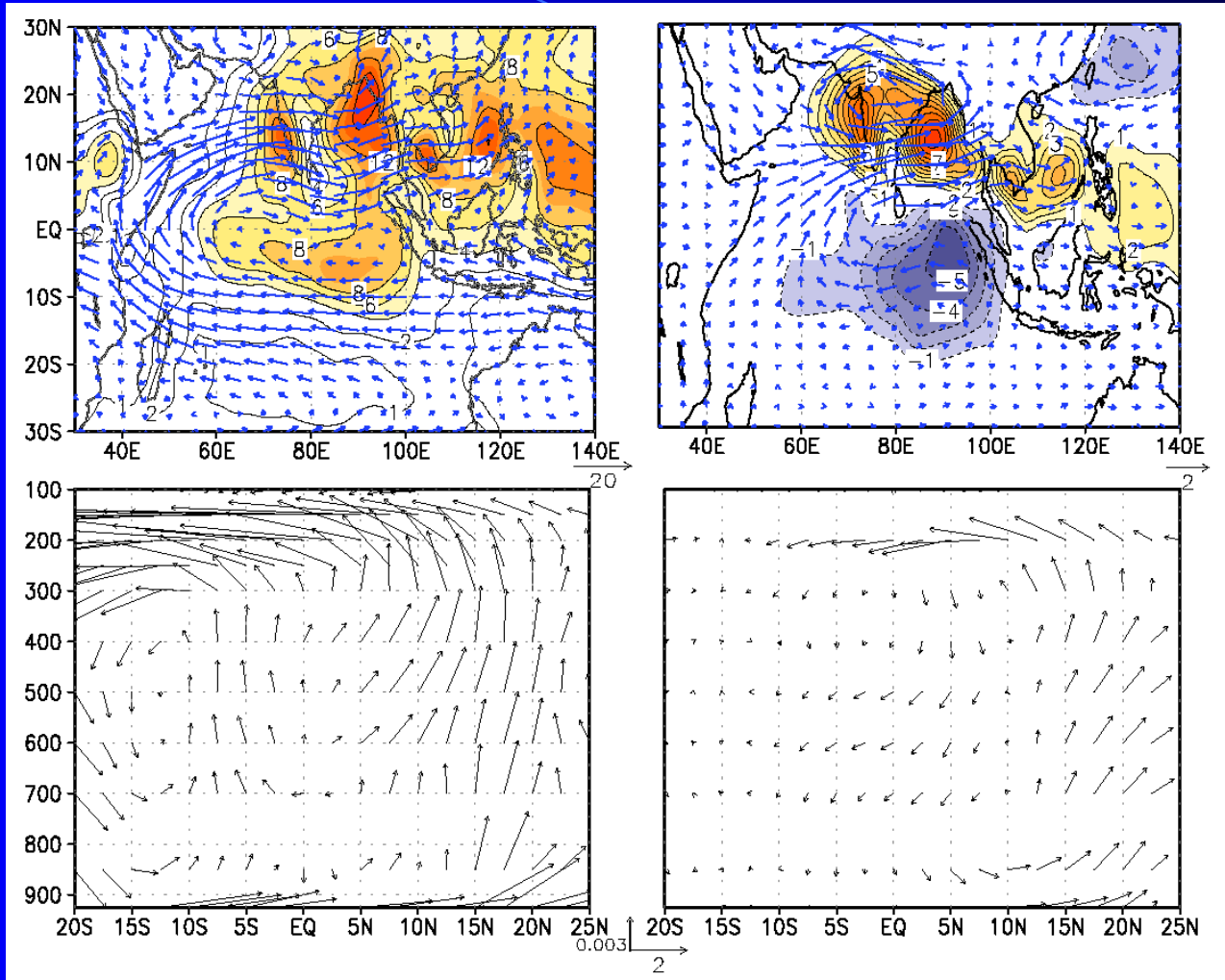

Mean monsoon Hadley circul.

70E-90E

Anom. Hadley circul. In an 'active' phase,

70E-90E

A common mode : Intraseasonal & interannual variability

Structure of dominant ISO mode

Active-Break composite of precipitation from NCEP

From 10-90 day filtered precip. Between 1 June-30 Sept., 1949-2002

Structure of dominant ISV mode

Strong-weak monsoon composite of precipitation from NCEP

From JJAS precip. Between 1949 and 2002, 6 strong and 4 weak monsoon years.

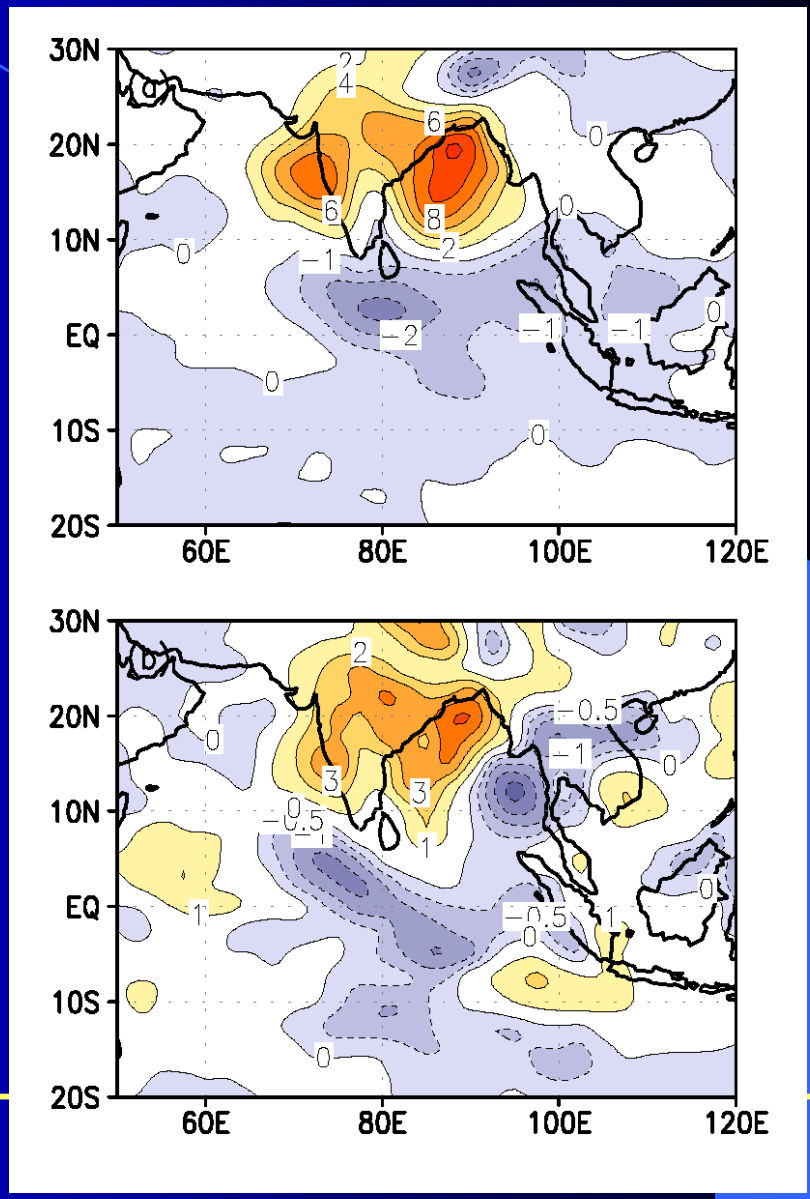

How does the ISOs influence the seasonal mean and IAV ?

- We have shown that the spatial structure of the summer ISOs have certain similarity with that of the summer seasonal mean. A common spatial mode of sub-seasonal and interannual variability.

- Seasonal mean of ISO anomaly can influence seasonal mean if frequency of occurrence of active and break phases are different.

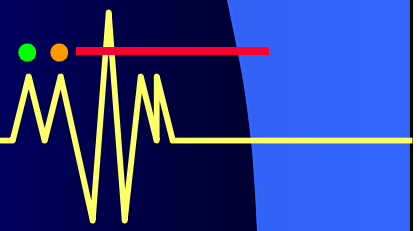

Frequency distribution of ISO anomalies of P over 70E-90E, 10N-30N

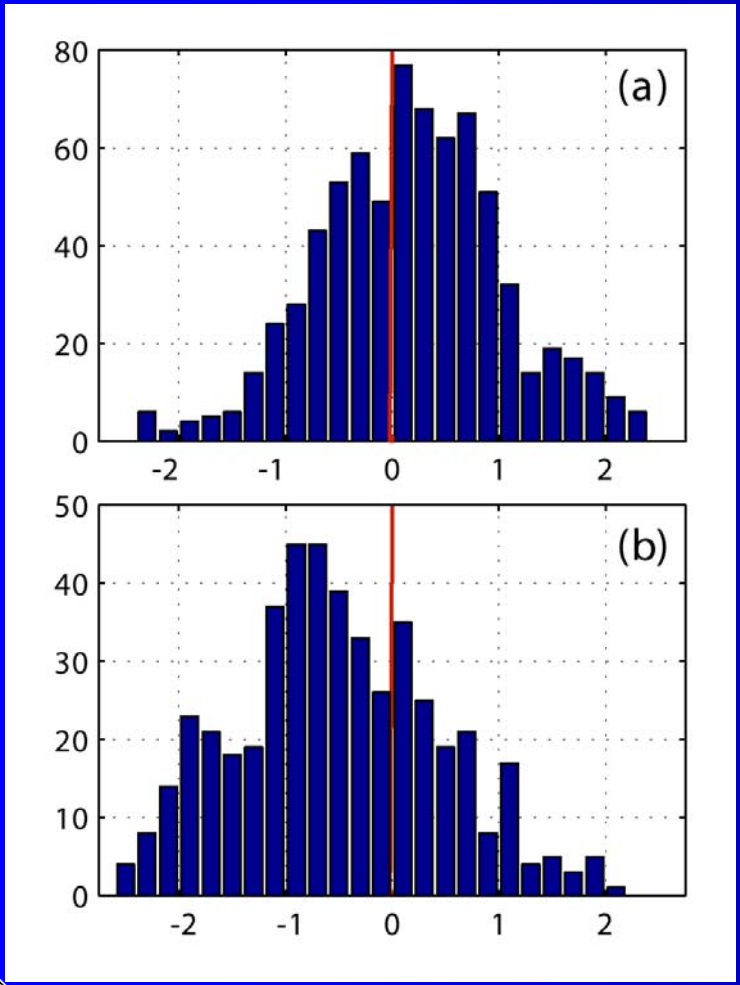

For 6 ‘strong’ Indian monsoon years

For 4 ‘weak’ Indian monsoon years

Goswami ,Wu and Yasunari, 2006, J. Climate

Seasonal mean of ISO anom. Vs interannual anomaly of seasonal mean

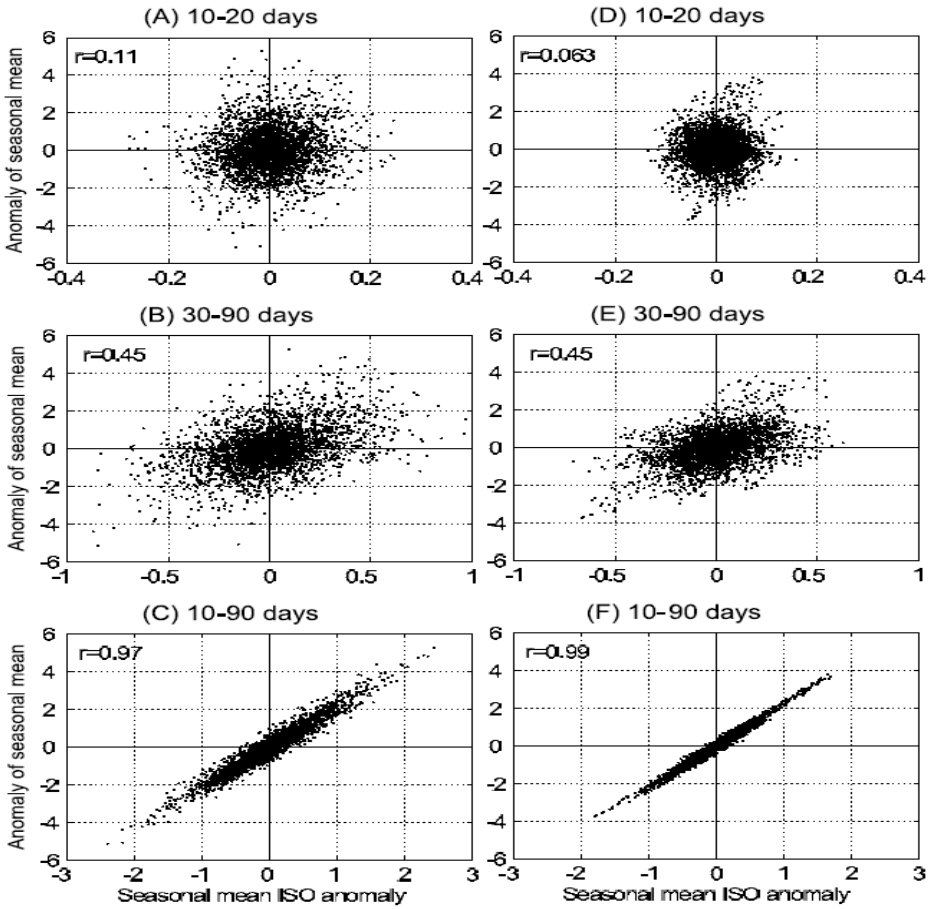

Figure 13. Scatter plot of interannual anomalies of seasonal mean versus seasonal mean of intraseasonal anomalies of precipitation (mm day^{-1}) from (a) 10–20 days band, (b) from 30–90 days band and (c) from 10–90 days band at all grid points in the domain 70°–100°E, 10°–30°N. (d, e, f) Similar to Figures 13a, 13b, and 13c, but for U850. Correlation values are given in the respective panels.

Goswami and Xavier, 2005, JGR

Predictability of Monsoon ISOs

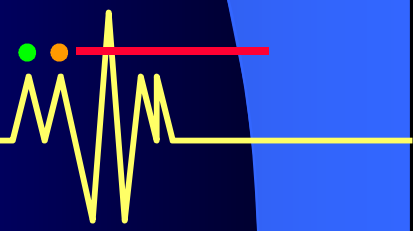

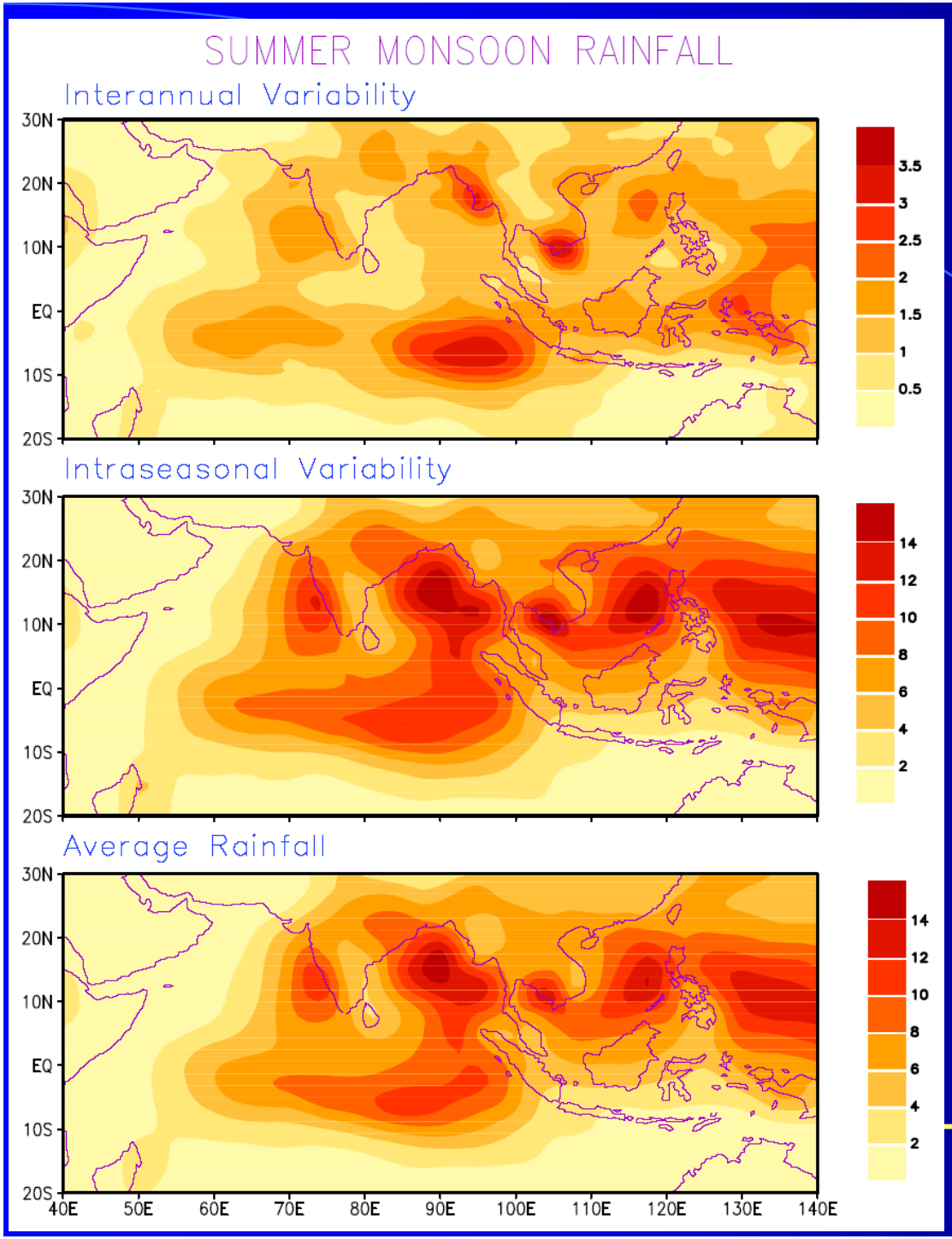

The ISO signal is much larger than signal in IAV of monsoon

Amplitude of (s.d.) of interannual variability of JJAS precipitation (mm/day) , (middle) Amplitude of intraseasonal variability (s.d. Of 10-90 day filtered anomalies during June 1 – Sept. 30) and (bottom) climatological mean JJAS precipitation (mm/day).

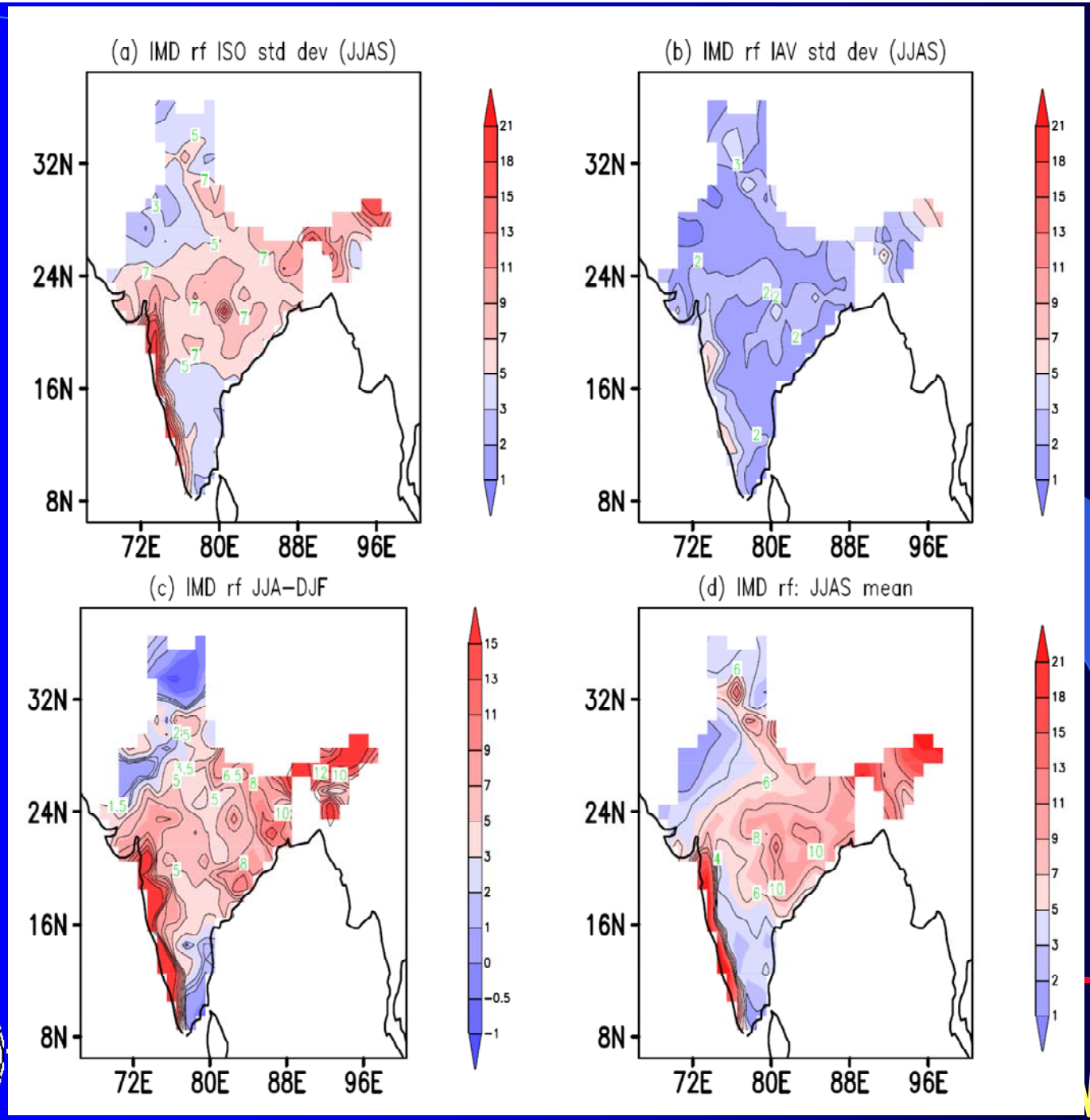
(a) IMD rf ISO std dev (JJAS)
(b) IMD rf IAV std dev (JJAS)
(c) IMD rf JJA−DJF
(d) IMD rf: JJAS mean
32N
24N
16N
8N
72E
80E
88E
96E

How Predictable are the Monsoon ISOs?

- **A simple procedure is described to make such an estimate of potential predictability for active and break conditions from observations**

Goswami and Xavier, 2003, GRL

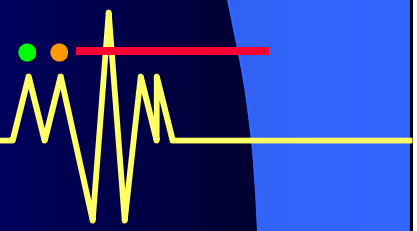

Data Used

- Daily rainfall over Indian continent from rain gauge stations (1951-2000)
- CMAP pentad data (linearly interpolated to daily values) , 1979-2001
- NCEP/NCAR Reanalysis daily winds ; 1979 – 2001
- NOAA daily OLR ; 1979-2001

10-90 day band-pass Lanczos filter is used to isolate ISO

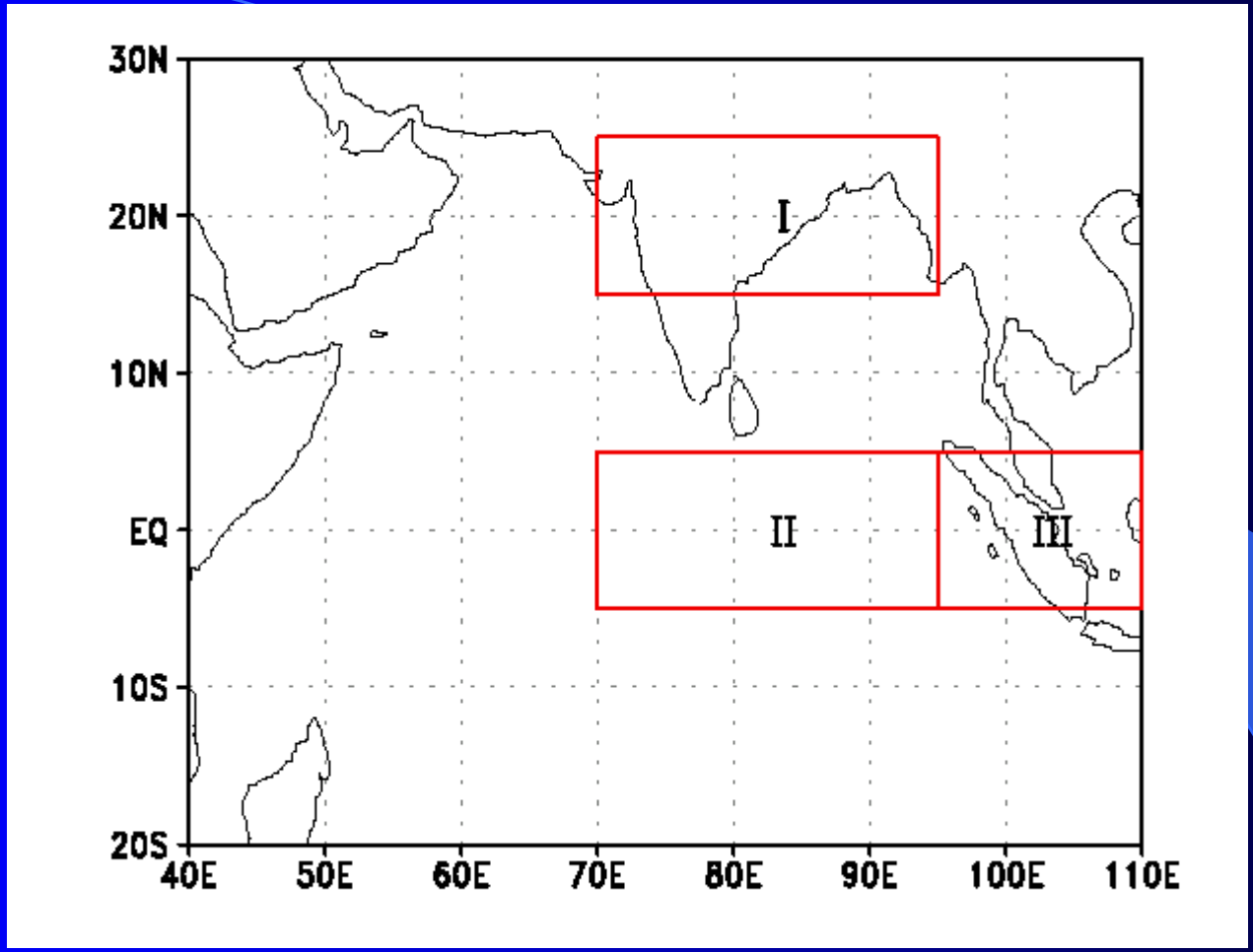

Regions over which potential predictability of precipitation is examined

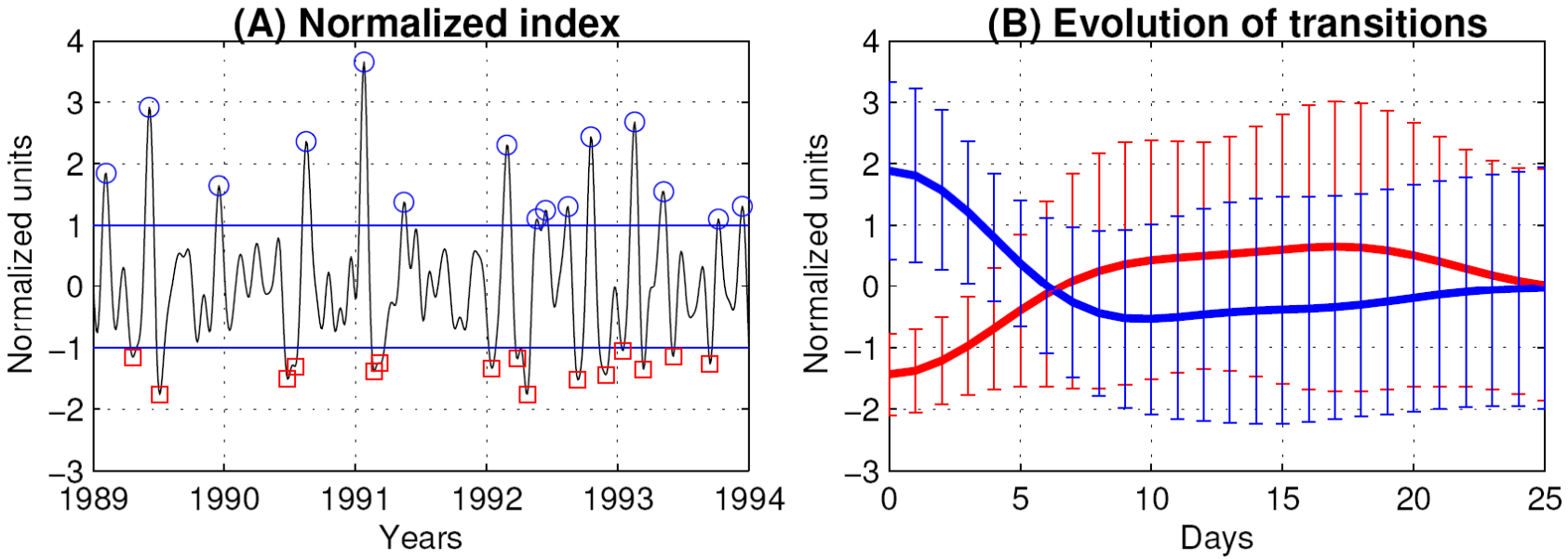

FIGURE 6.2: (A) An index of the monsoon intraseasonal variability defined as the time series of rainfall anomalies averaged over, 70°-90°E, 15°-25°N and normalized with its own standard deviation. The index is shown for a typical period of 4 years. Active phases are marked with red circles and break phases are marked with blue squares. (B) shows the evolution from active to break (in blue) and from break to active (in red). Average transitions are plotted in thick lines and the spread in transitions in terms of standard deviation of different evolutions at each lag are plotted as error bars with corresponding colors.

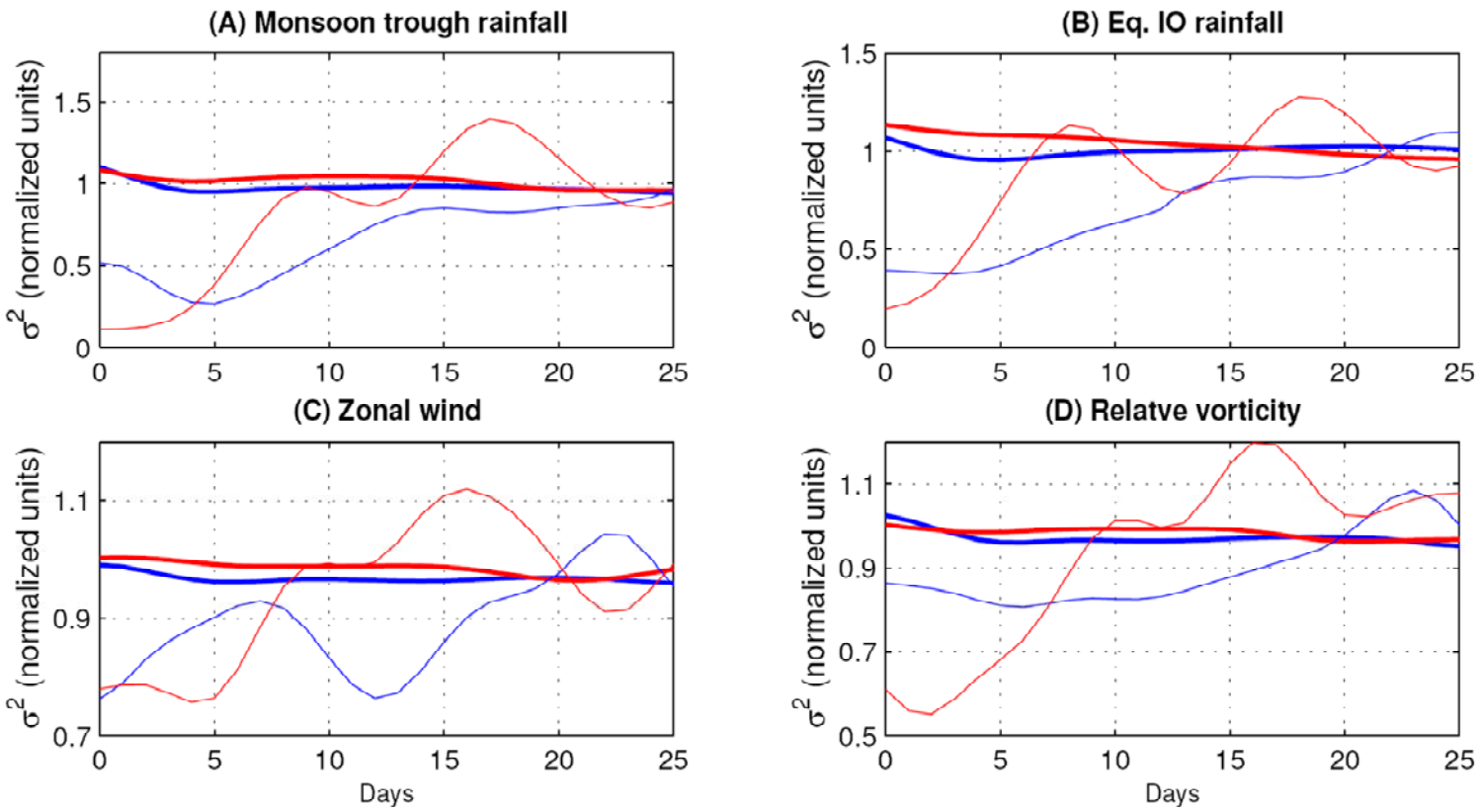

FIGURE 6.3: (A) The thick red (blue) line is the monsoon ISO 'signal' starting from troughs (peaks) of the index (Fig.6.2A). The thin red (blue) line is the standard deviation (or spread) of ensemble members as a function days from the initial date corresponding to all troughs (peaks) of the index representing transitions from break to active (active to break). (B) is same as (A) but for a precipitation index averaged over the eastern equatorial Indian Ocean (80°-100°E, 5°S-5°N). (C) same as (A) but for evolution of zonal wind at 850 hPa averaged over 80°-95°E, 12°-18°N. (D) same as (A) but for relative vorticity at 850 hPa averaged over the monsoon trough.

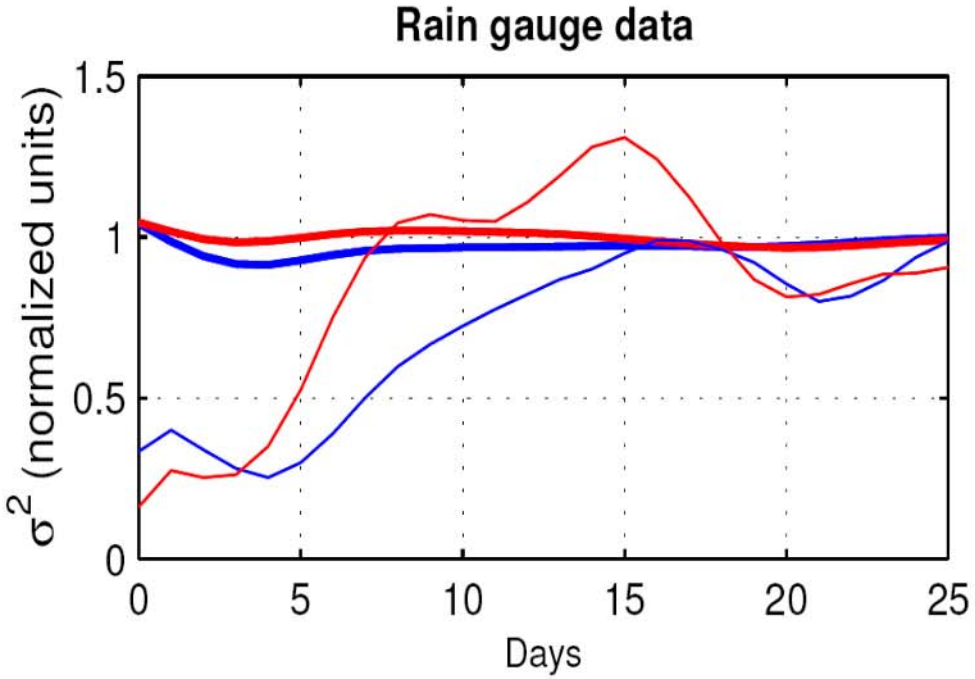

FIGURE 6.4: Same as Fig.6.3A, but for high resolution gridded daily rain gauge data (Rajeevan et al., 2006) for the JJAS season of 1951-2003, averaged over 70°-90°E, 18°-30°N.

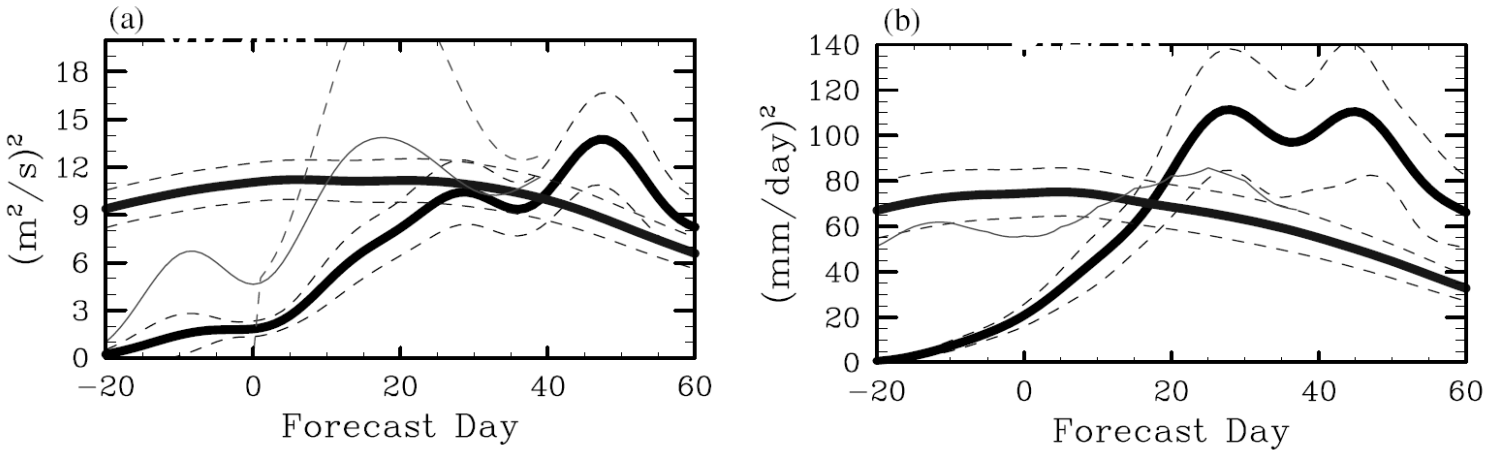

Figure 8. (a) Mean-squared forecast error (Eq. (4)) for the (30–90 day) filtered 200 hPa velocity potential (VP200) over the region 12–16°N and 117.5–122.5°E (model grid point at centre of smaller box in Figs. 10 and 11) for all the selected intraseasonal oscillation (ISO) cases ($N = 168$), shown by the thick solid black line that increases with forecast time; the mean ISO signal (Eq. (3)) is also shown, by the thick solid black line that is roughly constant with forecast time; 95% confidence limits for these two quantities using a Students t-test are given by the thin dotted lines; additionally the mean-squared forecast errors for two different types of persistence forecasts (see section 4 for more details) are given by the thin grey line. (b) As (a) but for rainfall, except that the thin grey line in this case gives the mean-squared forecast errors for an empirical forecast method based on the canonical ISO pattern depicted in Fig. 2 (see section 4 for more details). VP200 values have been scaled by 10^{-12}.

Waliser et al. 2003, QJRMS. **129**, 2897-2925

Uses GLA GCM, carried out 'identical twin' predictability experiments 84 cases selected from the amplitude of EEOF of 30-90 day filtered fields.

Conclusion: ISO Predictability

The transition from break to active conditions is intrinsically more chaotic than transitions from active to break conditions.

A fundamental property of monsoon ISOs.

Why?

Break →Active – convective instability— growth of error governed by fast conv. Instability

Active→Break – dying convection -- slow error growth due to slow oscillation

Consequence,

The potential predictability limit for monsoon breaks is about 20 days while that for monsoon active conditions is only about 10 days

Air-Sea Coupling Extends the Predictability of Monsoon Intraseasonal Oscillation

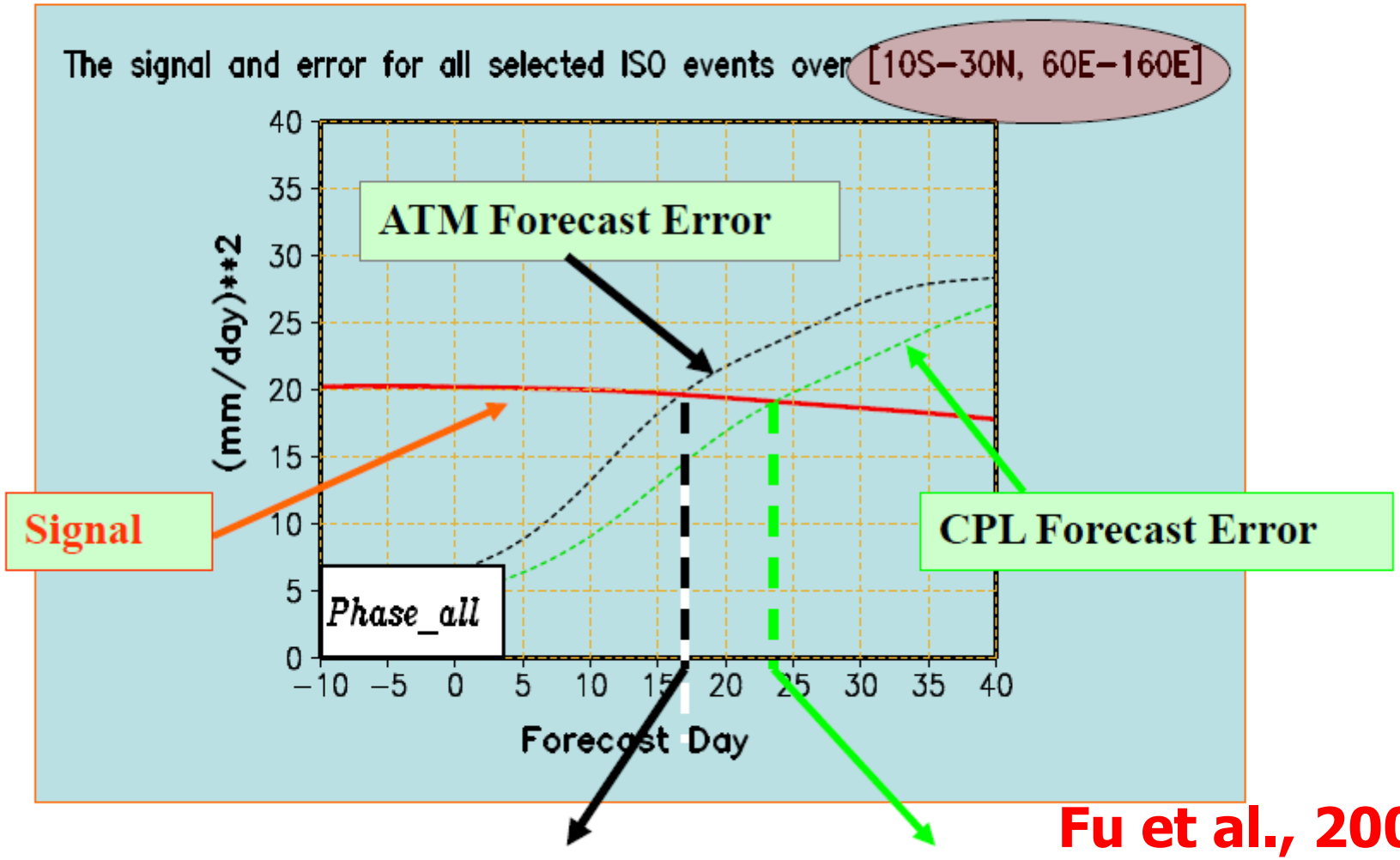

Fu et al., 2007

[ATM: 17 days; CPL: 24 days]

Extended Range Prediction of MISO

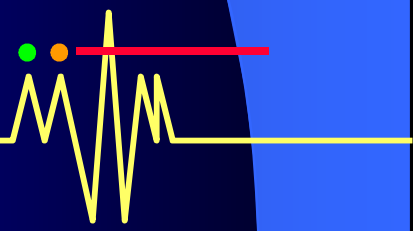

Empirical models:

Waliser et al. (1999), *J. Climate*, 12, 1918- 1939**.**

Lo and Hendon (2000), ***Mon. Wea. Rev.*****,** **128**, 2528–2543.

Mo (2001), *Mon. Wea. Rev*. 129, 802- 817**.**

Wheeler and Weickmann (2001), *Mon. Wea. Rev*. 129, 2677- 2694

Jones C et al (2004) ***J. Climate*** **, 17,** 2078- 2095

Use empirical technique and demonstrate skilful forecasts of the MJO in OLR and 200 hPa streamfunction up to 20 days in advance. The models perform well when the MJO is active at the initial condition but not so well when it is inactive.

All these studies primarily concentrated on MJO and use 25-90 day filtered data.

We feel that same may be possible for summer monsoon ISOs although existence of higher frequencies (10-20 day) may limit it to some extent.

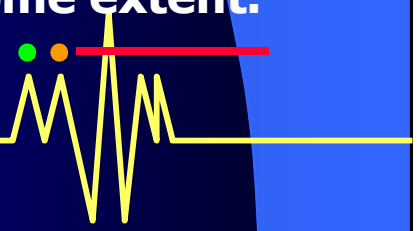

Webster and Hoyos (2004, BAMS) also show very good skill for predicting ISO phases using a slightly different empirical technique (wavelet banding)

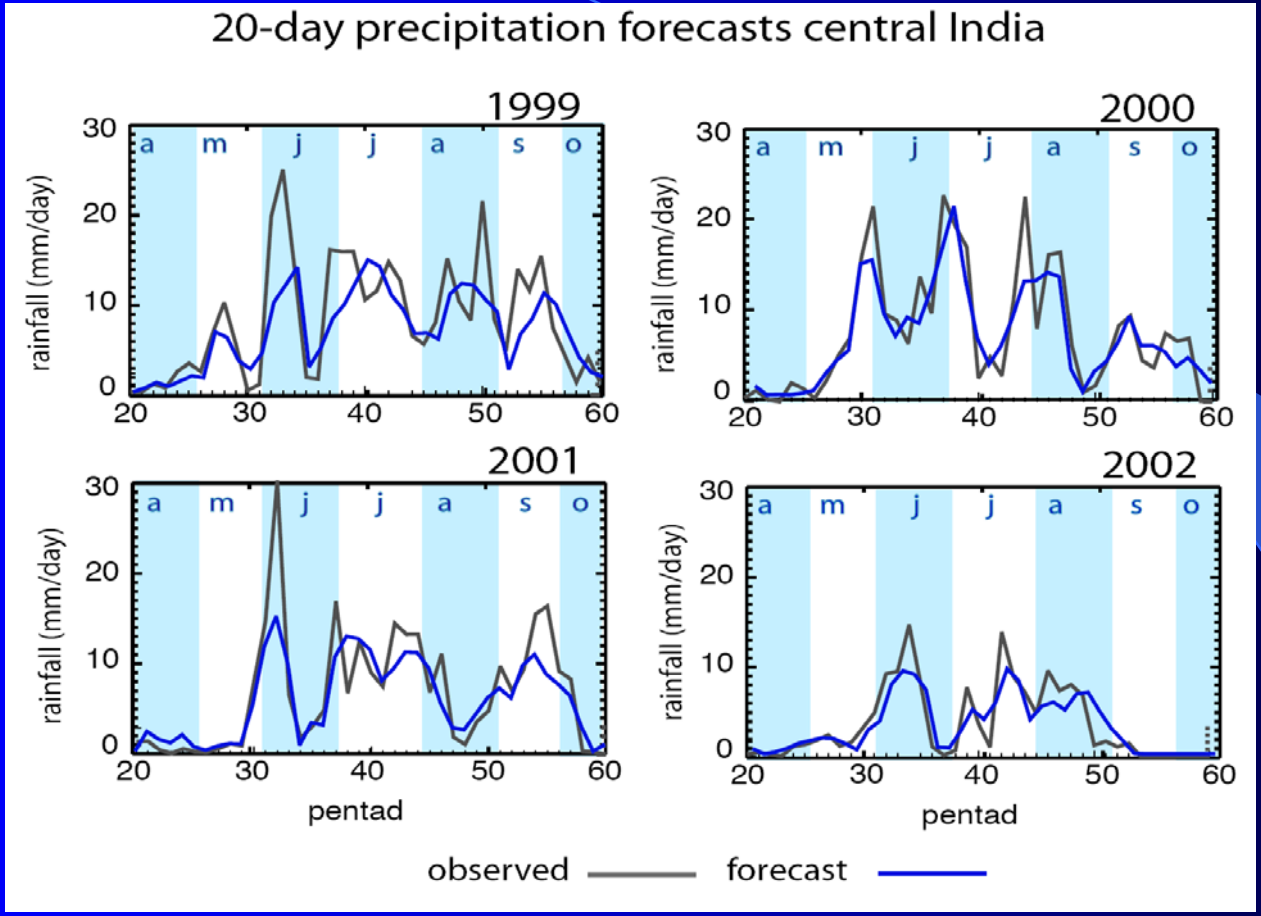

20-day forecast of precipitation over central India for the summers of 1999-2000. Blue lines indicate forecasts while the grey lines indicate verification obtained from area averaged GPI precipitation.

A new Analogue model for Extended Range prediction of the summer Monsoon ISOs useful for real time prediction

(Xavier and Goswami, 2007, MWR , 135, 4149-4160)

- Data Used and methodology:
- Penrad OLR data from 1979 to 2004 are used. No filtering is involved.
- To isolate the ISO, OLR anomalies are reconstructed with the first 10 EOFs
- First spatial analogues are identified and temporal analogue for each PC is found from the cases selected for spatial analogues.

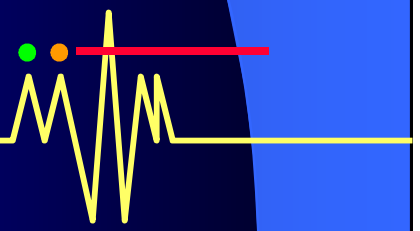

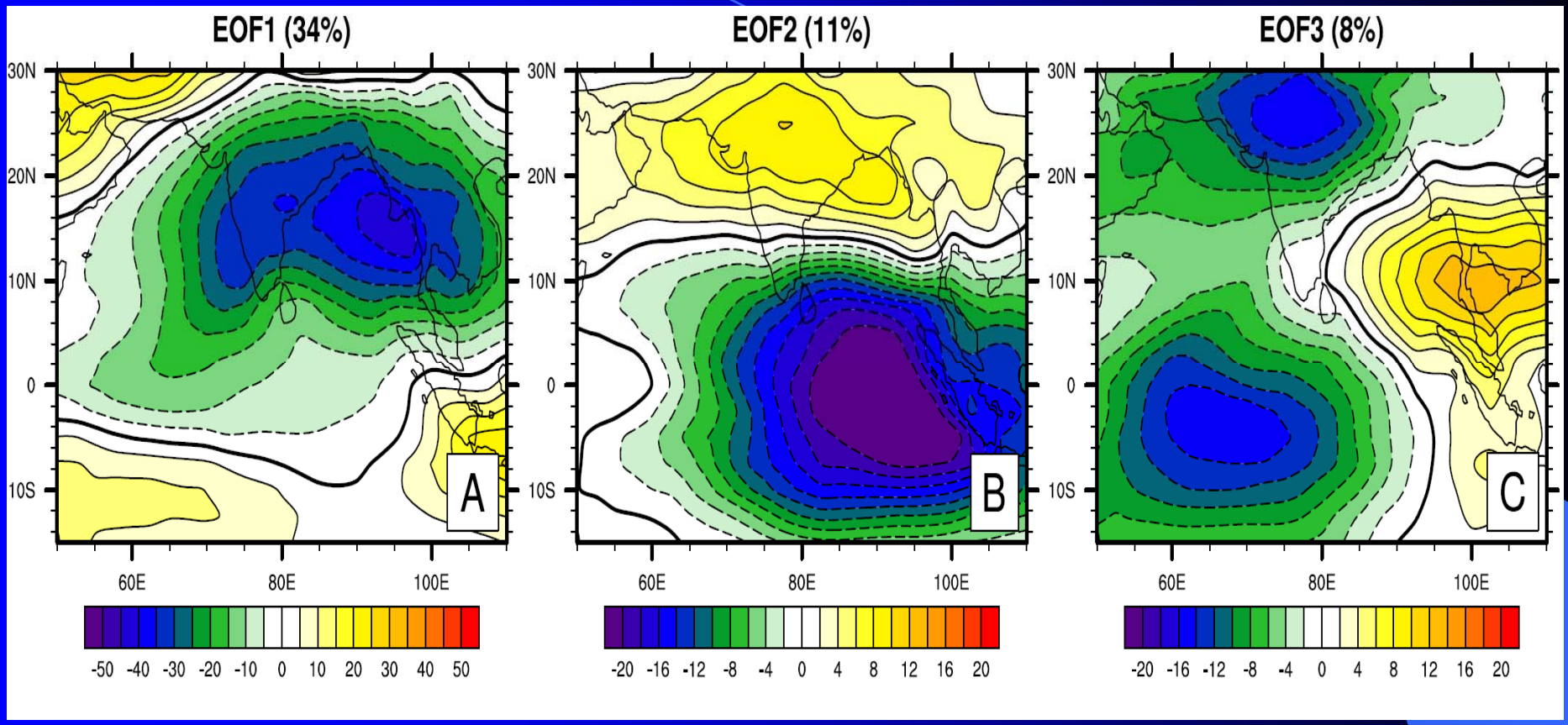

First three EOFs of pentad OLR

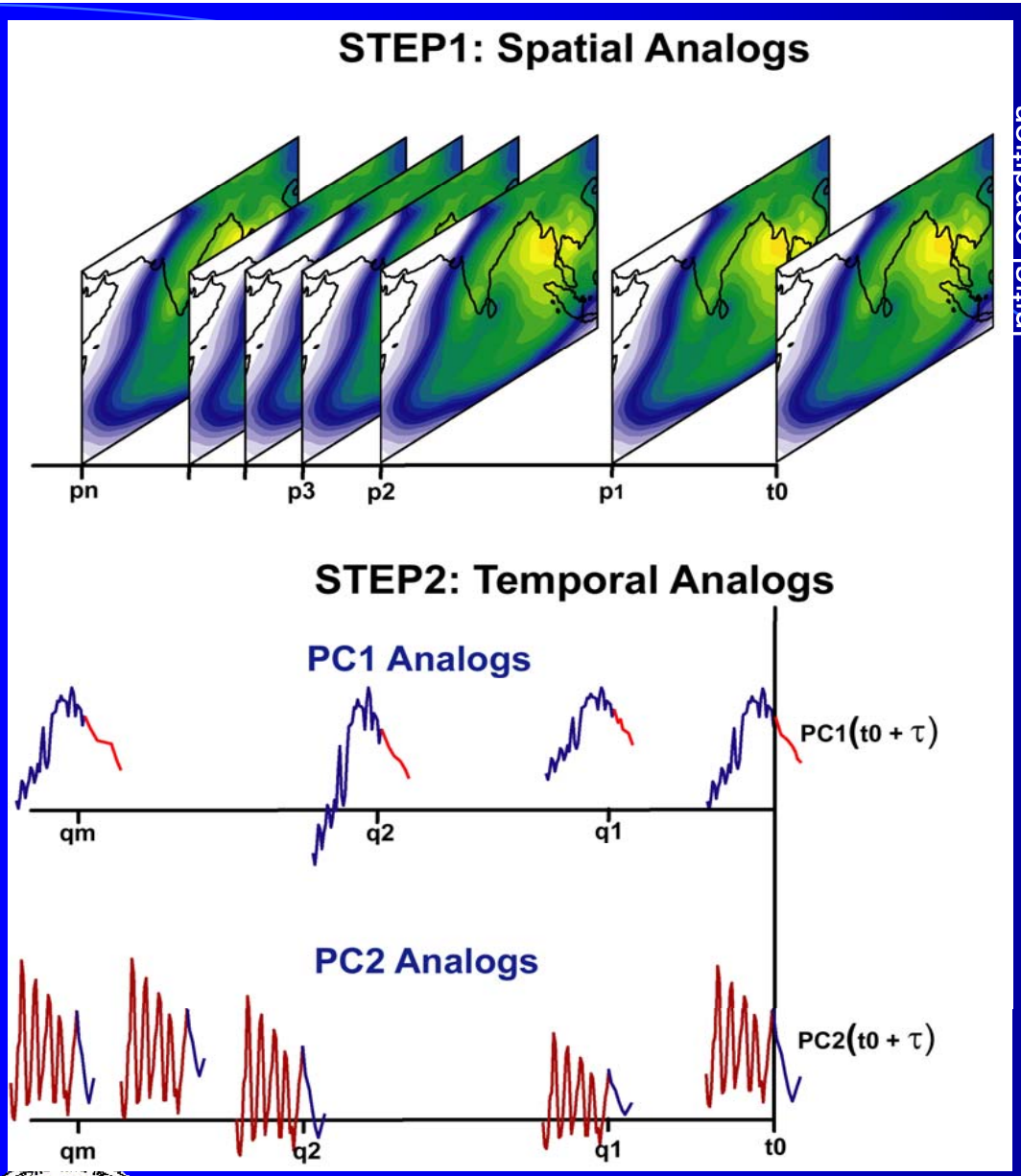

Initial condition

Identify spatial analogues over the entire period (25 years) for the OLR field reconstructed with first 10 EOFs at to

Identify temporal analogues for all 10 PCs going 5 pentads backward from each of the spatial analogues

Prediction → average evolution of the identified temporal analogues

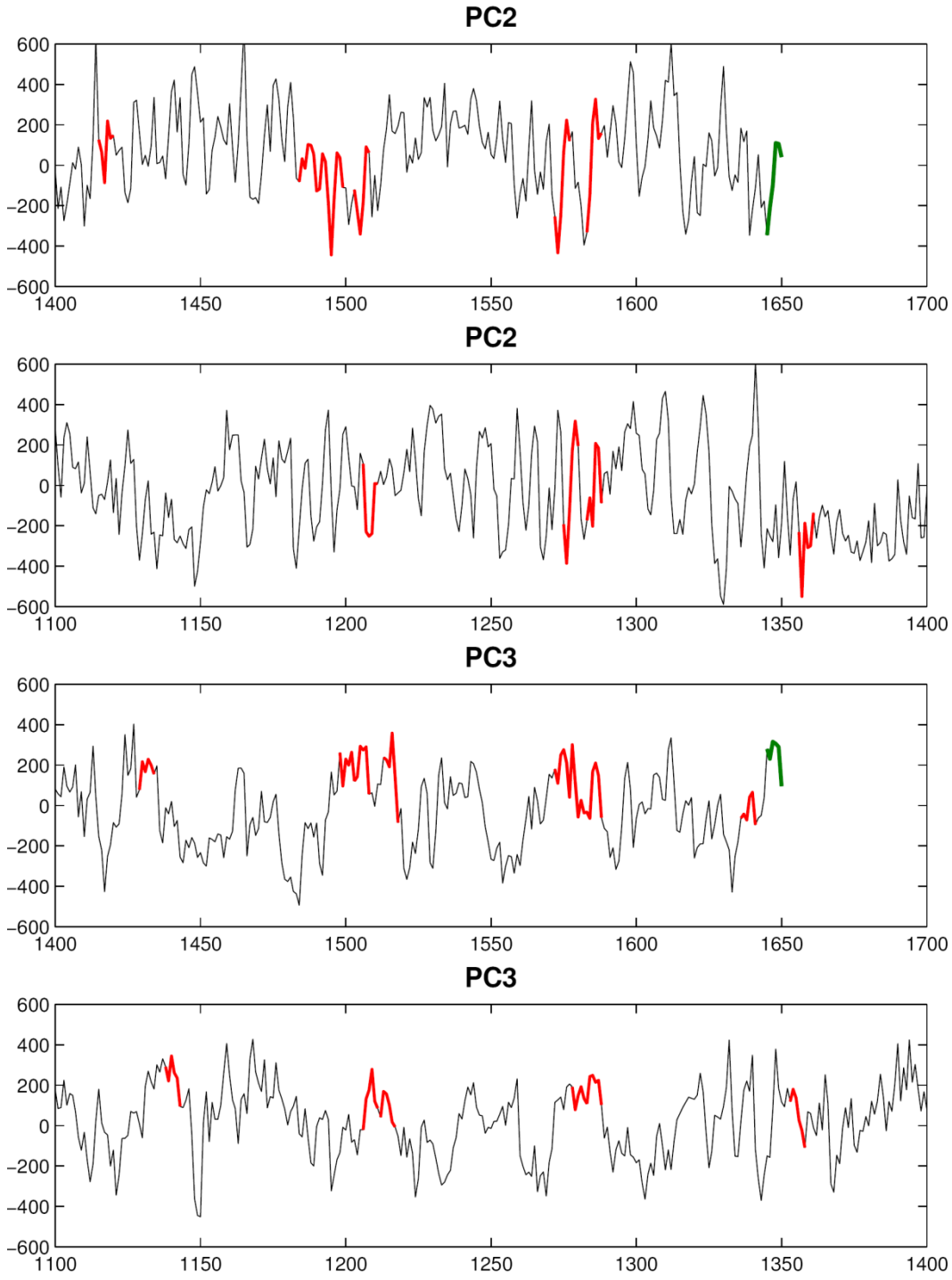

Illustration of a few temporal analogues of PC2 and PC3 for a particular initial condition.

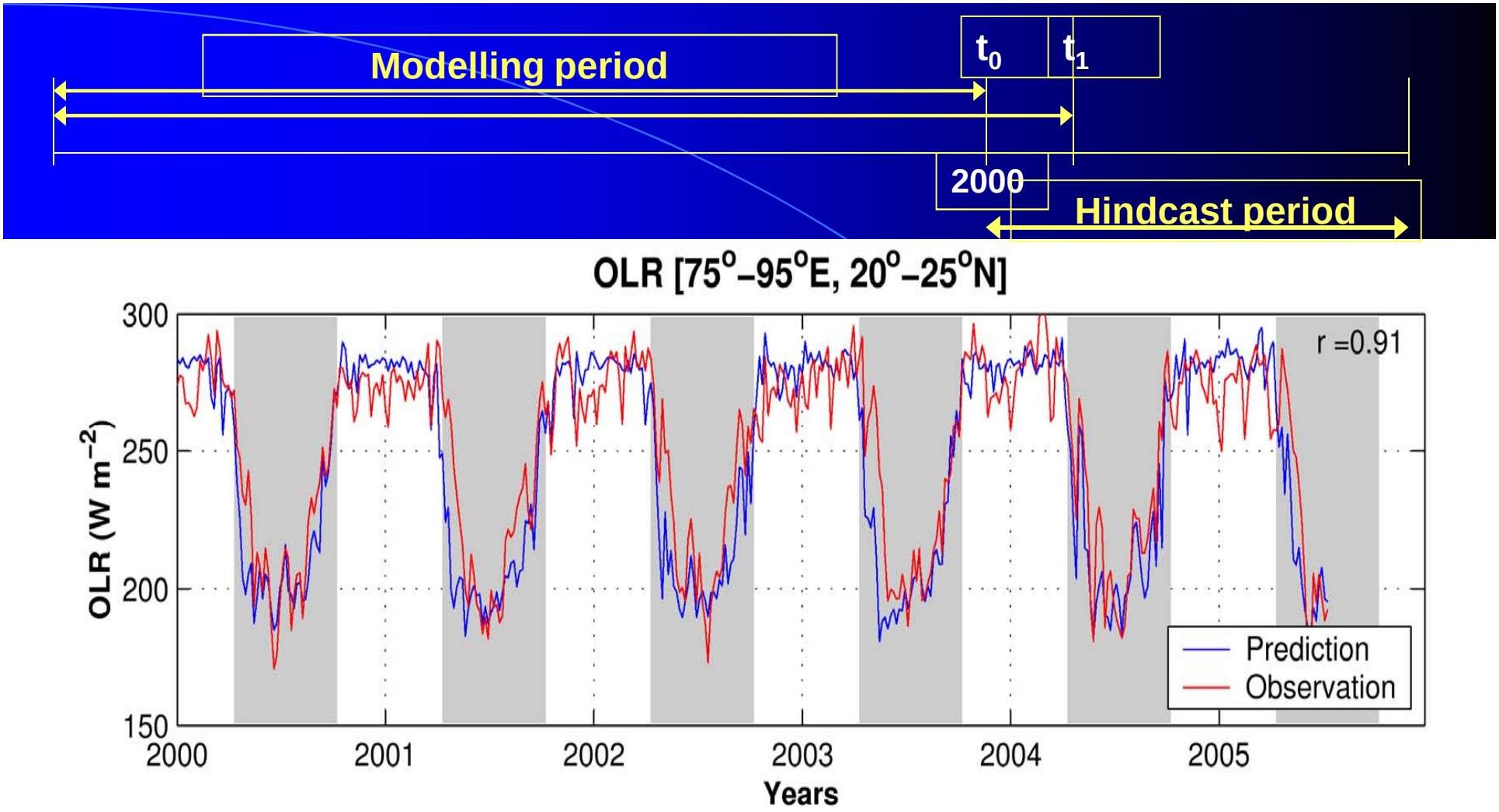

FIGURE 7.8: 4 pentads lead predictions and observations over central India during the hindcast period. Grey shades indicate the summer monsoon season. Correlation coefficient between the two is also shown.

Anomaly hindcasts

- Reconstruct the OLR data with 2-10 EOFs

  (removes the seasonal cycle)

- Look for spatial and temporal analogues as before

- Make predictions based on average evolution of these analogues

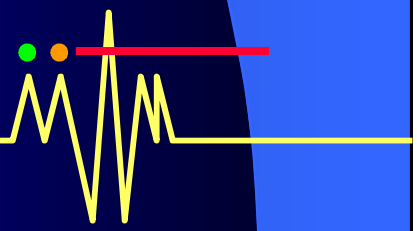

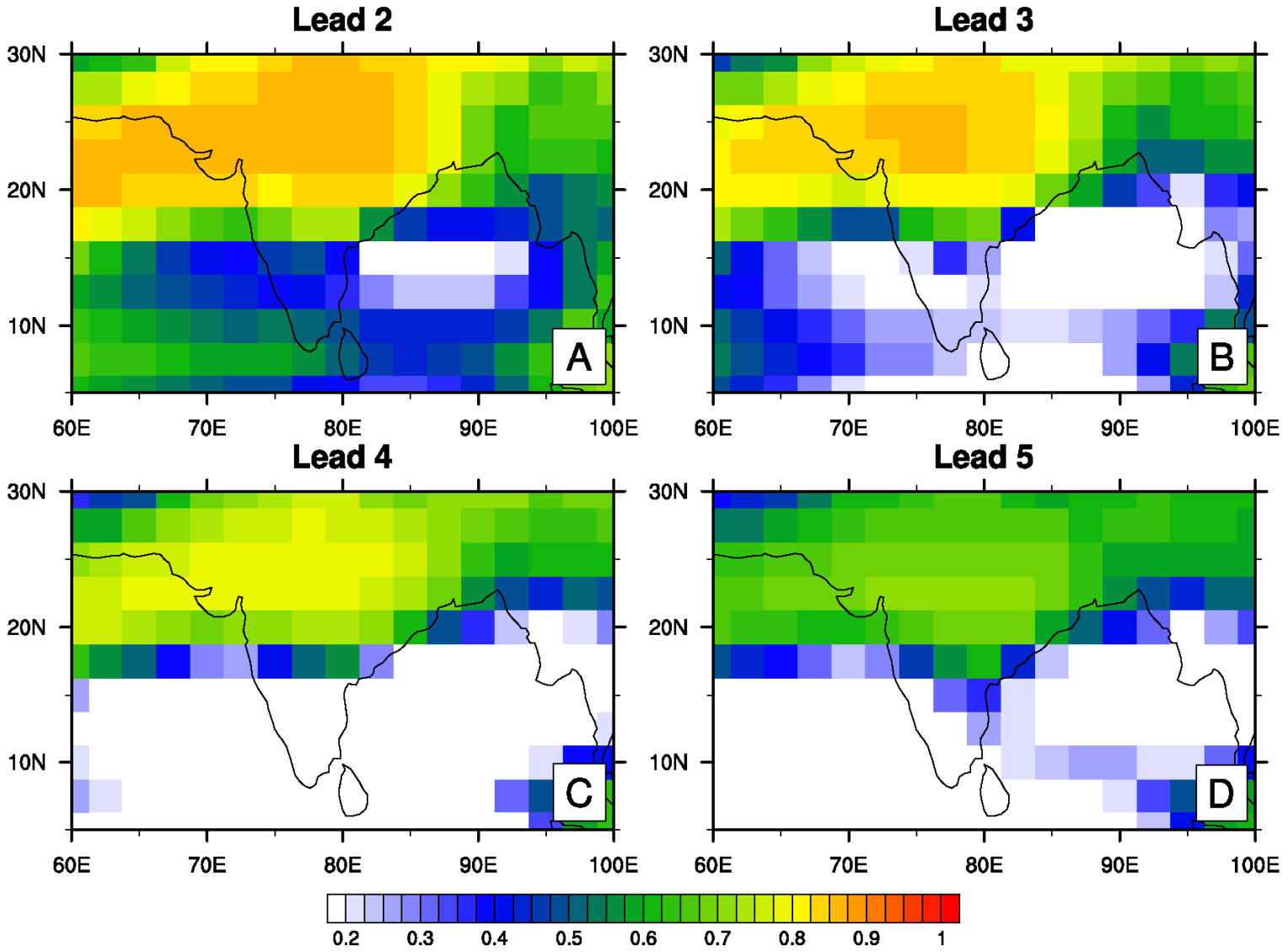

FIGURE 7.11: Temporal correlations between predictions and observations for different lead times during the May-October period in the AH.

Dependency of the forecasts on the state of initial condition

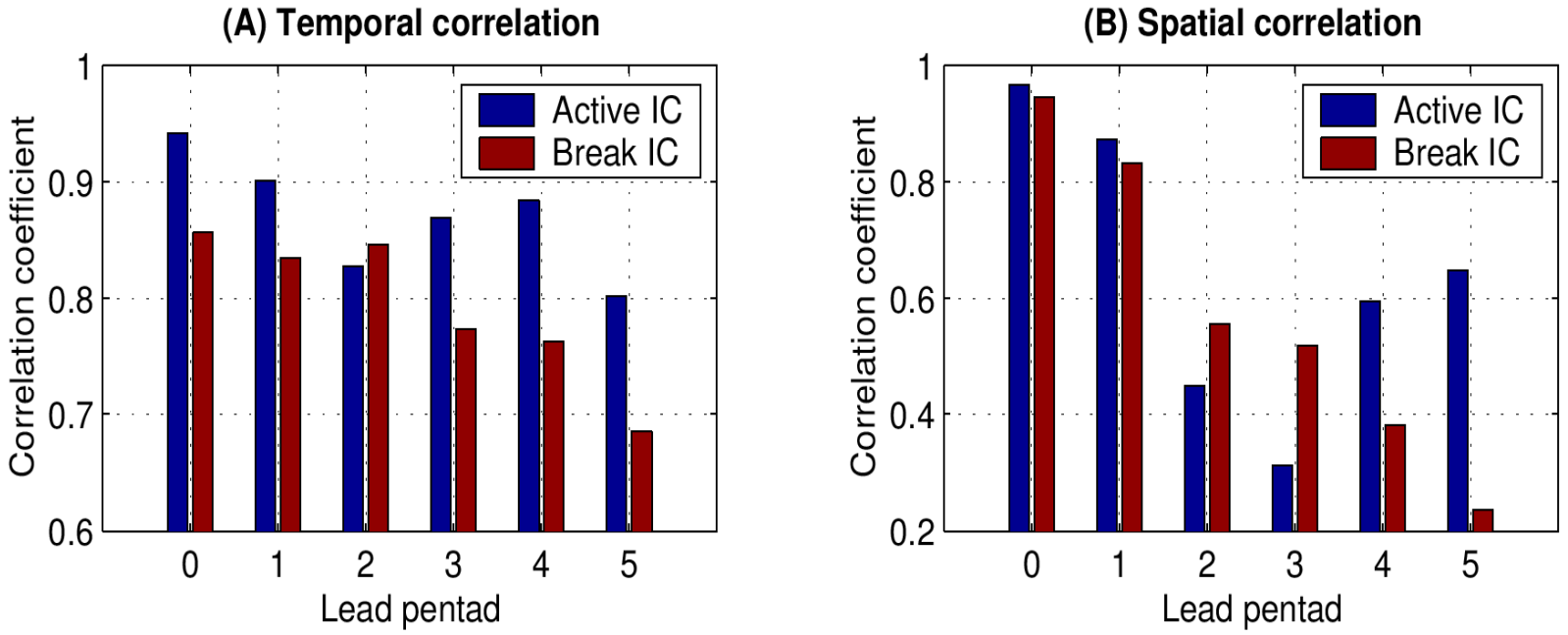

FIGURE 7.14: Temporal and spatial correlations between predictions and observations from active and break initial conditions at different lead times.

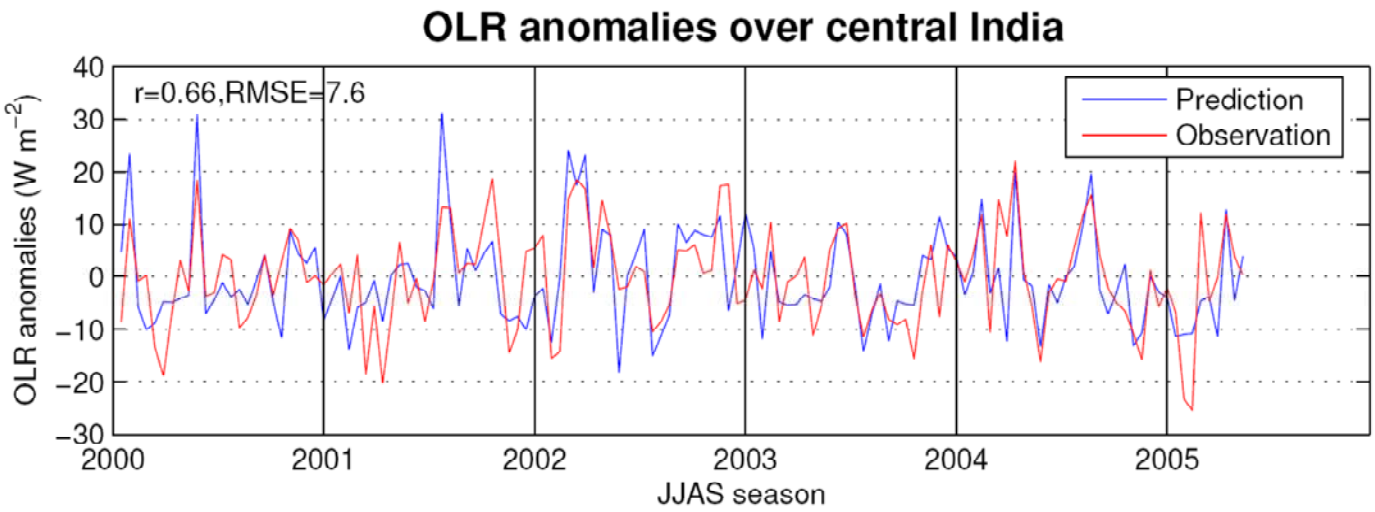

FIGURE 6.11: Prediction of OLR anomalies (W m^{-2}) at 4 pentad lead in comparison with observed values over the region 75°-95°E, 20°-25°N for the JJAS season of the hindcast period.

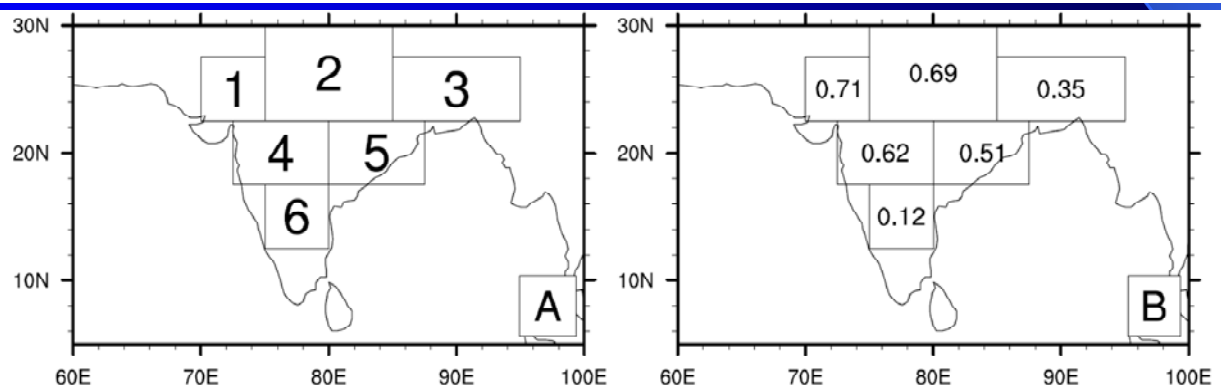

FIGURE 6.13: Regions chosen to evaluate the predictions with observations (A). The correlation coefficient between 4 pentad lead predictions and observations averaged over these regions for the May-October period (B).

This model is currently being used by the India Meteorology Department to make experimental Extended Range prediction of monsoon ISO this year.

Please see the following website

www.imdpune@gov.in

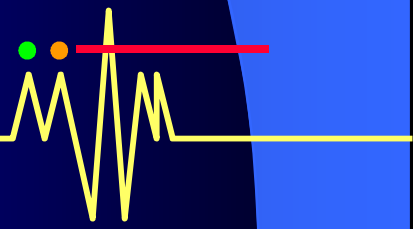

A Nonlinear Model for Real-Time Extended Range Prediction of Active/Break Cycle over Central India

Chattopadhyay,Sahai,Goswami, 2008, JAS

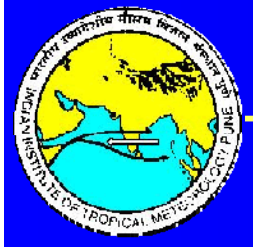

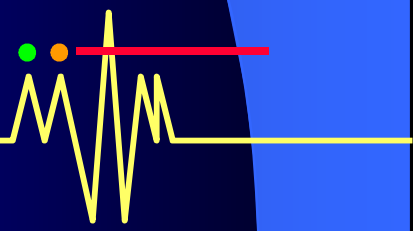

Model 1

1	Precipitation Index **(PR index)*: (*** 70^0E-85^0E, 15^0N-25^0N)
2	Goswami et al. Index **(GO index):** [V850(70^0E-110^0E,10^0S-30^0N) – V200(70^0-110^0E,10^0S-30^0N)]
3	Wang and Fang Index **(WF index):** [U850(40^0 E -80^0E,5^0N-15^0N) - U850(60^0-90^0E,20^0-30^0N)]
4	Webster and Yang Index **(WY index):** [U850(40^0E-110^0E,0^0-20^0N) – U200(40^0-110^0E,0^0-20^0N)] [U850(40^0-110^0E,0^0-20^0N) – U200(40^0-110^0E,0^0-20^0N)]
5	Mean sea level pressure index **(MS index):** msl(65^0E-95^0E,15^0N-25^0N)
6	Specific humidity (850mb) index **(SH index):** Sph850(65^0E-95^0E,15^0N-25^0N)
7	Geopotential Height (500mb) index **(GP index):** Gph500(65^0E-95^0E,10^0N-20^0N)
8	**U-shear index**: [U850(100^0E-140^0E,15^0S-5^0N)-U200(100E-140E,15s-5N)]
9	**Omega** (vertical velocity at 500 mb) index: w500(50^0E-115^0E,0^0N-7.5^0N)-w500(80^0E-150^0E,10^0N-20^0N)
10	**Mean Sea level Pressure shear Index**: msl(110^0E-150^0E,10^0N-20^0N)-msl(40^0E-60^0E,15^0S-5^0N)

RF data used for verification

Model 2

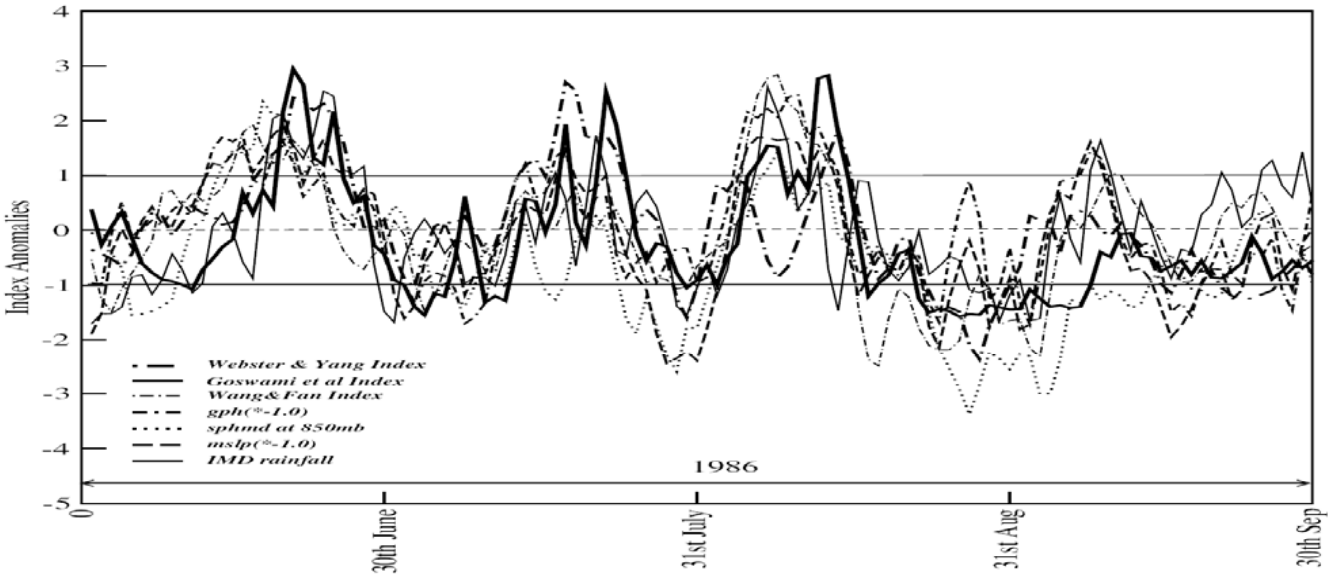

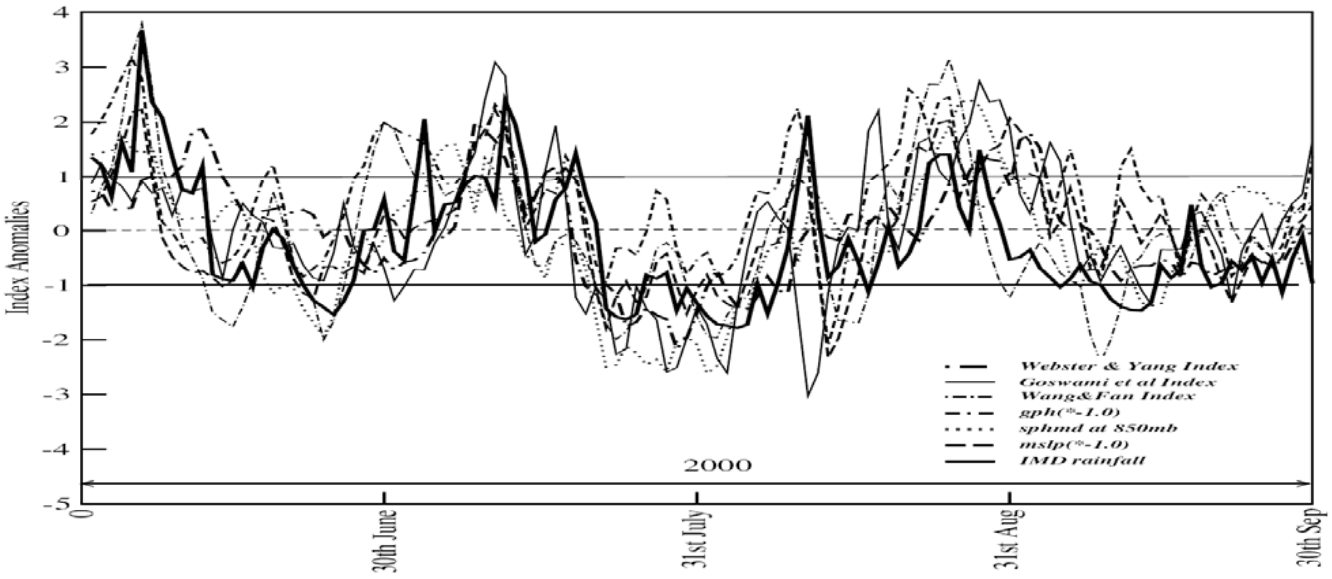

Normalized anomalies of six different indices during June-September of 1986 and 2000

We propose that the dominant monsoon ISO is nonlinear Convectively coupled oscillation

- Thus a unique relationship between a number of dynamical fields representing a nonlinear phase of the oscillation should be uniquely related a phase of the rainfall oscillation

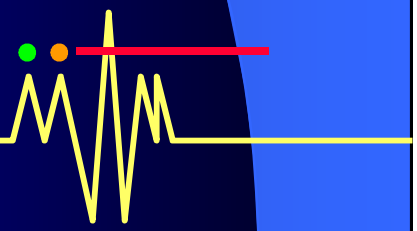

The SOM Algorithm

A non-linear classification scheme using the self-organizing map (SOM) which falls under the category of unsupervised learning neural network technique (i.e. learning without human

intervention or any pre-condition)

(Kohenen, 1990; Hewitson and Crane 2002)

- The SOM consists of a (usually) one or two dimensional array of identical neurons. The input vector is broadcast in parallel to all these neurons.

- For each input vector, the most responsive neuron is located. The weights of this neuron and those within a neighborhood around it are adapted to reduce the distance between its weight vector and the current input vector.

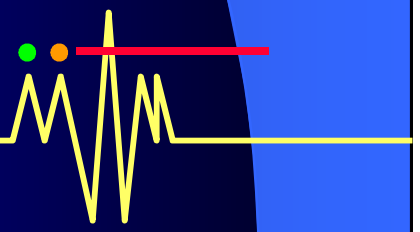

THE SOM NETWORK

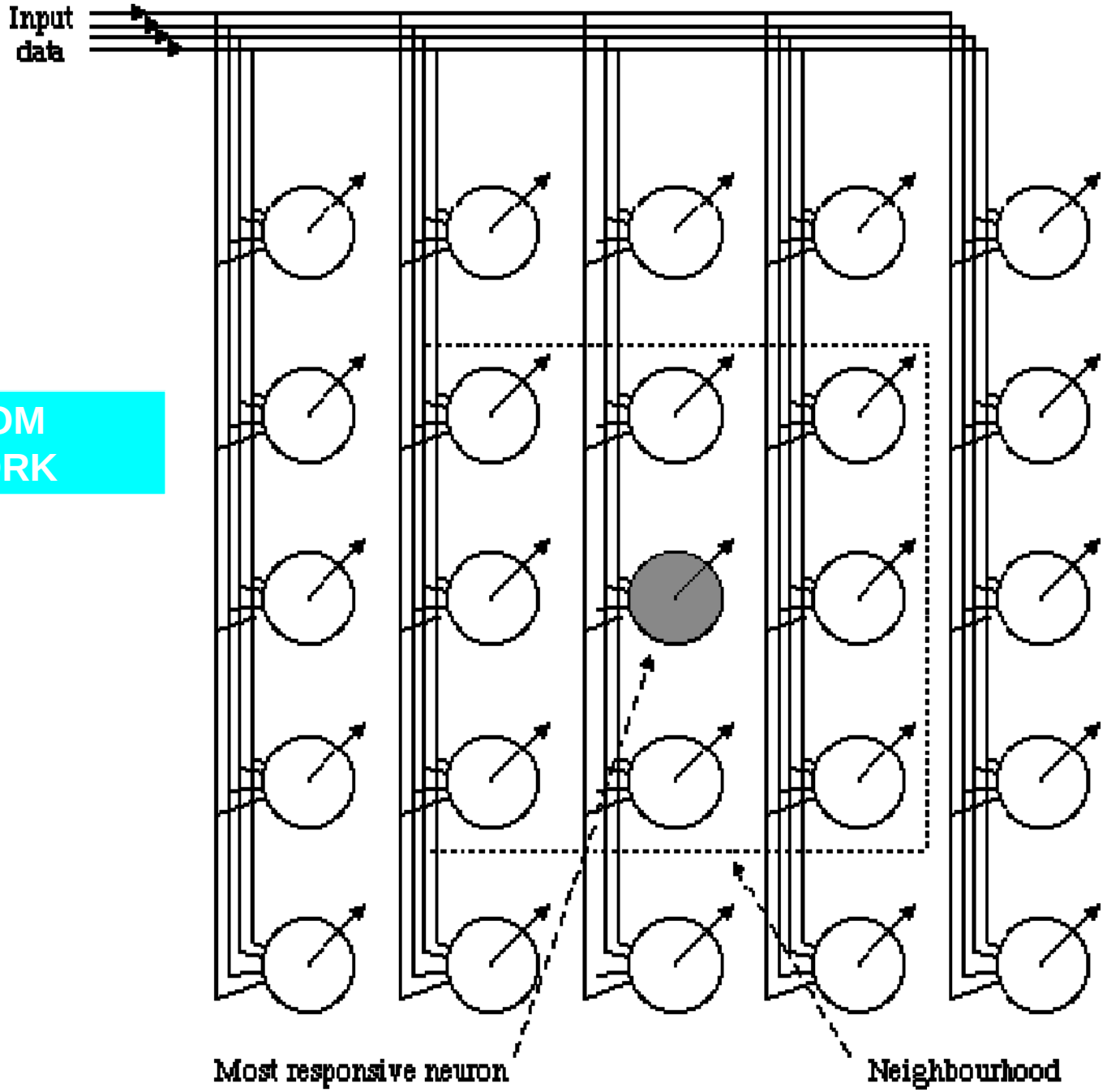

The SOM training for the nth iterative step is given by:

$$W_j(n+1) = W_j(n) + c(n)\{x(n) - W_j(n)\} \quad j \in R(n)$$

$$= 0 \qquad \text{otherwise}$$

$W_j(n)$ is the weight vector for the jth node at the nth step of iteration.

$c(n)$ is the learning rate at the nth step.

$R(n)$ is the neighborhood for the nth step.

The inclusion of neighbor hood makes the learning rate non-linear.

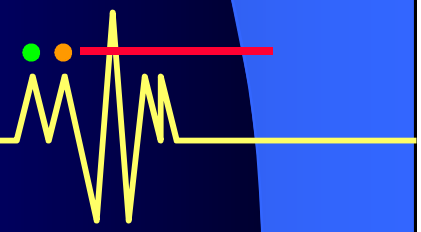

Some application of the SOM algorithm in the study of Indian summer monsoon.

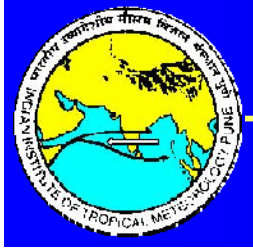

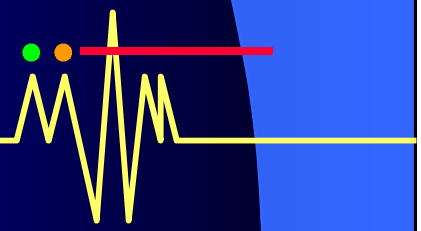

1. **Identification of active and break patterns of Indian summer monsoon using large scale dynamical parameters.**

A. Data Used: ERA-40 data from 1980-2001.NCEP data from 1951-2004. IMD daily gridded rainfall data from 1951-2004.

Parameters: U850,U200,V850,V200,MSLP,Sph850,Gph500 and Rainfall

The large scale indices are constructed based on this data and are used to classify the data using SOM. The data is classified as 3x3 clusters.

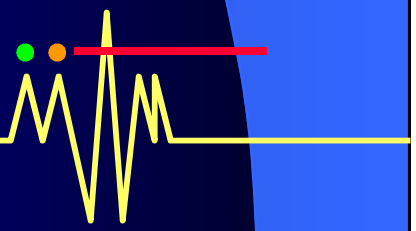

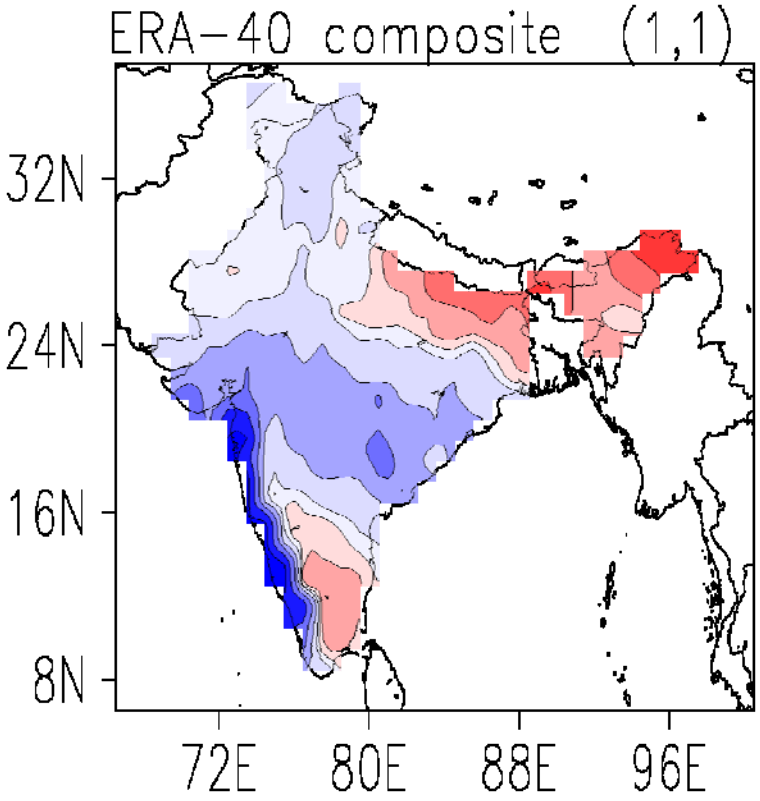

Active SOM

Break SOM

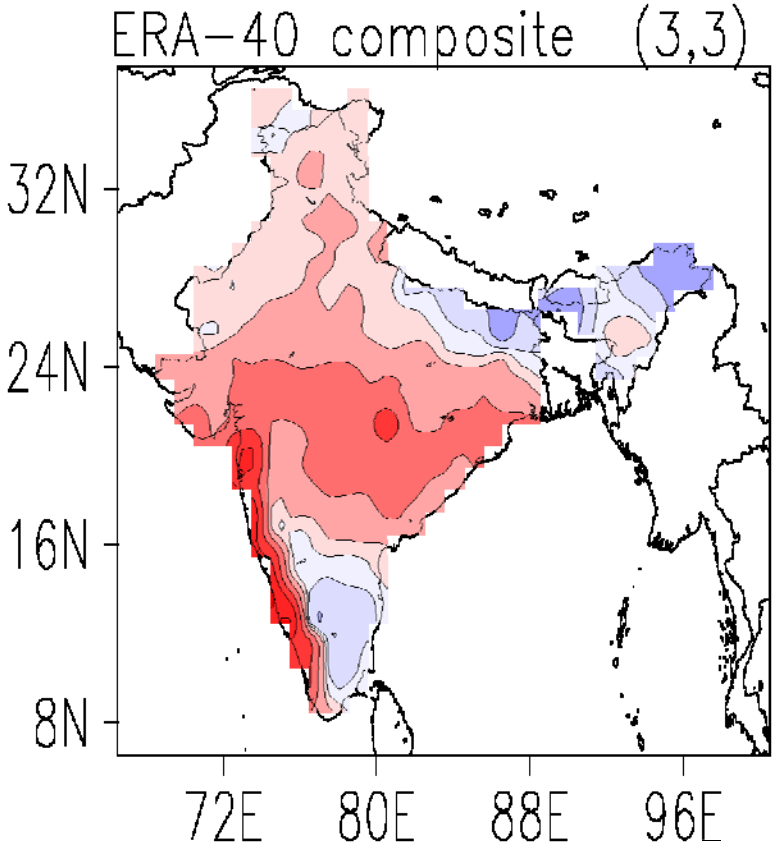

Area averaged rainfall anomaly over central India

(1,3)	(2,3)	(3,3)
-0.32	-1.38	-3.43
(1,2)	**(2,2)**	**(3,2)**
1.11	0.09	-1.73
(1,1)	**(2,1)**	**(3,1)**
4.14	1.96	-0.59

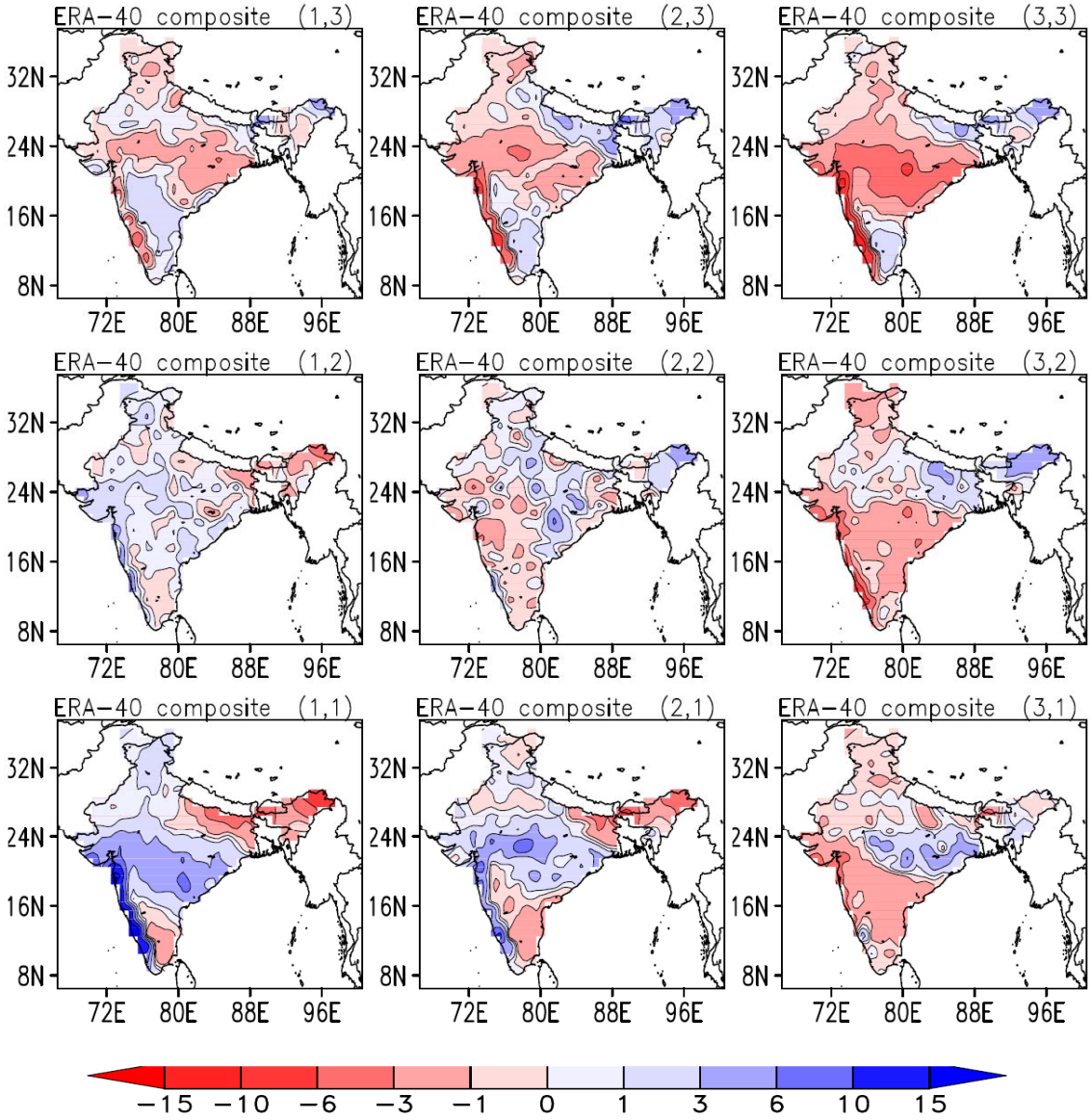

Figure 4: The spatial distribution of anomalous precipitation associated with SOM classified patterns .It is obtained by compositing the IMD daily rainfall anomaly corresponding to the days clustered at the respective SOM nodes. The states (1, 1) and (3, 3) are the most active and break nodes. (units $mm\ day^{-1}$)

The 3x3 SOM clustering.

Plotted here are the composite spatial plot of rainfall anomaly for the dates clustered at each SOM nodes

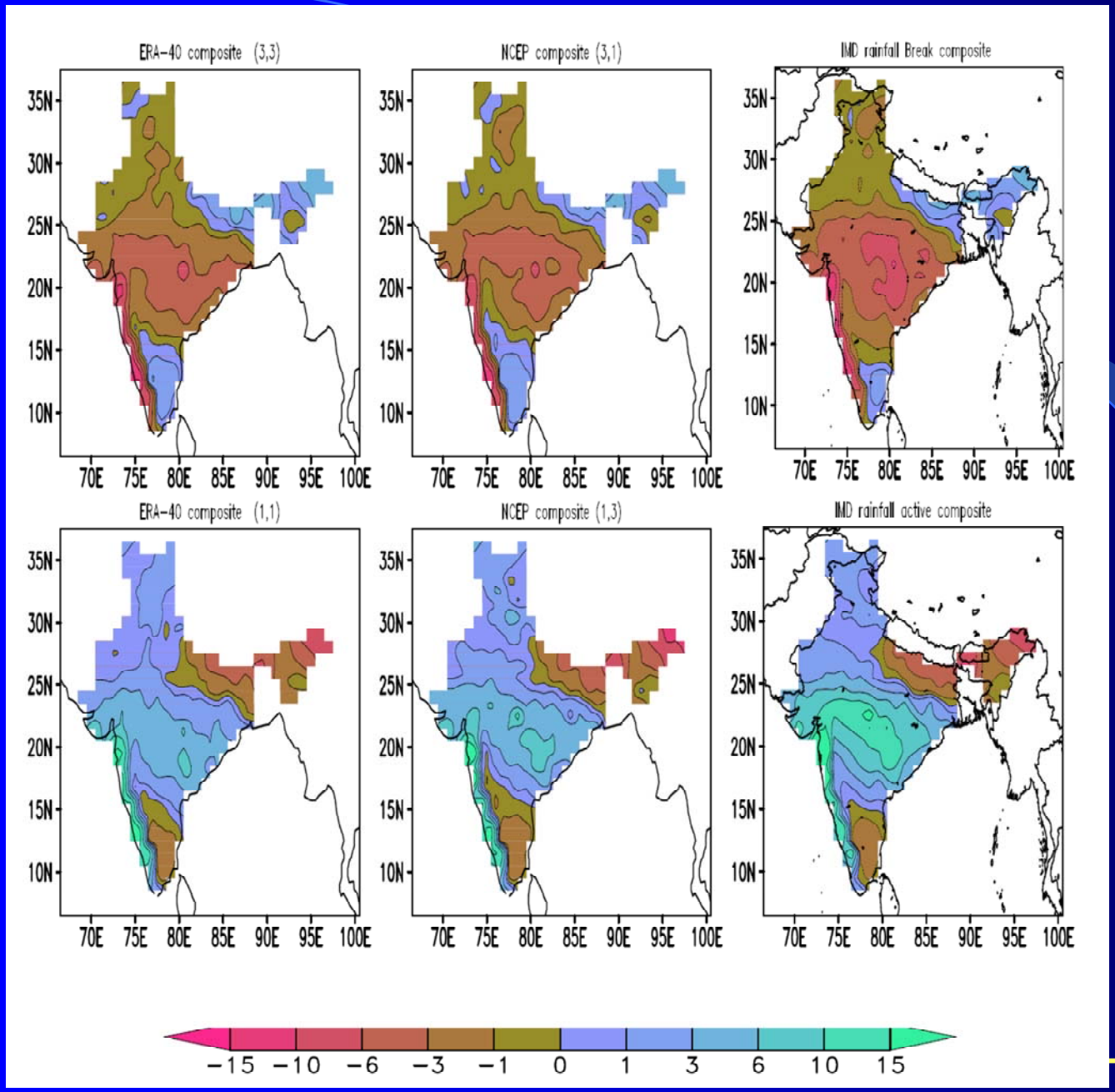

Break (top) and active (bottom) composites through SOM clustering using large scale circulation data from ERA-40 (left), NCEP (middle) and from IMD precip data (right).

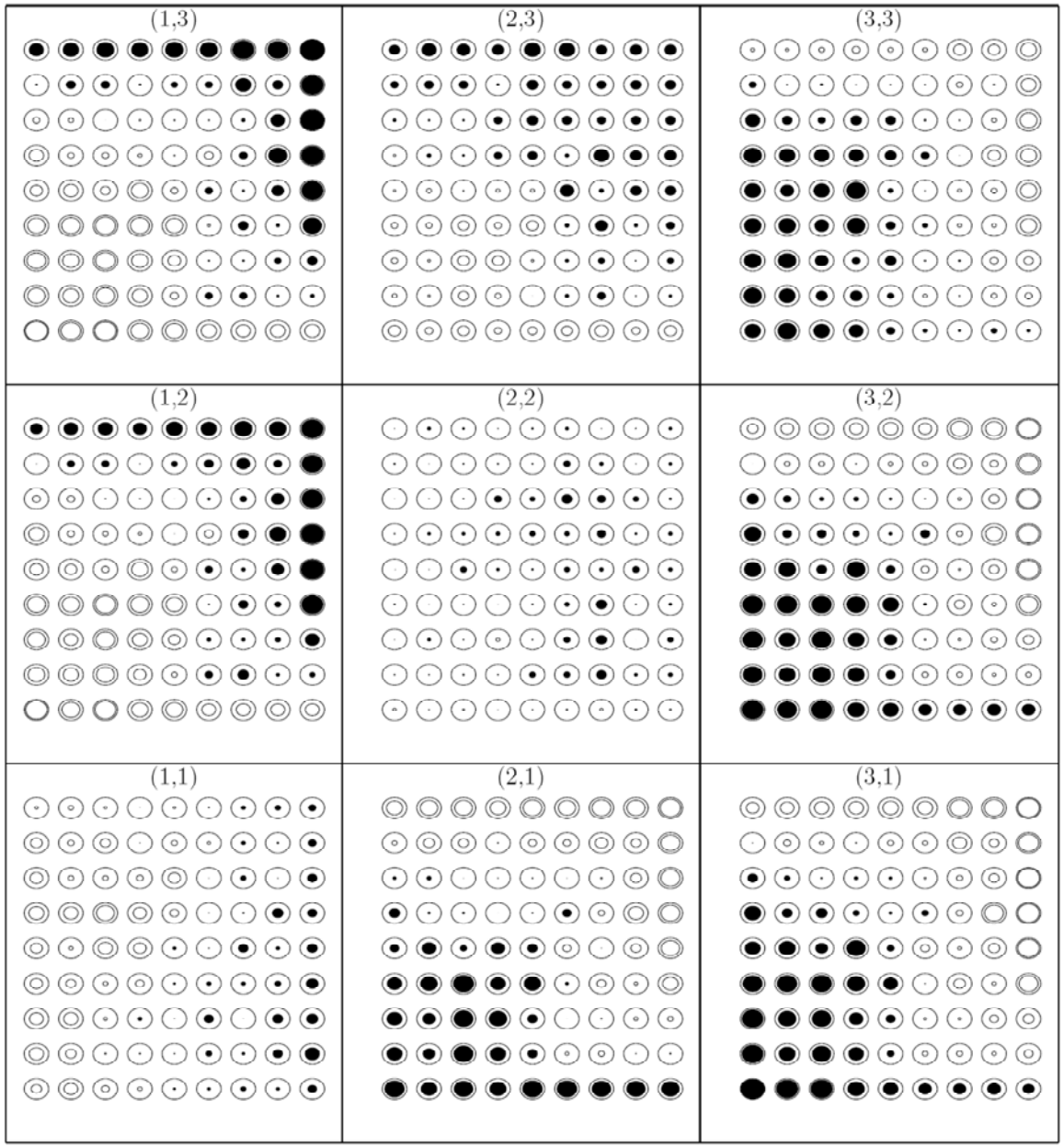

Pattern correlation between each of 3X3 (9) SOM patterns of precipitation and those of 81 patterns associated with 9X9 SOM classification

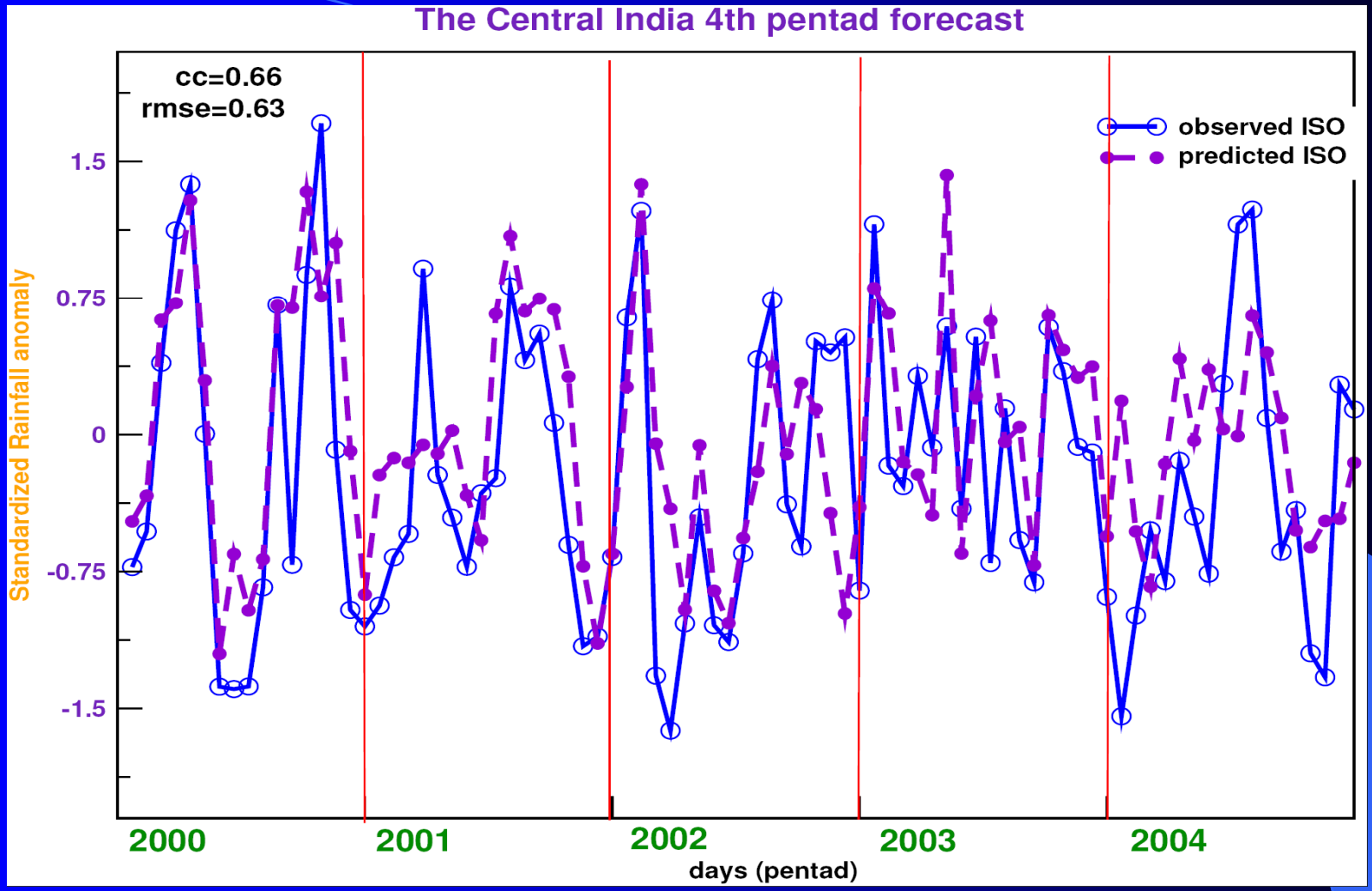
The Central India 4th pentad forecast
cc=0.66
rmse=0.63
observed ISO
predicted ISO
Standardized Rainfall anomaly
1.5
0.75
0
-0.75
-1.5
2000
2001
2002
2003
2004
days (pentad)

CONCLUSION

- Summer monsoon ISOs have large amplitude, as large as the annual cycle and much larger than IAV of seasonal mean.
- On one hand they cluster synoptic activity while on the other they produce internal IAV of seasonal mean. Thus, monsoon ISOs are the building block for monsoon climate
- Quantitative estimate of potential predictability of the summer monsoon ISOs indicate useful prediction of breaks should be possible 20-25 days in advance.
- Summer monsoon ISOs are nonlinear convective coupled oscillations. Large scale circulation may be sufficient to predict Rainfall ISO.
- 'Analogue models' have emerged as useful real time forecasting tool for Extended range prediction (3-4 weeks in advance) of 'active' and 'break' spells

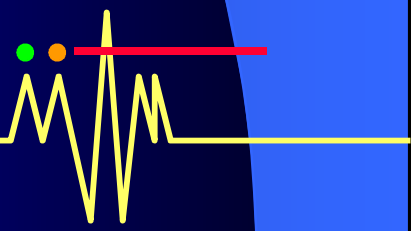

Real-time monitoring of the northward propagating MISO

Suhas, E, Neena J. M. and Goswami, B. N. 2012,
Climate Dyanmics (online)

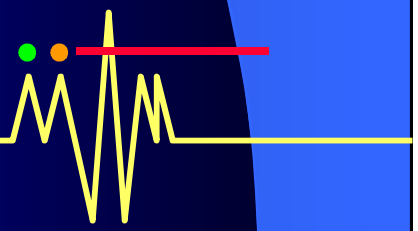

- **Strong seasonal dependence to off-equatorial behaviour (but still "MJO" in all seasons)**

Courtesy: M. Wheeler

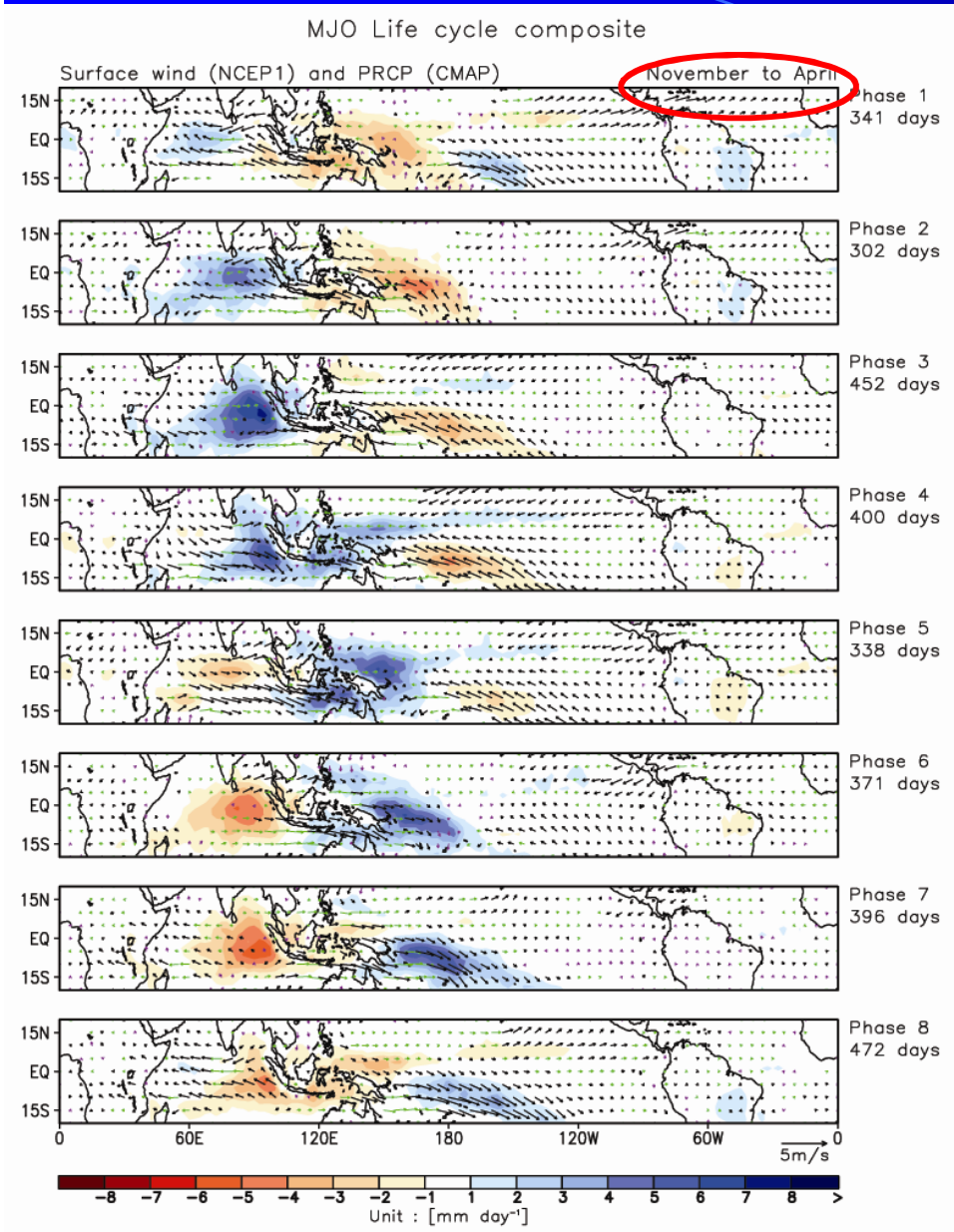

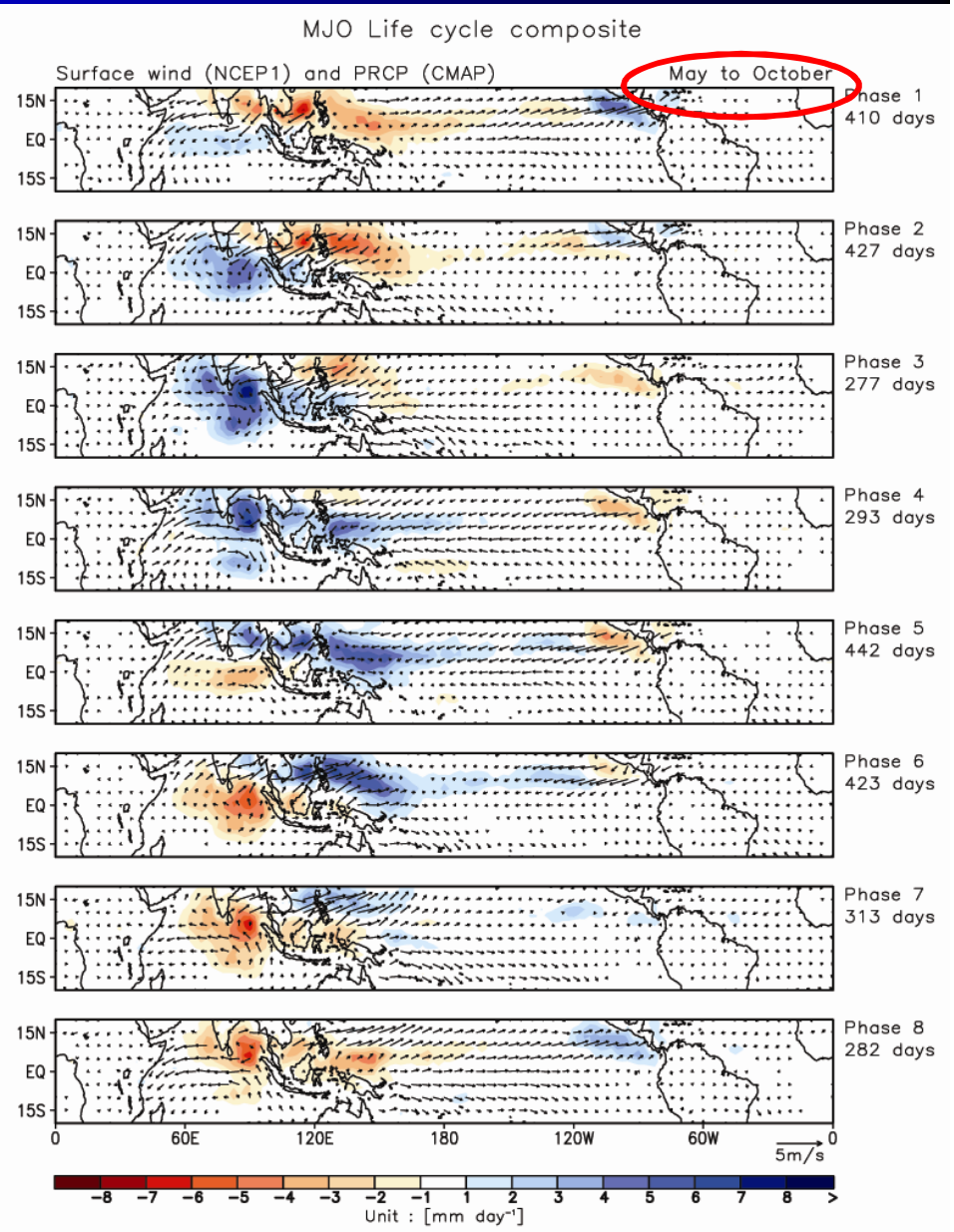

Each phase is separated, on average, by about 6 days

Multivariate EOF analysis: Useful for extracting convetively-coupled structure, and for generating a MJO phase index.

All seasons

15°S-15°N averaged data.

These EOFs are virtually independent of season!

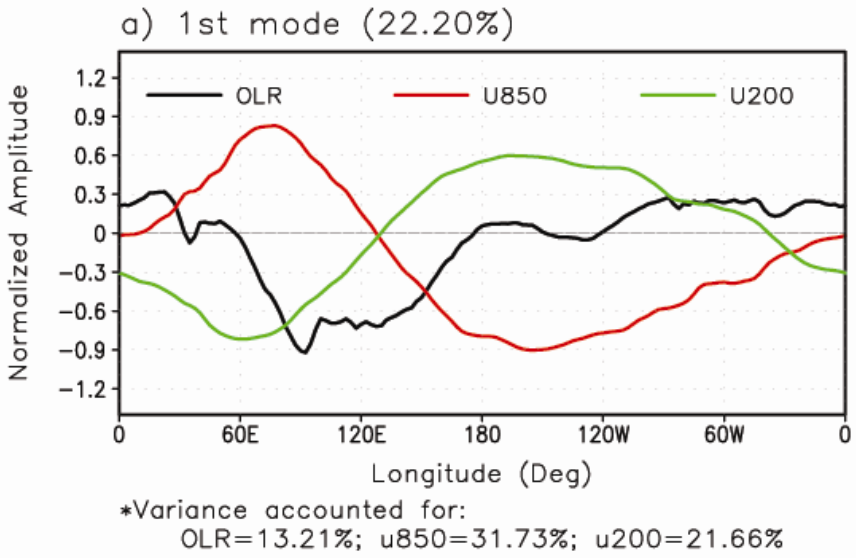

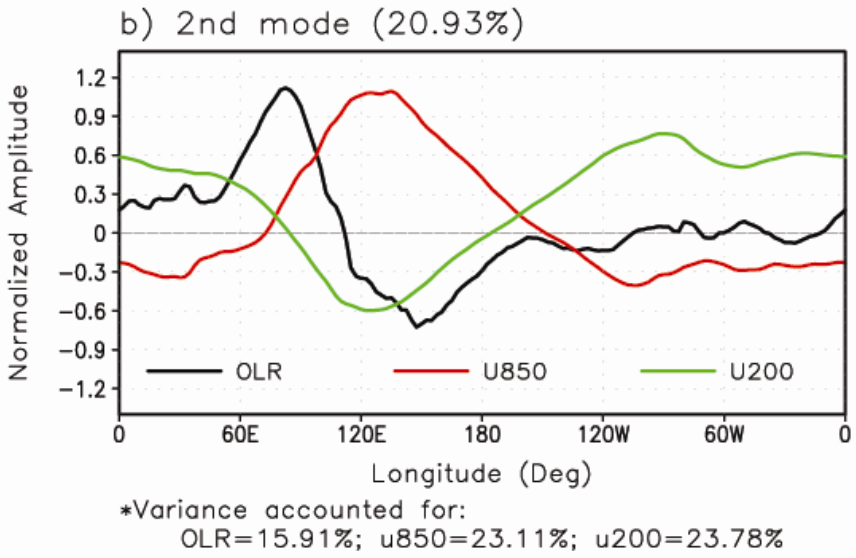

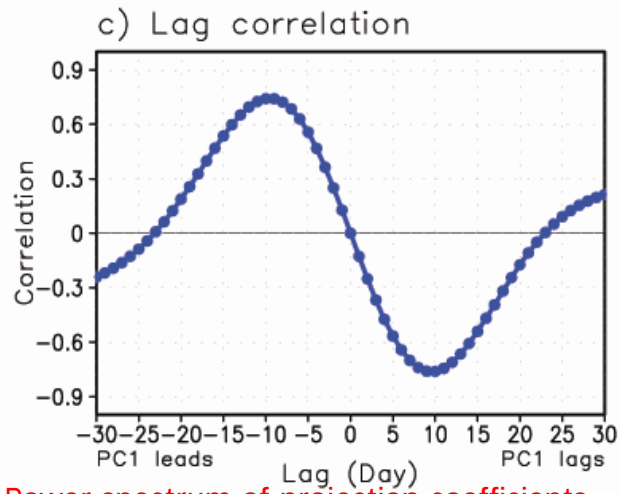

Power spectrum of projection coefficients obtained by projecting unfiltered data on the EOFs.

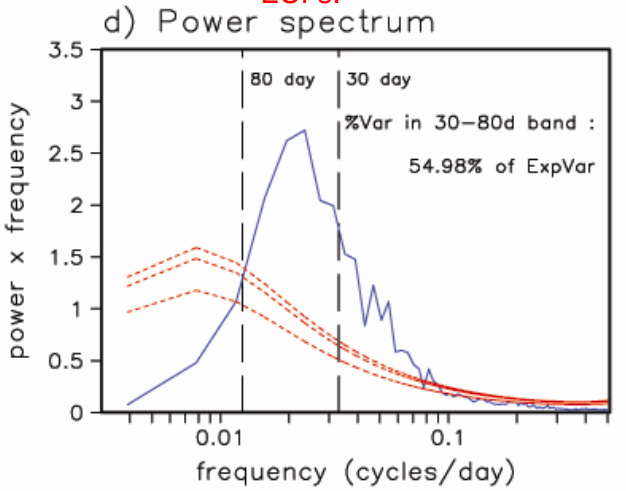

This analysis is the same as applied by **Wheeler and Hendon (2004),** except used 20-100d filtered data as input.

For compositing, phases may be defined from the leading pair of principal component (PC) time series.

Note the ‘smoothness’ of the phase-space trajectory because of the use of filtered data.

“Weak MJO” defined to occur when $PC1^2 + PC2^2 < 1.0$.

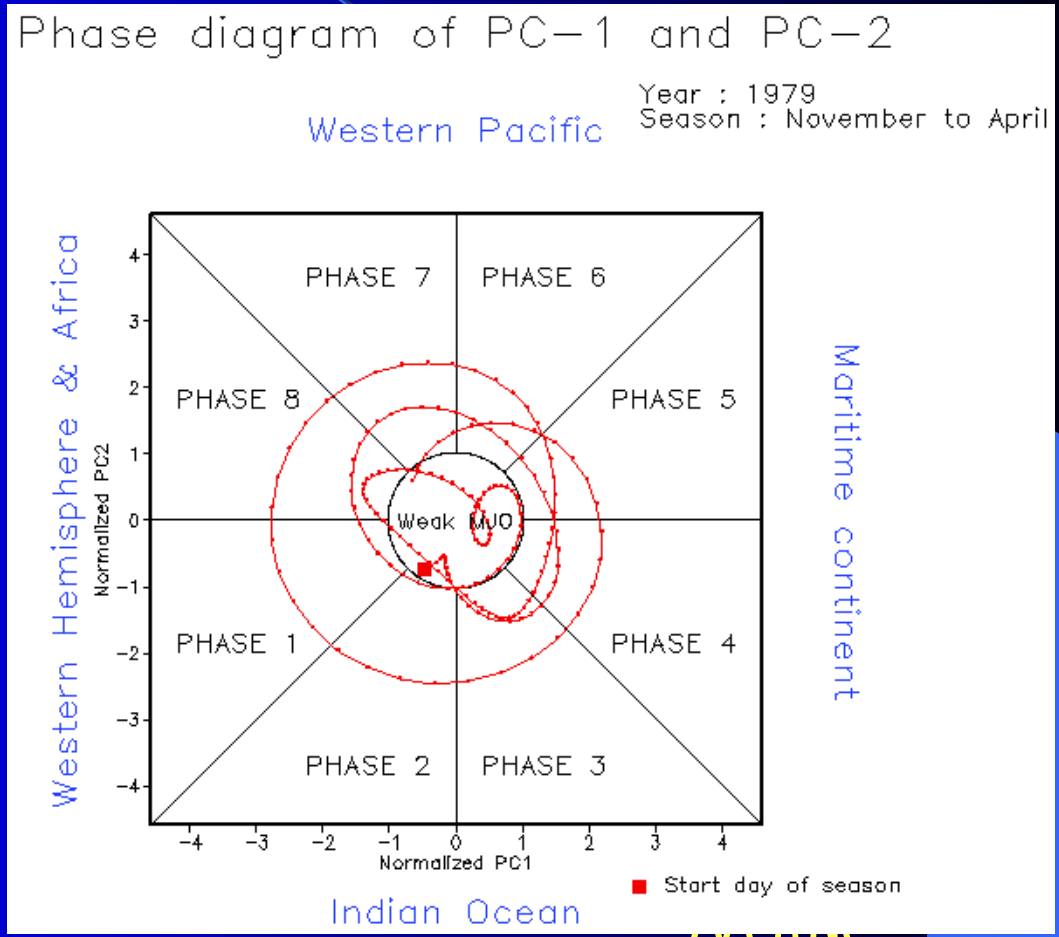

MJO and MISOs are two different entities . . . . .

Centers of action & propagation characteristics are different.

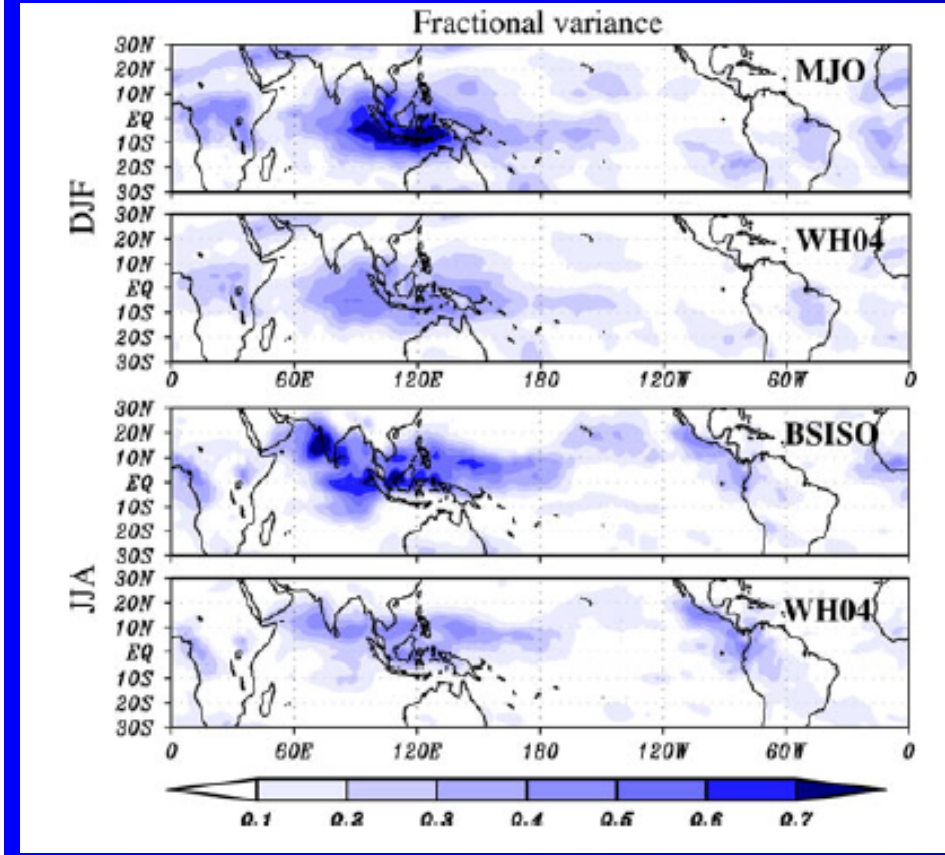

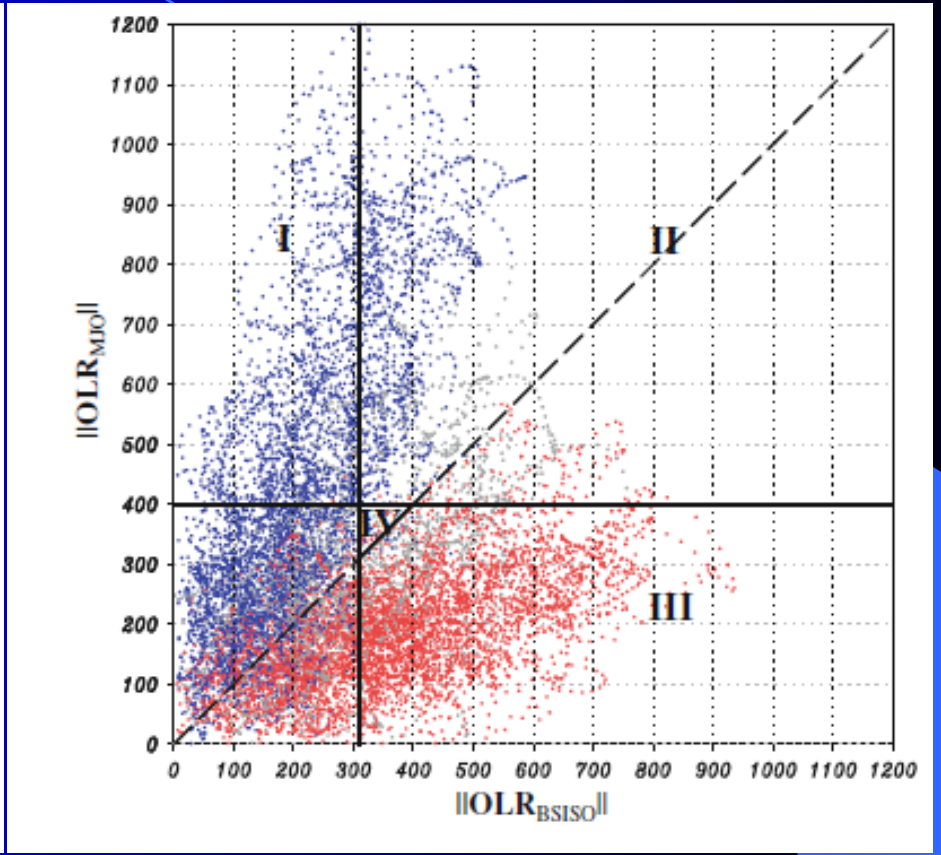

(Kikuchi et al. 2011, Clim. Dyn.)

Background…..

- **Active/Break rainfall spells are largely governed by northward propagating 30-60 day monsoon intraseasonal oscillations (Goswami 2005).**
- **The boreal summer MISO mode is distinctly different from the eastward propagating MJO mode (Kikuchi et al 2011).**
- **In contrast to the equatorially trapped spatial structure of the MJO, the MISO shows an off-equatorial structure with strong convective activity over the south Asian region.**
- **A real-time monitoring index for the MISO similar to the RMM indices for the MJO (Wheeler and Hendon, 2004) has been lacking so far.**
- ***Proper isolation of the 30-60 day mode from the westward propagating 10-day mode and high frequency synoptic scale is required.***

Lag composite of MISO: 25-90 day (GPCP JJAS)

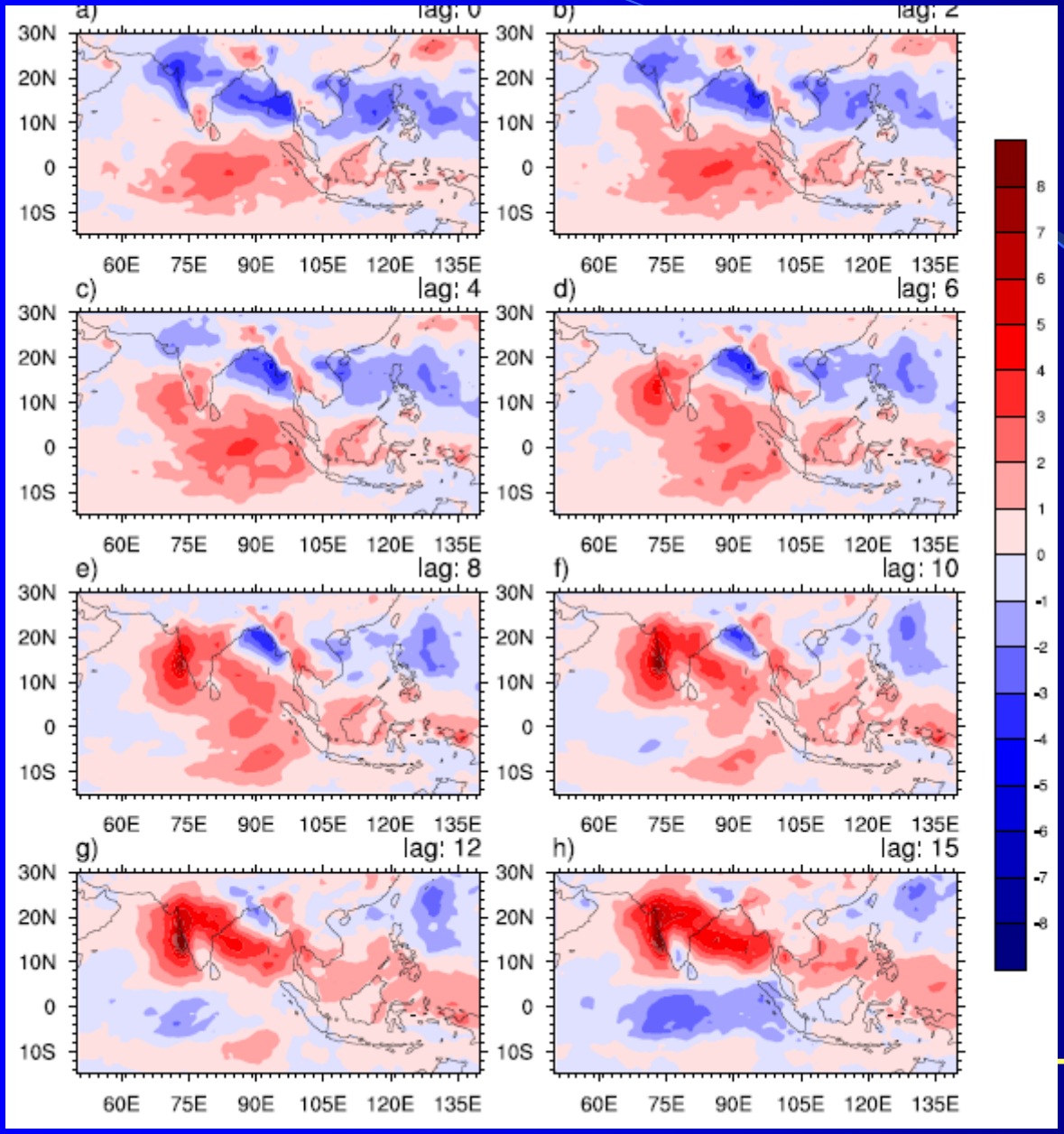

MISO evolution one half cycle

Extended EOF (EEOF)analysis & a low dimensional MISO index

EEOF captures the spatial &temporal evolution.

It has been demonstrated that first two EEOFs can represent a whole cycle .(Lau and Chen 1986, Kayano &Kousky 1999, Waliser et al 2003, Roundy et al 2009)

Methodology

- **Remove climatological mean and annual cycle.**
- **Augment the original anomaly data with different time lags**
- **Compute the EOFs (eigen values) of the augmented matrix.**
- **Projection of 1st two EEOFs on to the data gives corresponding PCs.**

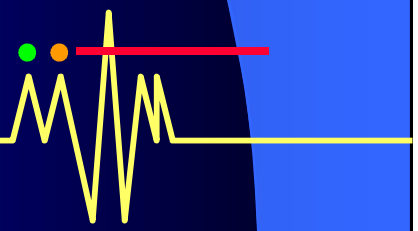

First two EOFs and PCs of EEOF

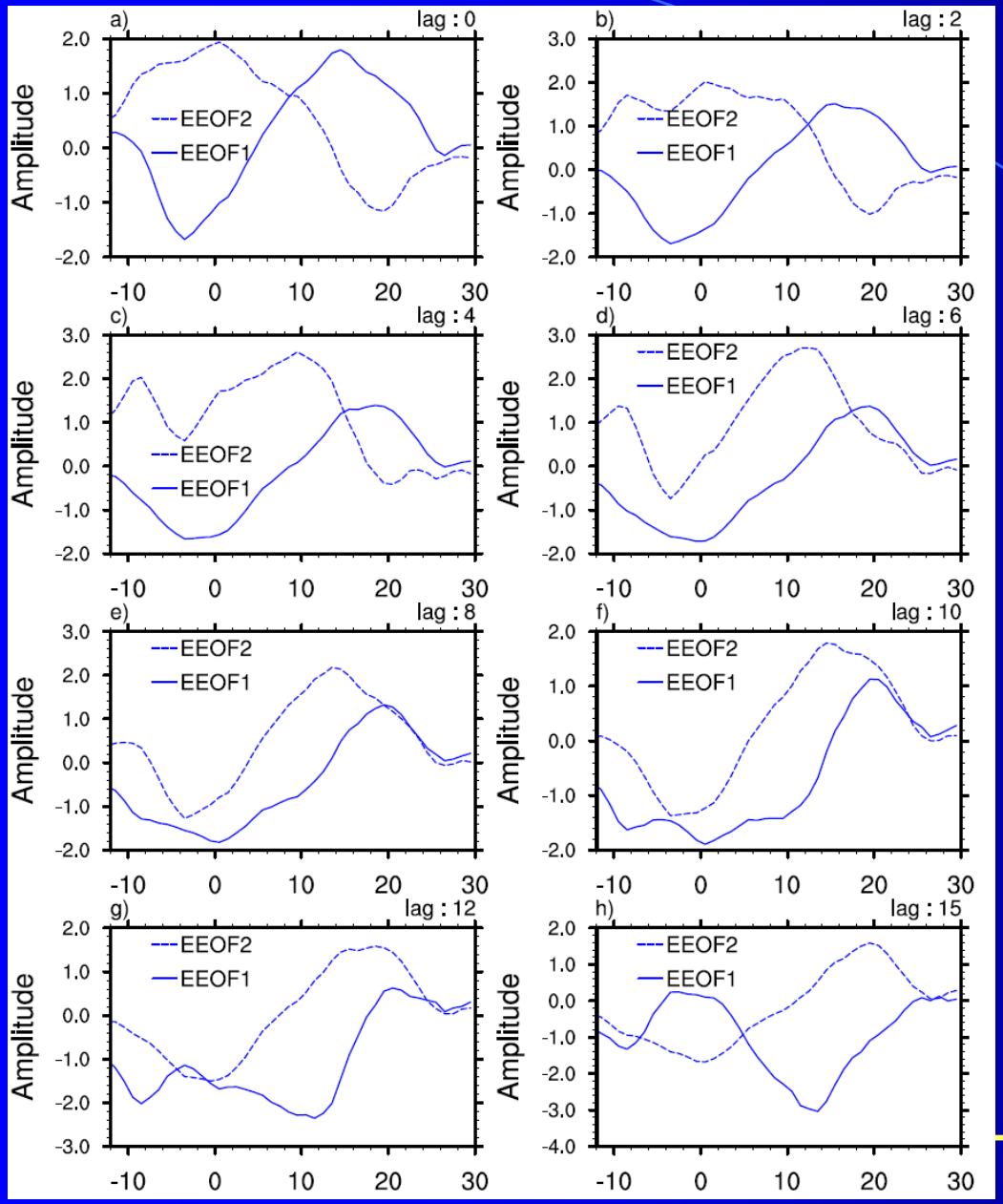

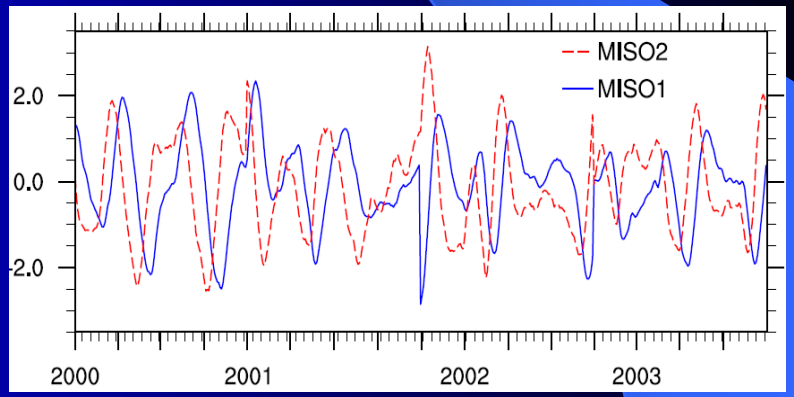

Analysis of the MISO indices

Power Spectra

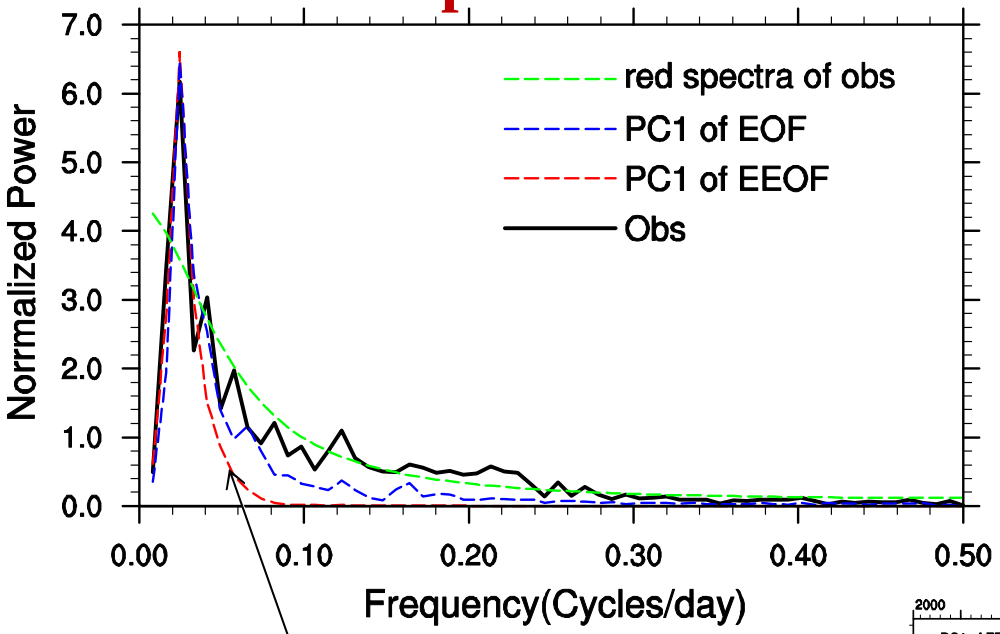

Neatly isolates the MISO signal

Clearly separate 10-20 day mode & synoptic scale

Comparison of MISO indices with filtered & unfiltered anomalies

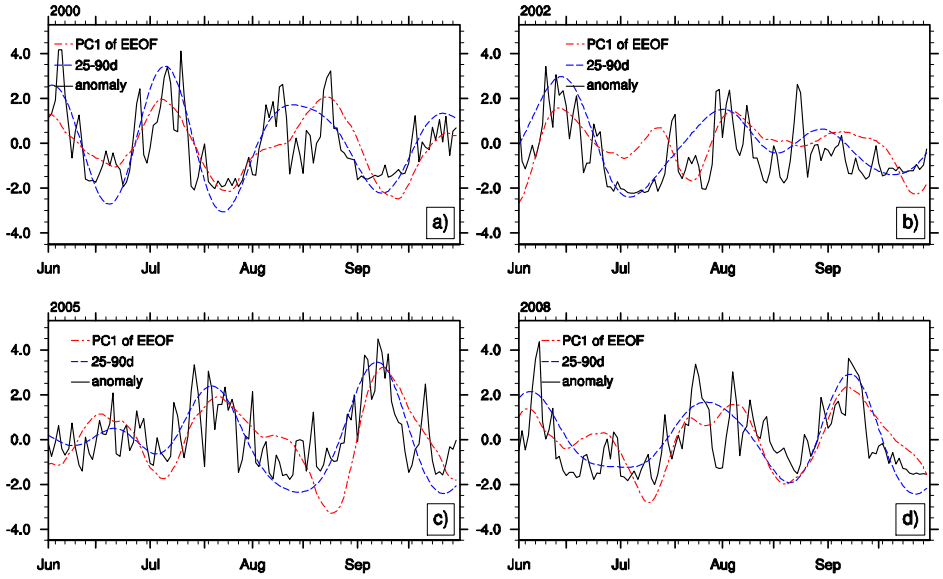

North-south space-time spectra

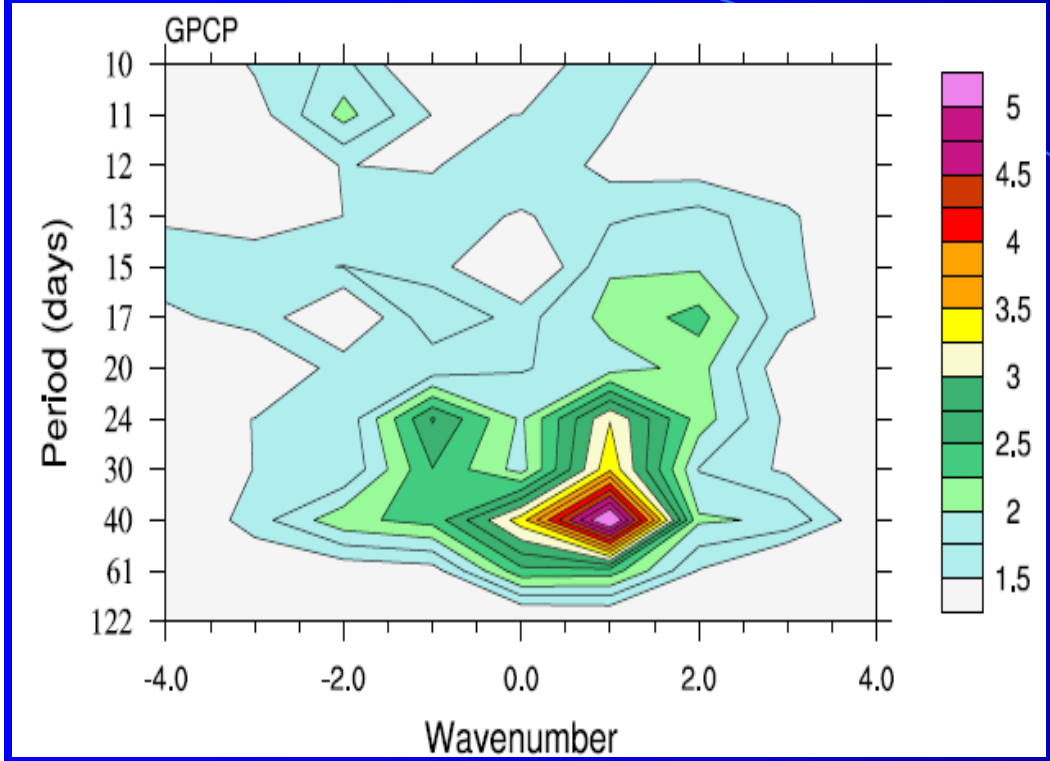

Lag correlation

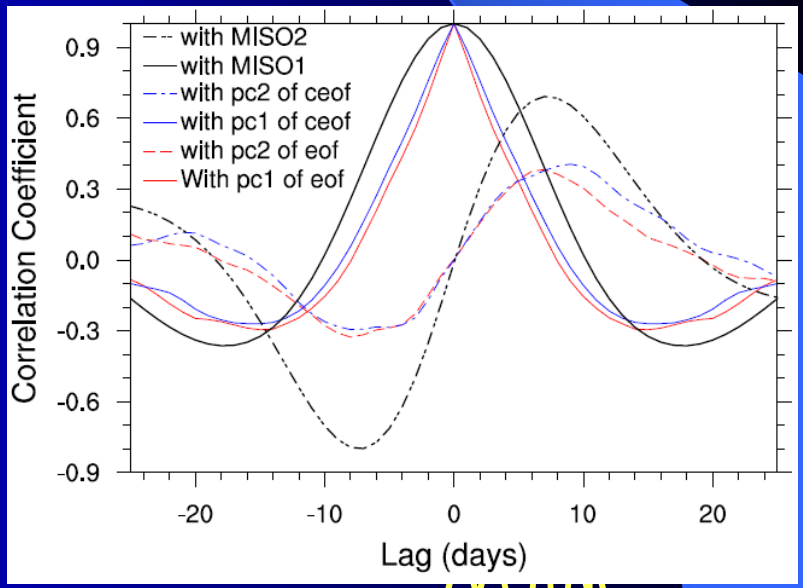

Phase composite of precipitation anomaly

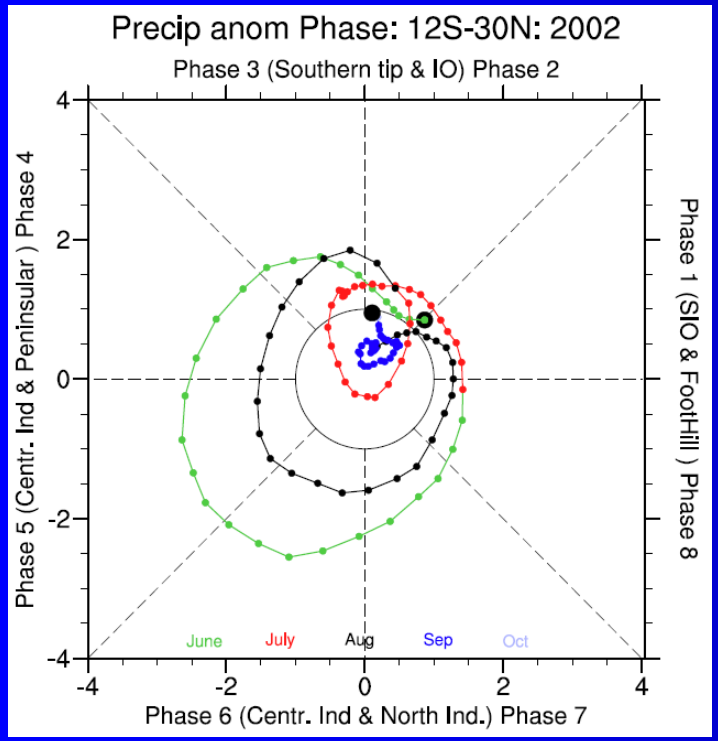

MISO2

MISO1

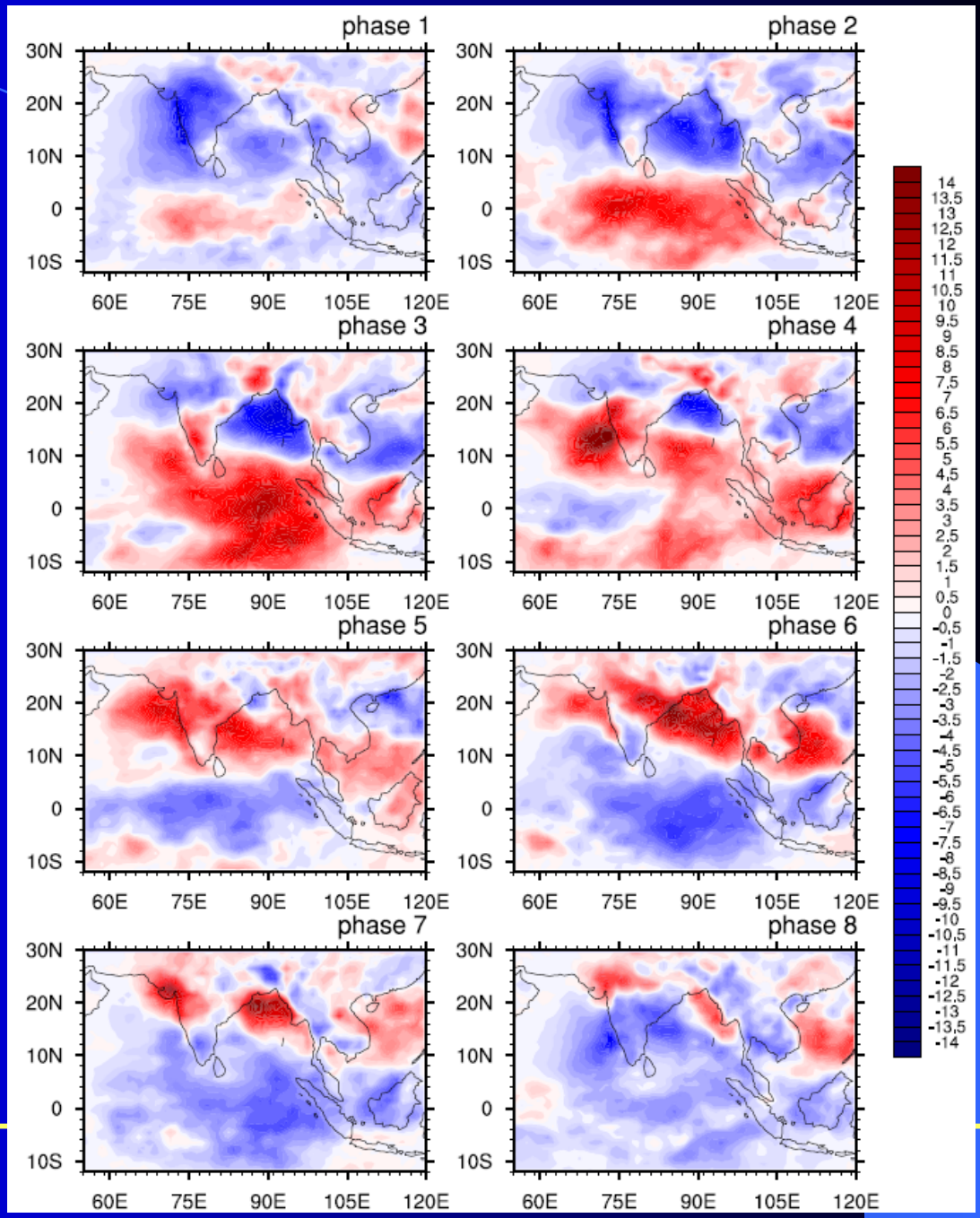

Interannual variability of Indian monsoon ISOs

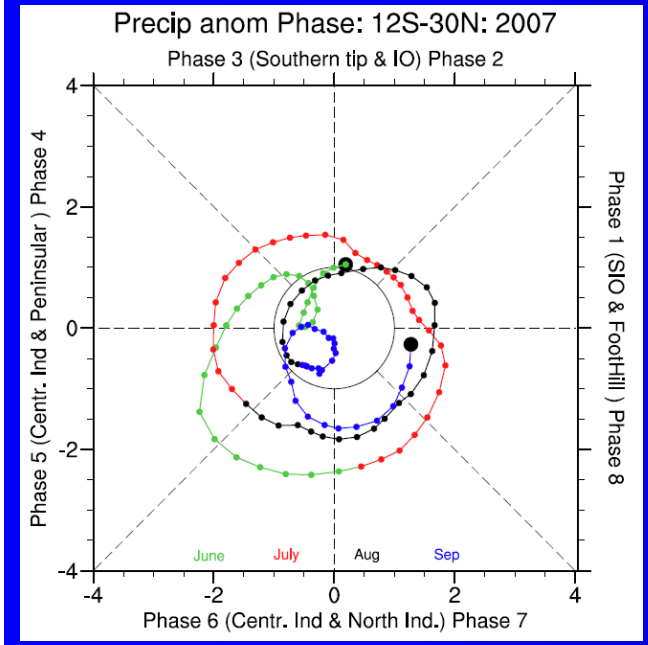

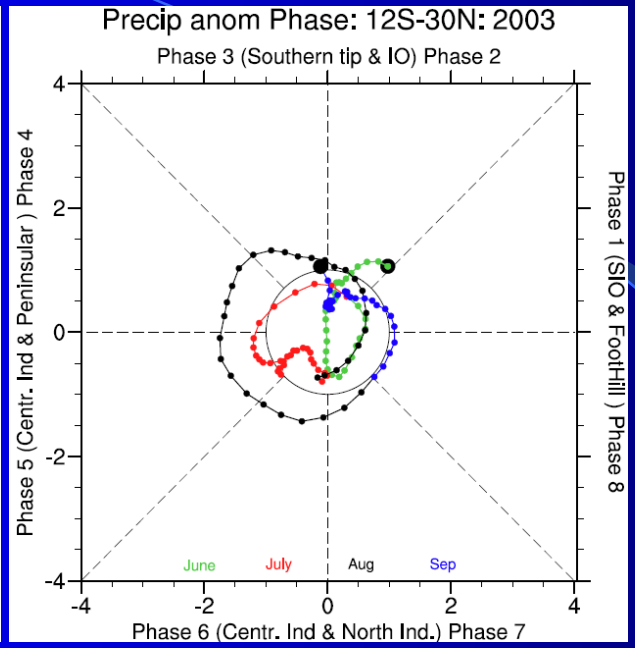

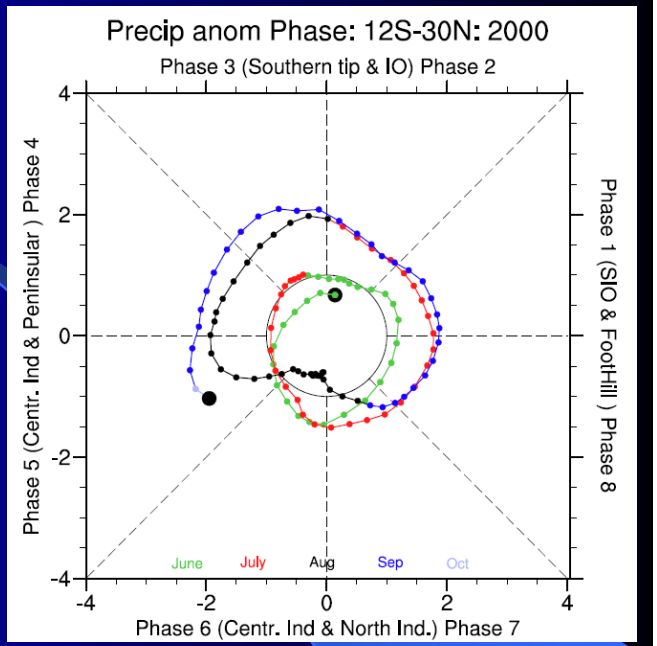

Behavior of ISOs during Jan-April On MISO space

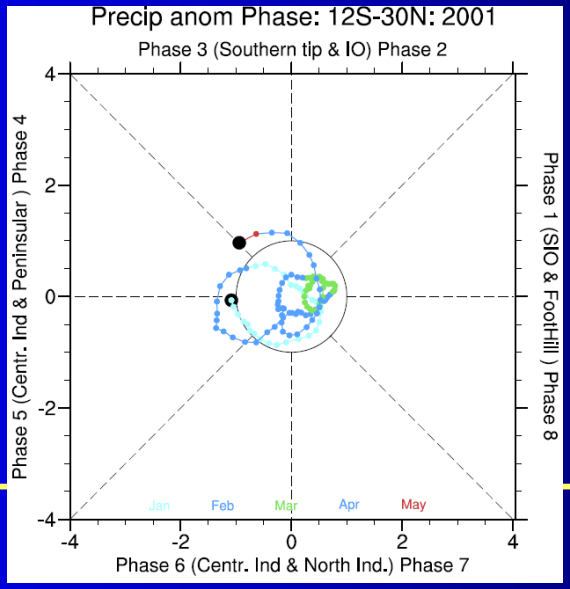

Verification of Extended Range Prediction of MISO by CFSv.1 and CFSv.2

Goswami et al. 2012, GRL (under review)

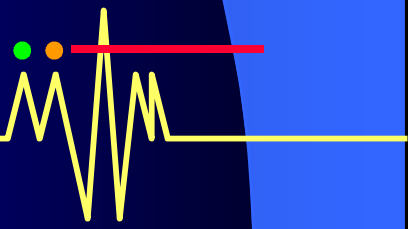

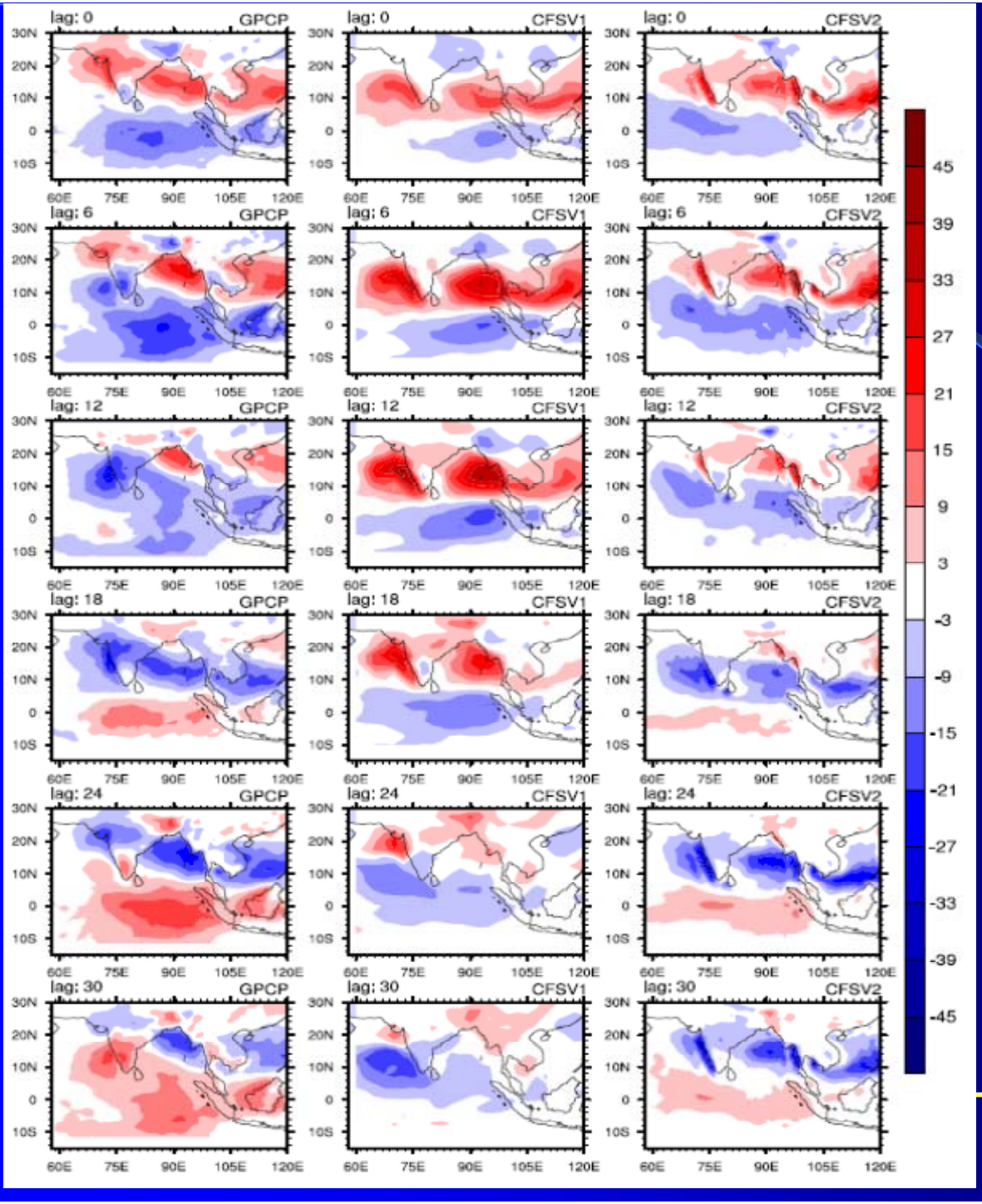

Figure 1: First EEOF of precipitation is plotted for up to 30 day lags with an interval of 6 days for observation (left panel), CFSv.1 (middle panel) and CFSv.2 (right panel). Units are arbitrary.

Extended Range Prediction Experiments with CFSv1 and CFSv2

- CFSv1 : Hindcast Period 2001-2007. Starting from May 1, an ensemble of 11, 45-day forecasts are made from initial conditions every alternate 5 days. Ensemble members are generated by a perturbation technique.
- CVSv2: NCEP already had one 45-day forecasts every 6-hour analysis cycle. For any initial condition, taking 5 forecasts immediately before and 5 after, an 11-member ensemble is created
- Ensemble mean precipitation at each grid points taken
- Projected to observed EEOF1 and EEOF2 and get predicted MISO1 and MISO2

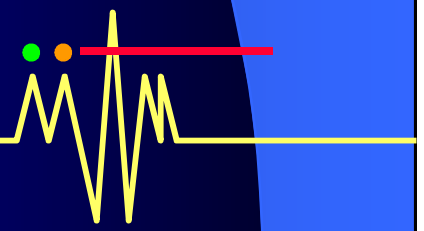

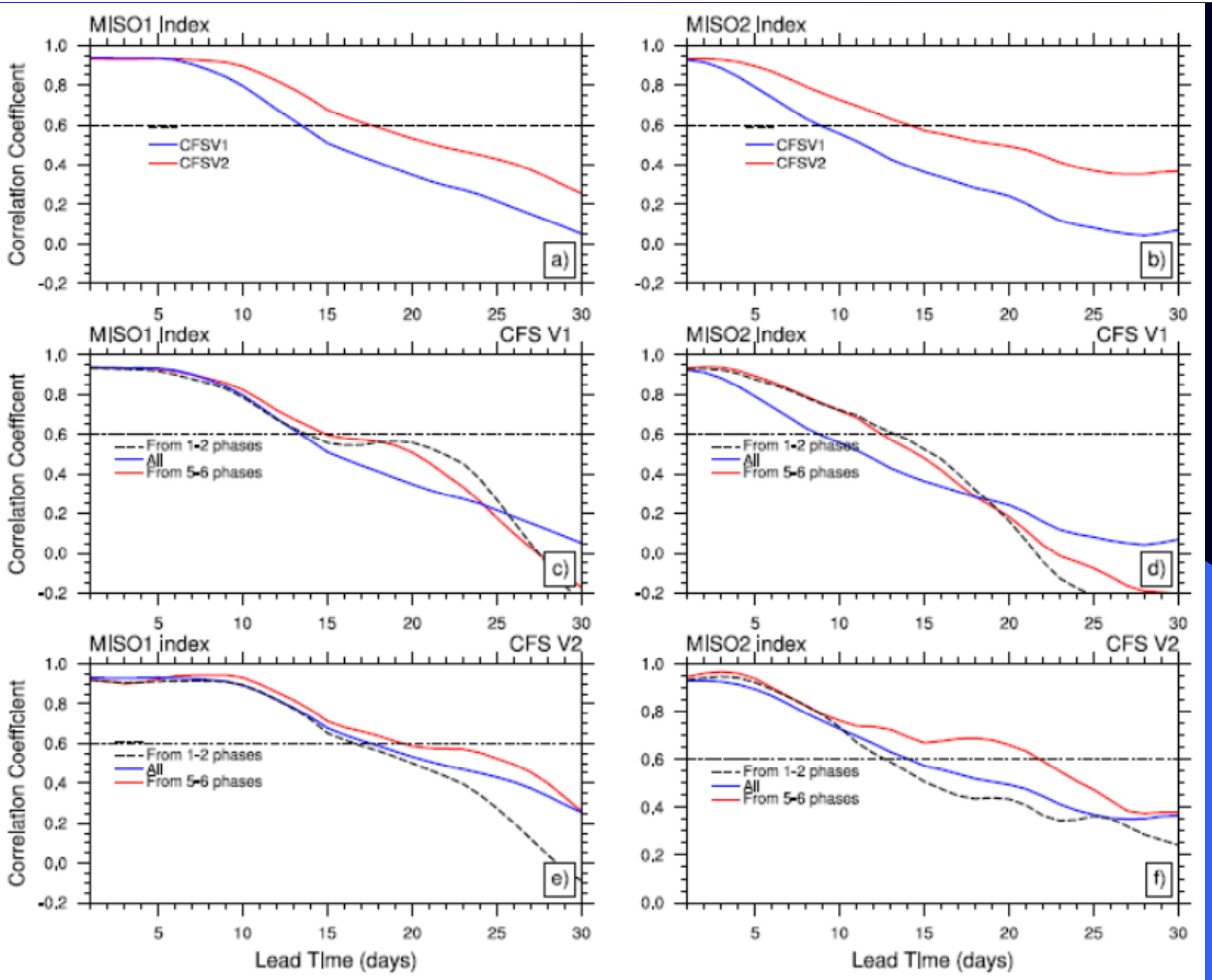

Correlation between observed and predicted MISO1 and MISO2 as a function of lead time

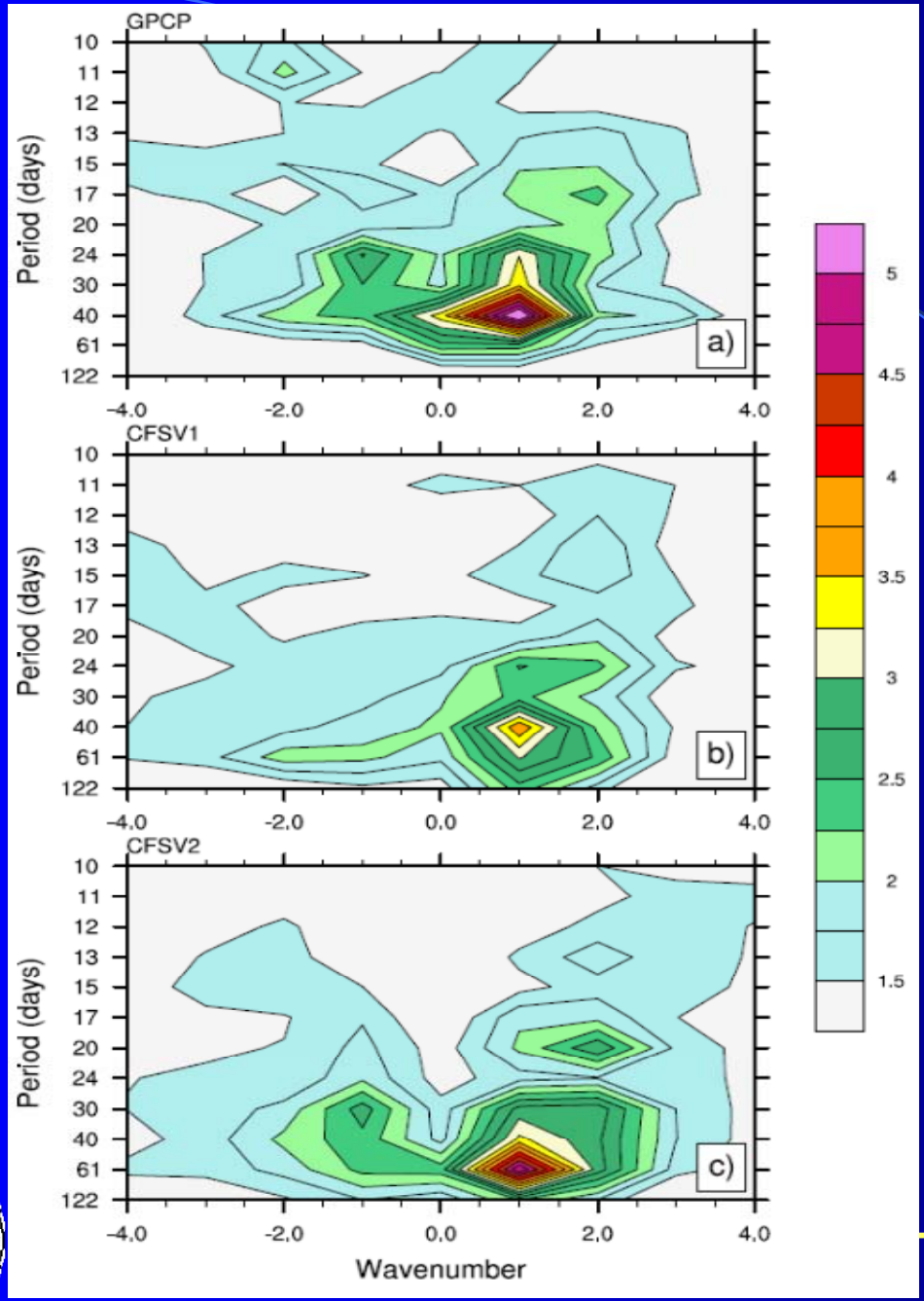

Figure 3: North-south space-time spectra of rainfall anomalies during June-September for (a) observations (GPCP) , (b) CFSv.1 and (c) CFSv.2. In each case, the spectrum is normalized by the corresponding red noise background estimated by an objective method. The north-south spectra have been calculated between 20S and 35N at each longitude between 70E and 90E and spectra are averaged over the longitudes.

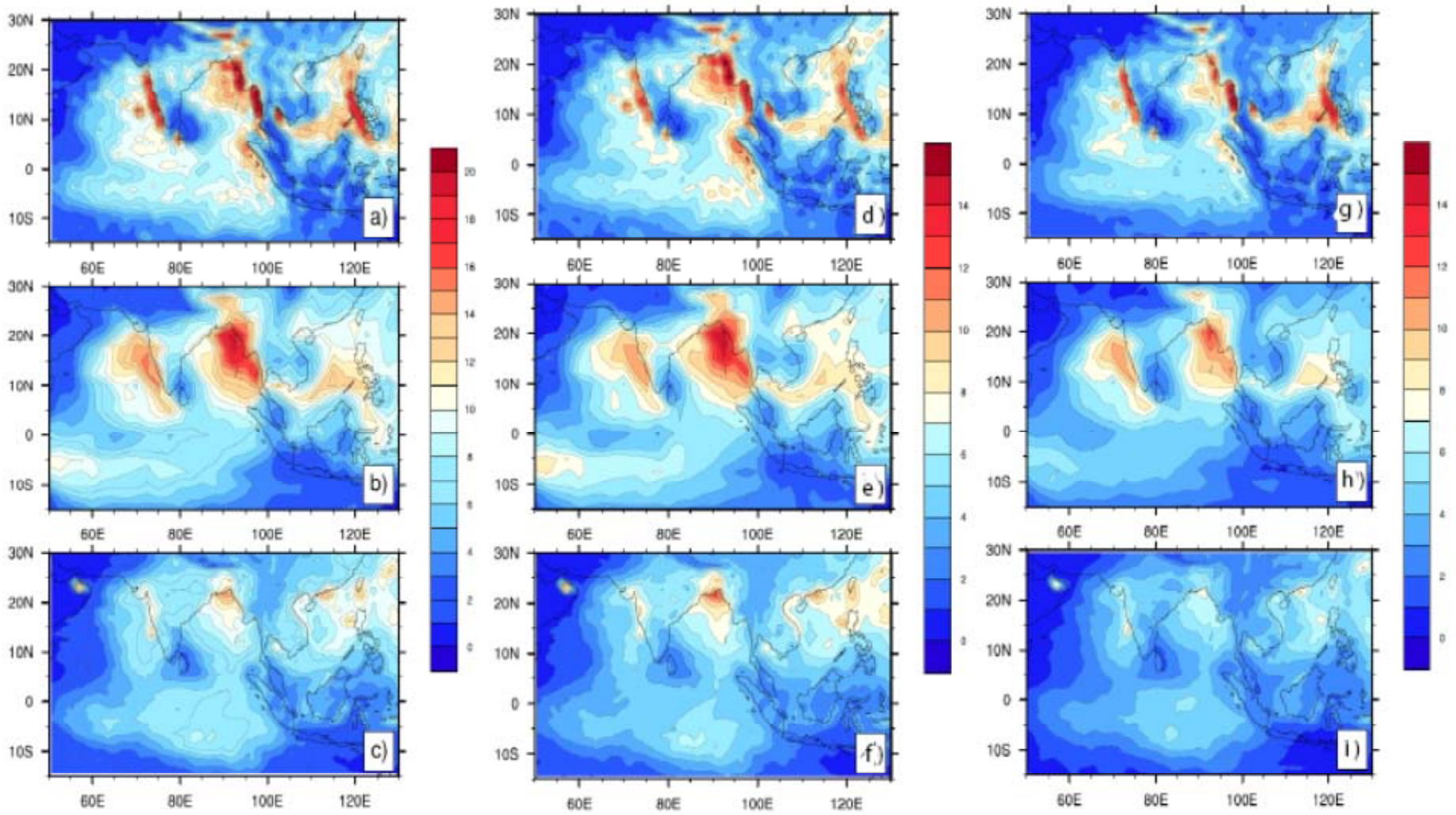

Figure S3: Variance of rainfall during June-September in the intraseasonal time scale in observation compared with simulated variance in the same time scales by the two versions of the model. Variance from observation, of 10-90 filtered anomalies from (a) CFSv.2 , (b) CFSv.1 and (c) GPCP. (d)-(f) are same as (a)-(c) but for 10-25 day filtered anomalies and (g)-(i) are same as (a)-c) but for 25-90 day filtered anomalies.

CONCLUSION (MISO)

- Summer monsoon ISOs have large amplitude, as large as the annual cycle and much larger than IAV of seasonal mean. Has predictability far beyond the weather predictability limit.
- Observed MISOs are associated with strong air-sea interactions. Simulation of correct SST by coupled models crucial for improved simulation and prediction of MISOs by coupled models.
- We introduce a new metric (MISO1 and MISO2) for real time monitoring and forecast verification of MISOs.
- Coupled Forecast System like the CFSv.2 is beginning to make useful forecast of MISO more than 20 days is advance, considered a major advance.

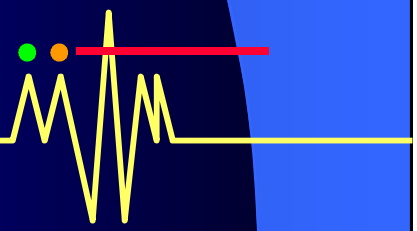

Thank you

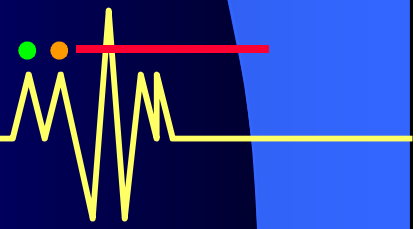

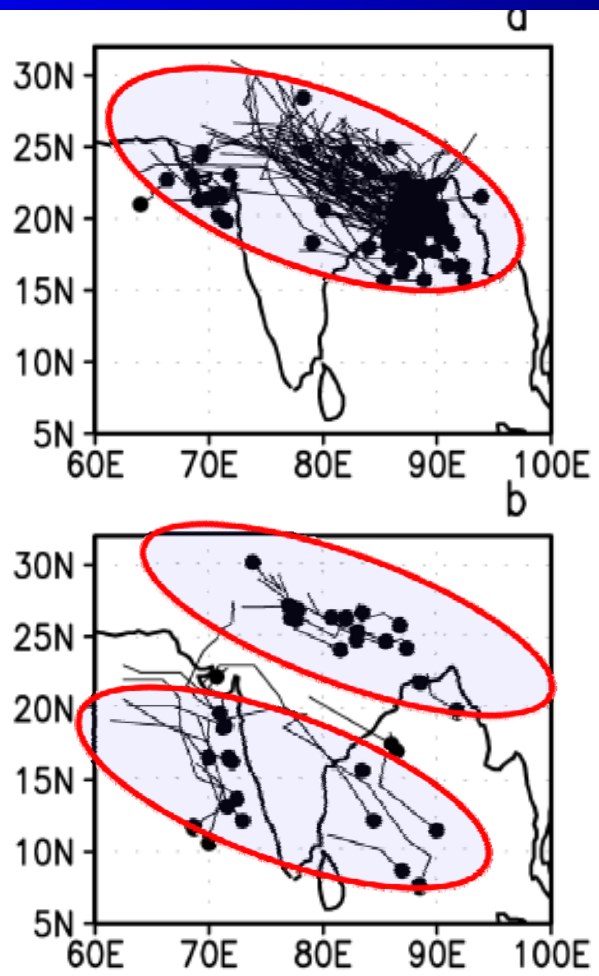

Figure 2.19. Tracks of LPSs for the period 1954–1983 during extreme phases of monsoon ISOs. (a) Active ISO phase (MISI $> +1$) and (b) break ISO phase (MISI > -1). The MISI (monsoon ISO index) used here is the 10 to 90-day filtered relative vorticity during the summer monsoon season (June 1–September 30) averaged over 80°E–95°E and 12°N–22°N. Dark dots represent the genesis point and the lines show their tracks. Large number of LPSs during the active phase are strongly clustered along the MT. The few LPSs that form during breaks clearly avoid the MT region and form either near the foothills of the Himalayas or off the western coast and move westward (after Goswami *et al.*, 2003; © American Geophysical Union).